Title

First-principles exploration of Si alloy electrodes

Author

Sivonxay, Eric

Publication Date

2022

Peer reviewed|Thesis/dissertation

First-principles exploration of Si alloy electrodes

by

Eric Sivonxay

A dissertation submitted in partial satisfaction of the

requirements for the degree of

Doctor of Philosophy

in

Materials Science and Engineering

in the

Graduate Division

of the

University of California, Berkeley

Committee in charge:

Professor Kristin A. Persson, Chair
Professor Gerbrand Ceder
Associate Professor Bryan McCloskey

Spring 2022

First-principles exploration of Si alloy electrodes

Abstract

First-principles exploration of Si alloy electrodes

by

Eric Sivonxay

Doctor of Philosophy in Materials Science and Engineering

University of California, Berkeley

Professor Kristin A. Persson, Chair

Li-ion batteries are the most promising secondary battery to meet the demand of electric vehicles and intermittent renewable energy sources. However, improvements to capacity and performance are necessary. As graphite-based negative electrodes are nearing theoretical capacity limits, alternative anode technologies are being explored to increase energy density. Materials that allow for Li alloying are of considerable interest due to the formation of high Li concentration alloys. Furthermore, additives to Si are a powerful tool to tailor the electrochemical performance of Si. This dissertation explores the use of Si, the alloying type electrode with the highest theoretical capacity, and Si-derived alloy materials as high capacity anodes. We probe the Si-alloy systems using computational methods, including i) simulation of short-range order using ab-initio molecular dynamics, ii) evaluating thermodynamics using electronic structure calculations, and iii) assessing diffusion kinetics using AIMD. From phase diagrams, derived from the first-principles calculations, additive elements are classified as inactive and active elements based on the element's reactivity with Li, where active elements form stable binary compounds with Li while inactive elements do not. In general, binary Si-X compounds, formed with the active elements are not thermodynamically stable and will phase separate into distinct Si and X phases. Alloyed components are capable of tuning the equilibrium lithiation potential with a range of 0 V-3.0 V dependent on the alloying element and mole fraction. Phase separation of the inactive Si-X binary compounds is not expected but, the incorporation of inactive elements leads to dramatically lower capacity due to the combined effects of decreased active material and formation of X rich Si-X compounds which are electrochemically inactive. While there is no limit to alloying with active elements, alloys with greater than 33 % inactive element yield extremely low capacity. Alloying of a third element is found to dramatically modulate the Li diffusivity through the modification of melting temperature. In the case of Oxygen, decreased Li-diffusivity is seen, while Sn increases Li self-diffusion rates. The methods and analysis utilized to predict electrochemical characteristics may be generalized for more alloyed components (ternary, quaternary, etc.) to rapidly screen the chemical space for Si-based alloy electrodes.

Contents

Acknowledgments

I extend my deepest gratitude to all of my friends, past and present, who accompanied me in my journey through my PhD program. First and foremost, I'd like to express my appreciation to my advisor, Kristin Persson, for the immense support and guidance she has provided me, although no amount of thanks will truly convey how thankful I am for all of her support. When I first came to grad school and was looking at research groups, I had the misconception that the best advisor would be the most famous or highest cited. After speaking to Kristin and the postdocs in her group, I was drawn in by the group culture and camaraderie. I have since learned that a good advisor is not only defined by their accolades and research, but by their mentoring style. I'm happy to have had a patient advisor who did not micromanage or add to my stress levels. She gave me a long leash to explore and learn, but pulled me back when I dived far too deep down a rabbit hole. I am also thankful for all the opportunities she has given me to work on soft skills such as writing proposals, disseminating research at conferences, managing group resources, and mentoring other students.

I would also like to extend a warm thanks to the past and present members of the Persson group. While the size of the group has grown precipitously and many people, who were present when I joined, have departed, the group culture remains the same. In particular, I would like to thank my office mates, Shyam Dwaraknath, John Dagdelen, and Jianli Cheng for being open to discussing all matters of research and life, as well as putting up with my *very* clickety-clackety keyboard. I also extend additional gratitude to Shyam, who was always there to field my research questions and provide me with additional guidance, even after his tenure with the group had concluded.

I am fortunate to have family, friends, and groups outside of my research to keep me sane. While my parents and sister were not close in proximity, they always felt like they were nearby thanks to all their support and I always looked forward to their visits. I thank James Chavez, Joey DeGrandchamp, and Karen Chiao for being great housemates and friends. Hanging out with Qingsong Tu (Howard) was never boring and I gained a tremendous amount of experience mentoring students and teaching courses with him. I have made many great friends in the student clubs(Cal Archery and UAVs@Berkeley) I was a part of and had many memorable experiences that I will look back fondly upon.

In addition to those mentioned above, I could not have completed this research without monetary support and access to computational resources. My work was supported in part by the Advanced Battery Materials Research (BMR) program directed by Tien Duong and in part by the U.S. Department of Energy's Vehicle Technologies Office under the Silicon Consortium Project, directed by Brian Cunningham, and managed by Anthony Burrell. This research utilized resources at the National Energy Research Scientific Computing Center (NERSC), a U.S. Department of Energy Office of Science User Facility located at Lawrence Berkeley National Laboratory, and the Lawrencium computational cluster resource provided by the IT Division at the Lawrence Berkeley National Laboratory, operated under Contract No. DE-AC02-05CH11231. Additionally, a portion of this research was performed using

computational resources sponsored by the Department of Energy's Office of Energy Efficiency and Renewable Energy and located at the National Renewable Energy Laboratory (NREL).

Chapter 1

Introduction

Renewable and clean energy sources such as wind and solar power are a key tool in reducing carbon footprint and ultimately in slowing climate change. However, these energy sources are inherently variable with intermittent power delivery, making the challenge of balancing the fluctuations in load and demand more difficult. Many solutions have been proposed, although none individually resolve load imbalance. One of the most promising strategies is energy storage to accumulate energy when power generation is high and demand is low and releasing energy when demand is high. Methods of grid scale energy storage include pumped hydroelectric, flywheels, and batteries. While batteries may not be the most cost effective, depending on the use case, the proliferation of electric vehicles(EVs) and other portable consumer electronic devices has dramatically decreased production costs. Additionally, the widespread adoption of electric vehicles presents an additional avenue to realizing grid scale electric storage, where integrating EVs into vehicle-to-grid infrastructure would allow for distributed load-balancing. While EVs have experienced a boom in popularity, their market share is insufficient to realize vehicle-to-grid storage and significant barriers still hinder its acceptance. While car manufacturers have boosted EV range to be comparable to gasoline powered cars, an outstanding challenge is recharging. Unlike gasoline-powered cars, which can be refueled in minutes, EVs require charging times ranging from 30 minutes to a few hours. Vehicle-to-grid systems further stress battery packs and threaten battery lifespan and longgevity. Therefore, to accelerate the deployment of EVs and use of batteries in grid scale storage, the energy density and rate capability must be significantly improved. To this end, tremendous effort has been placed into the research of high-capacity, high-rate secondary batteries.

In recent years, there has been a surge of investments into these secondary battery research from private investors and government organizations, such as the Vehicles Technology Office (VTO) within the DOE Office of Energy Efficiency & Renewable Energy. The VTO has set a goal to reduce the cost of vehicle batteries to less than \$100/kWh—ultimately \$80/kWh, increase the range of electric vehicles to 300 miles, and decrease charge time to 15 minutes or less. While many secondary battery technologies exist, a solution that leverages the existing global infrastructure and supply chain is ideal, as new battery chemistries would

face significant hurdles to implementation and scale-up. Highly commoditized, and possessing high energy density, Li-ion batteries are the primary choice for use in electric vehicles. Research to develop drop-in solutions to improve the performance of the individual Li-ion battery components is, therefore, a focus of many researchers. Such novel approaches include using high voltage cathode materials, solid-state electrolytes, or alternative anode materials - this dissertation focuses on the latter, particularly on alloying-type electrodes. While alloying anodes promise a significant increase in capacity, they face many challenges associated with a rapid capacity fade that prevent commercialization. Research into the stabilization of these batteries has yielded moderate success; however, progress has been limited due to the trial and error approach used. In this dissertation, high-throughput first-principles calculations are used to investigate a vast chemical space of alloy electrodes, thereby guiding experimental efforts by identifying design criteria and heuristics of alloy electrodes.

In Chapter 1, an introduction to Alloy-based negative electrodes for Li-ion batteries is provided. Chapter 2 discusses the computational methods for evaluating the thermodynamics and kinetics of these alloy electrodes. In Chapter 3, a computational benchmark of the Si and SiO_2 system is presented. Chapter 4 focuses on the impacts of alloying Sn with Si on Li diffusion and structural evolution. Chapter 5 details the high-throughput screening of lithiation thermodynamics in binary Si alloy systems. Finally, in Chapter 6, conclusions and possible future work are discussed.

1.1 Lithium-Ion Batteries

Rechargable Li-ion battery cells are composed 6 main components - a cathode, an anode, two current collectors, electrolyte and a separator. Typical Li-ion batteries utilize graphite anodes and lithium cobalt oxide ($Li_{(1-x)}CoO_2$) cathodes with Cu and Al as the anode and cathode current collectors, respectively. The separator provides mechanical stability and short-circuit protection between the cathode and anode if dendrites from. The electrolyte is an electronically insulating and Li-ion conductive medium that prevents charge transfer and facilitates diffusion of ions between the two electrodes. On the other hand, the current collectors must be electronically conductive while impermeable to the flow of Li-ions. The coupled redox reactions at both electrodes provide a chemical potential difference between the two electrodes and when electrons are allowed to flow between the two current collectors, electrical energy is delivered by the system. This process is known as discharge, corresponding to Li oxidation at the anode and Li reduction at the cathode, with Li diffusing through the electrolyte from the anode to cathode. In charging, a potential is applied across the two current collectors, and the flow of electrons and Li-ions is reversed, replenishing the Li supply in the anode.

1.2 Electrode Materials

Graphite Intercalation Electrodes

Traditional high-capacity Li-ion batteries utilize intercalation-type electrodes for Li storage in both the anode and cathode. The intercalation process reversibly stores Li ions in the lattice of layered materials. The host material in these electrodes does not experience significant structural changes upon Li insertion or removal. Without changes to the host structure, Li storage in these materials is generally limited to a few Li per formula unit. Consequently, these electrodes present low volumetric expansion when cycling, leading to good mechanical stability. Additionally, intercalation electrodes typically have relatively high Li diffusion rates, thanks to low barrier diffusion pathways from site to site.

The current state-of-the-art anode is graphite, composed of graphene sheets bonded by weak Van der Waals bonds. Full Li intercalation into graphite results corresponds with 1 Li atom per 6 carbon atoms, with a specific capacity of $372\,\mathrm{mAhg^{-1}}$ and volumetric capacity of $850\,\mathrm{AhL^{-1}}$.[1, 2, 3] At this stage, the interlayer spacing is increased by $\sim 10.4\,\%$ to accommodate Li insertion. Additionally, the formation of weak Li-C bonds screens C-C vdW interactions resulting in a shift from AB hexagonal stacking to AA stacking. Li is extracted from the lattice during battery discharge, returning the host structure to its initial configuration. The redox reaction describing the Li storage in graphite is as follows:

$$C_6 + xLi^+ + xe^- \longleftrightarrow Li_xC_6 \tag{1.1}$$

Owing to the weak bonds formed, high Li-diffusivities are found, with chemical diffusivities on the order of $\sim 1 \times 10^{-7}\,\mathrm{cm^2\,s^{-1}}$ - $1 \times 10^{-8}\,\mathrm{cm^2\,s^{-1}}$.[1, 4] Another advantage of graphite electrodes is a low operational potential range, of 0.25 - 0.01 V vs. Li/Li+, compared to alternative anode materials. However, this potential is lower than the reduction potentials (0.8 V vs. Li/Li+) of the carbonate electrolytes used, resulting in the decomposition of electrolyte at the graphite interface. Early electrolytes used did not passivate the surface, resulting in continuous electrolyte decomposition. In the case of propylene carbonate, co-intercalation of the solvation shell was found, exfoliating the graphite layers. However, the decomposition products of ethylene carbonate (EC) form a solid layer, composed of both organic and inorganic components, which is electronically insulating to prevent further electrolyte decomposition and Li-ion conductive while inhibiting solvent co-intercalation. The stabilization of the solid electrolyte interface was a key discovery leading to the successful commercialization of graphite anodes in Li-ion batteries is the successful discovery of an electrolyte formulation that forms a suitable solid electrolyte interphase (SEI). While graphite anodes currently power most consumer secondary Li-ion batteries, the room for improvement is capped.[5] Alternative Li storage mechanisms must be leveraged to realize a substantial improvement in capacity.

Alloying Electrodes

One route to improve anode capacity is using alloying-type electrode, such as Si, or a graphite/alloy composite electrode. Li storage in these materials occurs through an alloying mechanism, wherein lithiation occurs through the electrochemical formation of lithium alloys. These Li-active materials are capable of high capacities due to the formation of compounds with greater stoichiometric ratios of Li atoms to host atoms than intercalation electrodes. Integration of Li atoms into the host material is coupled to volumetric expansion proportional to the quantity of Li alloyed. With their high Li-storage capacity, alloy electrodes exhibit colossal expansion, leading to electrode instability due to high internal stresses and mechanical pulverization. Additionally, these materials possess much lower Li diffusivities than intercalation-type materials, leading to low rate capability and large overpotentials. Most elements in the periodic table have been explored as alloy anode materials for Li-ion batteries, although Si is the alloying element with the highest specific and volumetric capacity. The high abundance and high annual global production of Si also lend to its suitability.[6]

Theoretically, Si can alloy with up to 4.2 Li to form $Li_{21}Si_5$, although this phase is only found when cycling at elevated temperatures. At room temperature $Li_{15}Si_4$ is the highest lithiation stage seen. Si presents nearly a ten-fold increase in specific energy capacity ($3579\,mAhg^{-1}$) and about three times increase in volumetric capacity ($2194\,AhL^{-1}$) compared to graphite. While the capacity of Si anodes is superior to graphite anodes, the electrode suffers from mechanical and chemical instability stemming from significant volumetric expansion. These challenges include:

- Volume expansion upon lithiation results in particle cracking, exposure of fresh Si surfaces to the electrolyte, and further electrolyte decomposition. In alloy electrodes, each Li alloyed contributes $14.8\,Å^3\,Li^{-1}$ per formula unit; thus, volumetric expansion in alloying electrodes is unavoidable, but engineered solutions have successfully mitigated volume-related losses.[7] The most common strategy employed to reduce the effects of volume expansion is including void space to allow for growth. Such methods include using Si nanoparticles, Si nanowires, introducing porosity, or hierarchical nanostructures.[8, 9, 10, 11, 12]

- A large first cycle irreversible capacity is found when lithiating crystalline Si, corresponding to the conversion of c-Si to a-Li_xSi. This two-phase reaction front generates inhomogeneous internal stress resulting in further particle cracking and a low initial coulombic efficiency. Starting with amorphous Si is found to decrease particle cracking and increase the initial coulombic efficiency. No discernable difference is found in the Si electrode following the first cycle.

- The SEI formed on Si is non-passivating and, in some cases is observed to dissolve and reform during each cycle. This poor passivation results in parasitic corrosion currents, consuming Li inventory through continuous electrolyte reduction. The most common

approaches to stabilizing the SEI have revolved around electrolyte additives such as FEC or $Mg(TFSI)_2$ to promote the formation of a more robust SEI.[13, 14, 15, 16, 17, 18, 19] These approaches have shown moderate success, capable of improving coulombic efficiency (CE), although they remain insufficient to achieve capacity retention over thousands of cycles.

- The formation and subsequent delithiation of c-$Li_{15}Si_4$ is associated with a large voltage hysteresis and further electrode pulverization. While this issue has not been tackled directly, the crystallization of c-$Li_{15}Si_4$ can be suppressed by nanostructuring, under high pressure, and in metal silicides.[20]

A growing area of study is the use of additional alloy components to stabilize the electrode.[21, 22, 23, 24] Additive components improve mechanical stability and decrease volumetric expansion.[25, 24] These ternary Li-Si-X (or quaternary Li-Si-X-Y) are not high entropy alloys, although these glasses may exhibit exceptional fracture strength as compared to Li-Si, decreasing capacity loss through mechanical fracture. In some cases, alloys exhibit modified electrochemical characteristics with tailored surface reactivity and superior SEI stability.[20, 26] These alloyed elements fall into two groups, active and inactive components. Elements that form stable binary compounds with Li are Li-active and are dubbed the active alloys, while those that do not form stable binaries with Li are inactive alloys. The active and inactive elements are denoted by Ma and Mi, respectively.

Active alloys

The Li-active elements are primarily comprised of p-block elements and late transition metals, although the activity of some elements is contentious.[20, 21, 27] Active elements are also inherently alloy electrodes themselves, forming thermodynamically favorable binary compounds with Li. While many of these elements exhibit Li alloying capability, all of these elements possess a lower specific and volumetric capacity than Si. Thus, when alloyed with Si, a decrease in specific and volumetric capacity is seen. When alloyed with an active element, the Si alloy will typically lithiate through a conversion process. In the conversion reaction, the alloying of Li forms two distinct phases at terminal stages of lithiation, typically Li binaries with the two elements. As Li penetrates these host alloys, Li preferentially bonds with the element with higher lithiation potential, displacing a phase comprised of the second element. As the potential decreases, Li will begin to alloy with the second element. In this process, a nanostructured material will be formed with segregated phase regions composed of the individual elements. In this mechanism, lithiation potentials are expected to be a composite of the individual alloying elements. A representative chemical reaction is as follows:

$$\mathrm{Si_{1-z}Ma_z} \xrightarrow[e^-]{Li^+} \mathrm{zLi_xMa} + (1-\mathrm{z})\mathrm{Li_ySi} \xleftarrow[e^-]{Li^+} \mathrm{zMa} + (1-\mathrm{z})\mathrm{Si} \tag{1.2}$$

In some cases, stable ternary phases may form, resulting in lithiation potentials which differ from the alloy components. An example is the lithiation of SiO_2 where Li_4SiO_4 intermediates are observed, although Li_2O and $Li_{15}Si_4$, are expected to be in thermodynamic equilibrium at maximum lithiation.

Inactive alloys

The Li-inactive elements are mostly early transition metals or alkali metals. Inactive elements do not participate in alloying reactions with Li at anodic potentials and thus do not exhibit Li-storage capability. When alloyed with Si, the role of these components is contentious, with some believing that they are bystanders and follow the reaction:

$$\mathrm{Si_{1-z}Mi_z} \xrightarrow[e^-]{Li^+} \mathrm{zMi} + (1-\mathrm{z})\mathrm{Li_ySi} \xleftarrow[e^-]{Li^+} \mathrm{zMi} + (1-\mathrm{z})\mathrm{Si} \tag{1.3}$$

Others believe that stable binaries formed when alloying Si with inactive metals will result in the deactivation of more Si and further decrease capacity. An example is in the alloying of Si with inactive Ni metal to form $NiSi_2$. Because $NiSi_2$ does not melt congruently, the material is not phase pure, with the presence of Si impurity regions embedded within a $NiSi_2$ matrix.[28, 29, 20] Therefore, all observed capacity is attributed to the lithiation of Si impurities. Contrary to this, nanocrystalline NiSi is reported to cycle with a reversible capacity of $1180 - 1220\,\mathrm{mAhg^{-1}}$ according to the reversible reaction described in eqn. 1.3.[30, 31]

Nevertheless, inactive metals serve as a buffering matrix to reduce lithiation stress and volumetric expansion in both cases.[20] A lower average lithiation potential is observed compared to the strategy of mitigating volume expansion by limiting capacity.[25] In limiting the depth of Si cycling, Si's low voltage regimes are not utilized, leading to higher average voltages as illustrated in fig. 1.1. This voltage depression by inactive metals leads to higher energy densities in a full stack for a-Si/inactive alloys.

Due to the wide compositional space available for alloying electrodes, an Edisonian approach to evaluating the electrochemical properties and thermodynamics of alloys is unsuitable. And while battery cycling experiments are capable of capturing all the physical effects during cycling, it can be challenging to isolate the impacts from alloyed components. Changes in multiple factors such as synthesis environment, crystallite sizes, nanoparticle morphology may have tremendous effects on the measured electrochemical data and the incomplete reporting of experimental conditions obfuscates chemical insight, as described above for the Si-Ni system. In this regard, a computational simulation can more effectively interrogate the equilibrium thermodynamics and structural evolution during lithiation. A first-principles investigation will be capable of rapid, parallel screening of alloy-type anodes. In this work, we demonstrate a high-throughput Density Functional Theory (DFT) workflow for evaluating electrochemical characteristics of alloy anodes in Li-ion batteries.

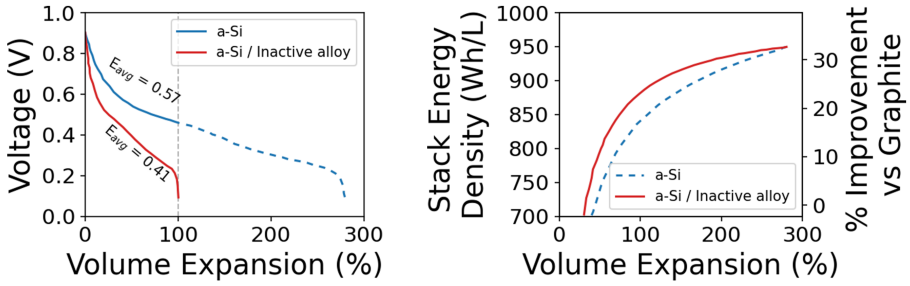

Figure 1.1: Voltage curve (left) of a-Si cycled with limited (to 100%) volume expansion compared to 36/64 v/v a-Si/inactive alloy. Predicted energy densities (right) for a-Si/inactive alloys as compared to a pure a-Si alloy as a function of volumetric expansion. Reproduced from [20]

Chapter 2

Methodology - Modeling Alloy electrodes

2.1 Sampling Amorphous Configurations

Since it is observed that amorphous Si alloys exhibit higher initial coulombic efficiencies and c-Si undergoes amorphization in the first cycle, amorphous electrodes are studied. Simulation of amorphous Si-based alloys and compounds occurs via a melt-quench approach, wherein liquid melts are generated at each composition before using rapid quenching to lock in glassy, amorphous-like local environments. This approach allows the interrogation of alloys of arbitrary compositions, not limited to the compositions for which known alloys or crystal structures exist. We leverage this to study the alloys formed between Si and all the elements on the periodic table - Formulaicly, $Si_{1-y}X_y$, where X encompasses elements from periodic table group 1-17. For each alloy system, we sample 9 compositions $y = \{0.1, 0.2, 0.3, 0.4, 0.5, 0.6, 0.7, 0.8, 0.9\}$. In addition to the binary alloys, we interrogate the amorphous structures for the lithiated forms of these alloys. Amorphous structures were be generated for the products reaction 2.1 with $x = \{0.5, 1, 2, 3, 4\}$.

$$xLi + Si_{1-y}X_y \longrightarrow Li_xSi_{1-y}X_y \tag{2.1}$$

Generating and Equilibrating Liquid Melt

Packmol was used to generate a random arrangement of $\geq$ 100 atoms according to the desired composition[32]. Beginning with a randomized cell configuration instead of melting a crystalline unit cell ensures no hysteresis or bias towards a crystalline system. Initial unit cell volumes were determined from a linear combination of the elemental molar volumes. Molar volumes of the most stable elemental phases found on the Materials Project are used. All AIMD simulations used input parameters as found in the MPMDSet in the pymatgen software package.[33] As a brief summary, one gamma-centered k-point was utilized with a

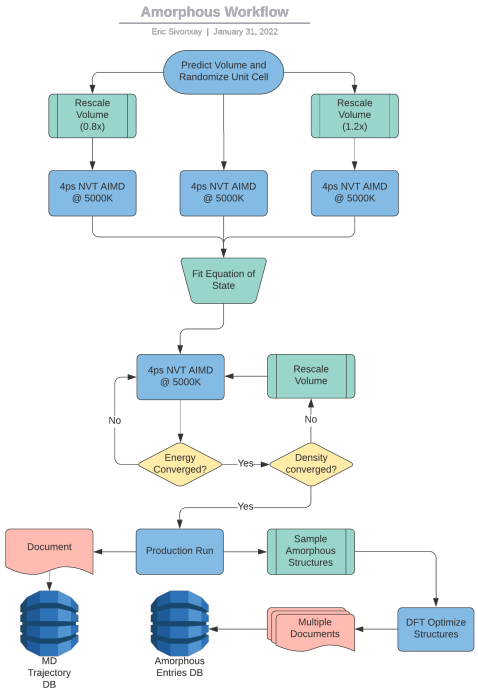

Figure 2.1: Flow chart depicting the workflow for sampling quasi-amorphous configurations

plane-wave cutoff of 400eV, a reciprocal lattice density of 64 per Å^{-3}, and a timestep of 2 fs. The cell stress tensor was output during equilibration runs, using the ISIF=2 input parameter to evaluate the external pressure, but ISIF=0 was used in production runs to decrease computational cost.

Pressure and energy of simulation cells were equilibrated, as described in fig2.1. First, 2ps NVT AIMD simulations are run for simulation cells with 0.8x, 1x, and 1.2x the predicted volume. Pressures and volumes in the initial three simulations are used to fit the Birch Murnaghan Equation of State and interpolate (or extrapolate) volume for $P = 1\,\text{bar}$.[34] Iterative rescaling was then used to ensure the pressure and energy were equilibrated. The rescaling process requires running AIMD simulations using an NVT thermostat until the total energy is stable. After energy convergence, the cell stress is evaluated, and if the average pressure deviates from a $\pm$ 5 kbar tolerance window, the volume is rescaled proportionally to the pressure observed.

The process of energy convergence and scaling the unit cell is repeated until both the energy and pressure meet the convergence criteria. Final 20 ps production run is performed at 5000 K, from which structures are sampled. For some systems, gaseous regions were formed when equilibrating the simulation cells at high temperatures. This was primarily observed in chemical systems containing the elements N and F, which form stable diatomic

molecules. In these cases, the volume was not rescaled before the production run, and energy was the primary convergence criteria. Due to the lower system volume, higher pressure is maintained throughout the AIMD simulation, preventing the formation/sublimation of N_2 and F_2 regions. The pressure is relieved during the quenching process, specifically during the DFT optimization.

Quenching Structures

Following the completion of production AIMD runs, ten structures were sampled at 2 ps intervals and quenched. Two quenching approaches were used in the research to be presented. The first and most frequent method was an "instantaneous" quenching through direct DFT optimization of the structure, allowing for relaxation of both atomic positions and lattice. The second method used was a stepped cooling with AIMD followed by DFT optimization, allowing for atomic and lattice relaxation. Stepped quenching started at 5000K, decreasing temperature by 500K over 400 fs utilizing an NVT simulation, followed by an isothermal hold at the new temperature. The cool and hold process was repeated until a temperature of 0K was achieved. Energies resulting from the direct DFT relaxation were generally greater than those found in stepped quenching due to limited structural reorganization. As discussed in the Chapter 4, a difference in local structures was found in some cases, especially in the alloys of incompatible elements. Generally, quenching through AIMD allows the system to explore the energy landscape and yields more stable local environments due to a slower cooling rate than direct DFT optimization, which is more analogous to a near-instantaneous quench. While structures quenched through both these methods did not typically exhibit any medium or long-range order, some snapshots showed a degree of crystallinity and were discarded. Crystallinity was observed in both visual inspection and the bond orientational order parameter, which was calculated as implemented in pyboo.[35]

Local Structure and Si-Si bonding

Bonding graphs were used to investigate Si connectivity and the local environment changes. A graph is used to represent the bonding in an amorphous structure, where the nodes represent atoms and the edges represent bonds. Connectivity of the graph is determined using pairwise cutoffs, determined by the radius corresponding to the minimum following the first peak in the Radial Distribution Function (RDF). The first peak in the RDF corresponds to the nearest-neighbor interactions between a given pair of elements and roughly follows a Gaussian distribution. The apex of the first peak corresponds to the average bond length between the pair. While the first minimum captures nearest-neighbor interactions, it may also capture some second nearest-neighbor interactions due to an overlap in the distributions for the first and second nearest-neighbor interactions. Conversely, some bonding interactions may be excluded within the tail of the distribution. The RDF, $g_{ab}(r)$, is defined by the eqn.2.2

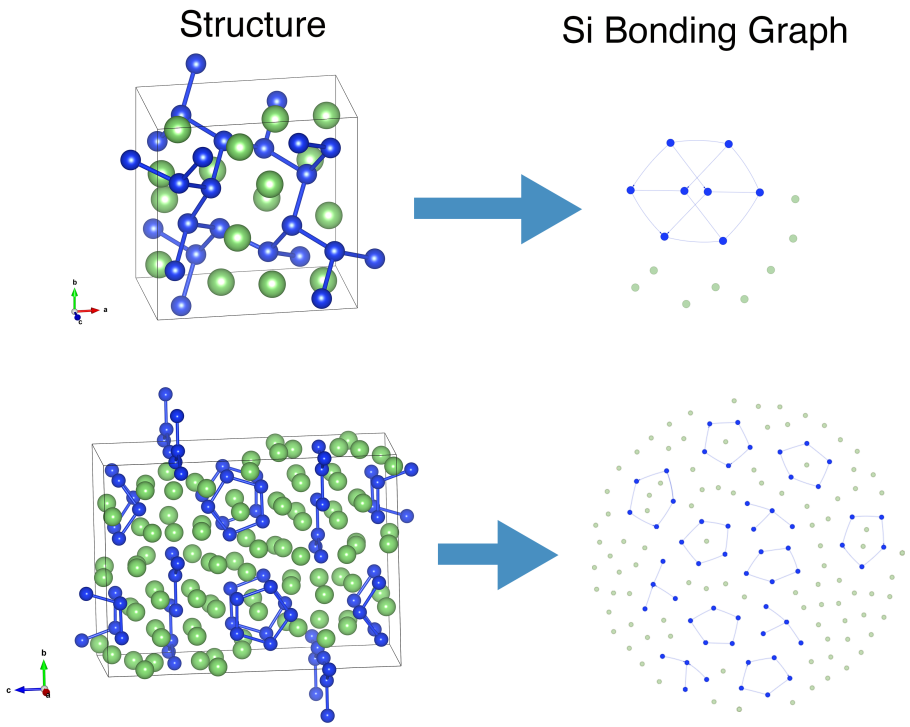

Figure 2.2: Example Si-Si bonding graphs for crystalline LiSi (top) and $Li_{12}Si_7$ (bottom). In both the structure and graphs, Li atoms are depicted in green and Si atoms in blue

.

as follows. [36]

$$g_{ab}(r) = (N_a N_b)^{-1} \sum_{i=1}^{N_a} \sum_{j=1}^{N_b} \langle \delta(|\mathbf{r}_i - \mathbf{r}_j| - r) \rangle \tag{2.2}$$

Implementation of radial distribution function can be found in mpmorph.[37, 38] The distance matrix for the DFT relaxed structure is binned into a histogram, effectively counting the average number of b neighbors at a distance r from atoms of type a. Due to the relatively (compared to classical MD) small simulation cells, RDFs may contain large fluctuations, however, when averaged across all sampled configurations, smoother RDFs are produced. When evaluating Si-Si bonding graphs, isolated sub-graphs represent Si aggregates or clusters. Bonding graphs with no isolated sub-graphs indicate networked Si, where all Si is connected through percolating Si-Si bonds. As is shown in Chapter 3, agglomerates identified through this method agree well with those observed through Nuclear Magnetic Resonance (NMR). Additionally, bonding graphs for each atomic pair are useful in determining the average coordination numbers. Using these approaches, Si's short and medium range order can be quantitatively compared across alloy compositions.

2.2 Thermodynamics

The relative stability of simulated amorphous materials are evaluated from each chemical system's computed phase diagram. It is important to note that these phase diagrams predict phase equilibria at 0K and do not have a temperature axis. Additionally, calculated phase diagrams may deviate from experimental counterparts due to entropic effects or insufficient chemical or configurational space sampling. Much like the crystalline phase diagram formed from an n-dimensional convex hull, we construct the analogous convex hull for the amorphous structures sampled as outlined by Ong et al. [39]. Each simulated structure is represented as a point using its atomic fractions and formation energy, U_F, as defined by eqn. 2.3.

$$U_F(Li_xSi_{1-x-y}X_y) = U(Li_xSi_{1-x-y}X_y) - xU(\text{c-Li}) - (1-x-y)U(\text{c-Si}) - yU(\text{c-X}) \quad (2.3)$$

The phase diagram is given by the minimum convex hull encapsulating all calculated points. In this definition, points coincident with the convex hull, forming vertexes, represent thermodynamically stable equilibrium phases. Edges connecting two stable points indicate a 2-phase equilibrium, while triangles between three hull points represent a 3-phase equilibrium. This can be generalized for an n-component system such that all the simplices $\in \{1, .., n-1\}$ represent phase equilibria between n-1 phases. Compositions which do not intersect the hull are metastable and will decompose to form the nearest adjacent equilibrium phases according to the simplex containing the phase. More detail on the interpretation of the phase diagrams can be found in chap. 5 While the formation energy of all amorphous phases are metastable with respect to the crystalline phases, we posit that crystallization is unlikely to occur for the lithiation of Si-based materials. Lithiation at room temperature does not present sufficient thermal energy to allow long-range structural reorganization, preferring only local rearrangements due to hindered kinetics. With the assumption that long and medium-range order is not observed and lithiation occurs through a series of amorphous phases, the lithiation is represented by the amorphous hull. At end stages of lithiation, plating of Li metal is observed, therefore BCC Li is included in the amorphous phase diagram to enforce proper phase equilibria and lithiation limits. We confirm the phase diagram's ability to predict lithiation in chapter 3 by comparing to experimental lithiation profiles for amorphous Si.

Operating voltage, E, of the full cell is related to the difference in Li chemical potential, μ_{Li}, within the cathode and anode Li potentials.

$$E = \frac{\mu_{Li}^{Cathode} - \mu_{Li}^{Anode}}{e} \quad (2.4)$$

A common and convenient method to probe the performance of electrode materials is to consider its electrochemical behavior in a half-cell, utilizing the material of interest as the cathode and Li metal as the anode. Within the half-cell, eqn. 2.4 is simplified and Li effectively becomes a reference state with a chemical potential of μ_{Li}^0.

$$E = \frac{\mu_{Li} - \mu_{Li}^0}{e} \quad (2.5)$$

The potential of a full cell, $E^{Full\ Cell}$ can then be determined from the difference of the half-cell potentials for the cathode and anode, $E^{Cathode}$ and E^{Anode} respectively.

$$E^{Full\ Cell} = E^{Cathode} - E^{Anode} \tag{2.6}$$

The half-cell potential is therefore the most common method for reporting lithiation potentials of Si-based alloy electrodes in the literature. The chemical potential of Li is defined as:

$$\mu_{Li} = \frac{\partial G_{rxn}}{\partial x_{Li}} \tag{2.7}$$

where x is the mole fraction of Li. To utilize the DFT calculations to determine the Li chemical potential, a simplification to the Gibbs free energy (eqn. 2.8) must be made.

$$\Delta G_{rxn} = \Delta U_{rxn} + p\Delta V - T\Delta S \tag{2.8}$$

DFT calculations occur at 0 K and following structure optimization the internal pressure is 0 bar, therefore the change in Gibbs free energy simplifies from eqn.2.8 to:

$$\Delta G \approx \Delta U \tag{2.9}$$

Because the functional form of $G_{rxn}(x_{Li}, x_{Si}, ...)$ is not known, a numerical method is more convenient to determine the Li chemical potential. To this end, the alternate definition of gibbs free energy is useful.

$$G^{\alpha}_{rxn} = \sum_i x^n_i \mu_i \tag{2.10}$$

Essentially, in a binary system, the chemical potential of each element is also given by the intercepts of the tangent line with the $x = 0$ and $x = 1$ axes. For a ternary system, the chemical potentials are defined by the intercept of the tangent planes with the axes corresponding to the pure elements. Within the calculated phase diagrams, each simplex (line, triangle, etc.), represents a chemical equilibria where the chemical potentials of each element are equal in all phases present. For example when considering a chemical system of A-B-C, the 3-phase equilibria between A_2B_3C, ABC, and ABC_2, the following is true:

$$\mu_i^{A_2B_3C} = \mu_i^{ABC} = \mu_i^{ABC_2} \tag{2.11}$$

where μ_i^{α} is the chemical potential of element i ($i \in \{A, B, C\}$) in phase α. Therefore, solving the system of linear equations (eqn 2.12-2.14) yields the chemical potentials for A, B, and C within the phase triangle.

$$G^{A_2B_3C} = \frac{2}{6}\mu_A^{A_2B_3C} + \frac{3}{6}\mu_B^{A_2B_3C} + \frac{1}{6}\mu_C^{A_2B_3C} \tag{2.12}$$

$$G^{ABC} = \frac{1}{3}\mu_A^{ABC} + \frac{1}{3}\mu_B^{ABC} + \frac{1}{3}\mu_C^{ABC} \tag{2.13}$$

$$G^{ABC_2} = \frac{1}{4}\mu_A^{ABC_2} + \frac{1}{4}\mu_B^{ABC_2} + \frac{2}{4}\mu_C^{ABC_2} \tag{2.14}$$

Under this formalism, a material will alloy with Li only if its Gibbs free energy is lowered by the inclusion of Li and the convex hull is concave up. Lithiation will track the convex hull until the simplex representing the n-phase equilibria with Li is reached. Equilibrium with the BCC Li phase predicts that the plating of a separate Li phase is more favorable than further alloying. The capacity of the material is bounded by this final equilibrium and the specific capacity is calculated with respect to this limit.

$$C = \frac{nF}{3.6 * M} \tag{2.15}$$

where n is the # of Li atoms alloyed, F is the Faraday constant, and M is the molecular weight of the final lithiated phase. Alternate definitions of the specific capacity utilize the molecular weight of the starting material, however, this metric may be misleading and inflates the capacity.

2.3 Kinetics

The rate performance of alloy electrodes during cycling is related to many factors including but not limited to grain boundary diffusion, electronic conductivity, and Li-diffusivity. In an amorphous alloy, the limiting factor is the diffusion kinetics for Li. We probe the intrinsic self-diffusivity of elements in Si alloys using equilibrium AIMD simulations. The motion of each particle within the simulation cell is reflective of chemical bonding, temperature, and other characteristics. By tracking the trajectory of each particle as the simulation progresses, the kinetics are realized. Transport coefficients in MD simulations are typically computed from the Mean Squared Displacement (MSD) from the Einstein relationship or the Velocity autocorrelation function (VACF) according to Green-Kubo relations. Both these methods yield the same diffusivity values[40], however we opt to use MSD. as defined by equation 2.16 and 2.17. AIMD is computationally expensive, requiring a DFT calculation at each time step to determine the forces.

$$\hat{b}(t) = \frac{1}{\tau}\int_0^{\tau} [x(t'+t) - x(t')]^2 dt' \tag{2.16}$$

$$\hat{D}(t) = \frac{1}{2} * \frac{\hat{b}(t_2) - \hat{b}(t_1)}{t_2 - t_1} \tag{2.17}$$

This drastically limits simulation time often leading to poor sampling of diffusion events. This necessitates the use of averaging methods to reduce statistical error and to fully leverage the simulations. Such averaging methods include time-averaging and ensemble-averaging. In time-averaging, the MSD is computed for all time-lags (t') and averaged over all possible time origins (t), as illustrated in fig 2.3, maximizing the sampling within each trajectory.

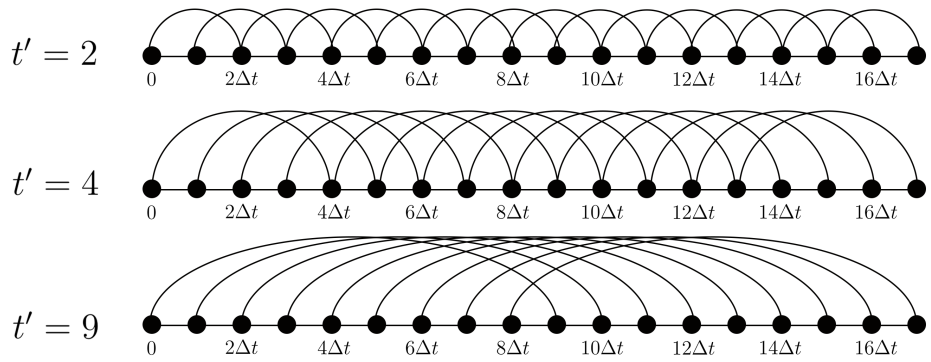

Figure 2.3: Schematic of MSD calculation for time lags of 2 (top), 4 (middle), and 9(bottom) timesteps. Δt is the simulation timestep of 2ps. Figure adapted from [40]

Ensemble averaging allows for the simulation of multiple trajectories in parallel to improve the sampling statistics and improve uncertainty in extrapolated values.

To ensure proper sampling of diffusive events, a minimum MSD was enforced, corresponding to the average Li cage size observed. Hybrid ensemble/time averaged trajectories not satisfying a minimum MSD of $3.0\,\text{Å}^2$ were discarded and not factored into diffusivity calculations. In these cases, the MSD, when viewed in log-log, do not exhibit a linear diffusive regime. Diffusion coefficients were fit from the linear regime of the MSD up to a maximum of 75 % of the simulation time.

Using the average temperature during the NVT AIMD simulation, room temperatures were extrapolated from the Arrhenius relationship (eqn 2.18).

$$D = D_0 * e^{aT}; a = \frac{E_A}{R} \tag{2.18}$$

It is noted that the mechanism governing diffusion may change across the temperature range. However, due to the size and time limitation of AIMD, low temperature points cannot be adequately sampled and an extrapolation must be used. With the data points sampled, it is found that the diffusivities do not follow the Vogel-Fulcher-Tammann (VFT) equation. In fact, regression using the VFT equation fails to converge for all samples.

Rigorous propagation of uncertainties was performed through all averaging, regression, and extrapolation operations performed. Uncertainties in regressed values, σ_{D_0} and σ_a, are obtained from the diagonals of the regression covariance matrix. Reported errors are uncertainties, corresponding to 1 standard deviation, in the calculated diffusion coefficients.

$$\sigma_D = \sqrt{\sigma_{D_0}^2 * (\frac{D_{298.15K}}{D_0})^2 + \sigma_a^2 * (\frac{D_{298.15K}}{289.15K})^2} \tag{2.19}$$

Chapter 3

Benchmarking the Si alloy electrode system

This chapter is reproduced with permission from Electrochimica Acta. 2020, 331.[41]

3.1 Introduction

Due to their high theoretical gravimetric capacity, alloys have garnered much attention as potential high energy density anodes in energy storage applications.[42, 27, 43] Specifically, silicon exhibits a theoretical maximum gravimetric capacity of 3579 mAh/g, an order of magnitude greater than that of the state-of-the-art graphite anode ($\sim$ 372 mAh/g).[7] While several other values for theoretical gravimetric capacity corresponding to formation of Li21Si5[44, 20] (4008mAh/g) and Li22Si5[45, 46, 47, 48] (4199mAh/g), it has been shown that these phases cannot be reversibly formed, even when cycling at elevated temperatures[44, 7]. Silicon also suffers from several performance-inhibiting attributes stemming from its large volumetric expansion under lithiation and its chemical reactivity with the liquid electrolyte. The large volume expansion (up to 300%) of the Si electrode results in mechanical pulverization and loss of electrical contact which reduces the capacity as well as the cycle life of the system. Efforts to reduce the degradation have been creative ranging from i) the use of nano-sized particles/architectures[49, 50, 51, 9, 52], ii) thin films[8, 53, 54], to iii) porous or hollow particle[55, 12, 56], and iv) core-shell particles[57, 10, 58]. Common to all these attempts is the increased Si surface area to volume ratio, which, while alleviating the internal strain under lithiation, also increases the reactivity with the electrolyte, lowers the volumetric energy density of the composite anode and increases the amount of native surface SiO_2. The growth of SiO_2 on Si has been well studied both in the semiconductor and the energy storage field, and is found to be tunable, in composition, thickness, and crystallinity, by varying the concentration of oxygen, water present and temperature during the synthesis process.[59] The native SiO_2 surface layer on bulk Si anode particles is usually found to be amorphous due to its rapid formation under ambient conditions, and

strain with respect to the underlying Si phase[60]. However, despite recent attention, the native oxide layer's impact on the Si anode electrochemical performance remains elusive[61]. On one hand, the presence of SiO_2 has been suggested to promote a first-cycle functional surface electrolyte interface (SEI) formation through the passivation of the anode.[11, 62] Core-shell architectures consisting of a SiO_z layer grown on a Si nanotube were, as a "mechanical clamping layer", found to restrict Si swelling to the interior channel[11]. Additional studies on sub-stoichiometric silicon oxides (SiO_z for $z < 2$) suggest the oxide layer is active during the cycling of the material. Jung et al. [63] used first-principles molecular dynamics to investigate the lithiation behavior of substoichiometric amorphous SiO, finding a theoretical capacity of 3172 mAh/g corresponding to the composition $Li_{5.22}SiO$. Furthermore, they also hypothesized that a SiO anode, thermodynamically evolves towards Li-Si alloys and Li-silicates($Li_2Si_2O_5$, $Li_6Si_2O_7$, Li_4SiO_4)/Li_2O, respectively.[63] In a similar study, Chou et al. [64] used first principles to study the structural evolution of amorphous $SiO_{1/3}$ during lithiation, finding an increase in the Li-Si bonding and the formation of Li_6O complexes.

On the other hand, bulk SiO_2 exhibits a high impedance, caused by its low electrical conductivity and low Li mobility.[65] Hence, some studies suggest that, as opposed to bulk SiO_2[66], a thin SiO_2 surface layer remains inert under lithiation, due to the activation energy and overpotential required to break the strong Si-O bonds. For example, Ariel et al. reported on the use of a 9nm SiO_2 film as a solid electrolyte. By monitoring the voltage of the Li_yCoO_2/SiO_2/Si cells while charging, they suggested that SiO_2 was both electrically insulating and unreactive to Li, allowing for Li transport from the Li_yCoO_2 to the Si to form Li_ySi [66]. In contrast, other reports claim that SiO_2 surface films react with Li to form lithium silicates, Li silicides and even Li_2O upon lithiation.[67, 68, 69, 49] Zhang et al. [67] studied the structural evolution, electronic conductivity, and ionic conductivity of Li in SiO_2 films on SiC nanowires. The lithiation of the SiO_2 thin film was observed by TEM, revealing the presence of Li_2O and Li_4SiO_4 upon lithiation of amorphous SiO_2. Multiple reports show that a thicker SiO_2 surface layer causes increased irreversible capacity loss and low coulombic efficiency, due to Li consumption in the first cycle.[62, 68]

Numerous experimental studies on the diffusivity of Li in c-Si and a-Si report highly disparate values ranging from $10^{-16}\,cm^2\,s^{-1}$ - $10^{-8}\,cm^2\,s^{-1}$ in Li_xSi[70, 71, 72, 73, 74, 75, 76, 77, 78, 54, 79]. Diffusivity of $10^{-9}\,cm^2\,s^{-1}$ to $10^{-7}\,cm^2\,s^{-1}$ is found in amorphous Li_ySi (for $0 < y < 3.75$) and $10^{-10}\,cm^2\,s^{-1}$ to $10^{-9}\,cm^2\,s^{-1}$ in c-Si using ab-initio molecular dynamics (AIMD) [80, 81]. Using nudged-elastic band (NEB) and Kinetic Monte Carlo (KMC), the diffusivity of Li in c-Si is found to be $10^{-13}\,cm^2\,s^{-1}$ to $10^{-12}\,cm^2\,s^{-1}$ [82, 83], even as low as $10^{-16}\,cm^2\,s^{-1}$ to $10^{-8}\,cm^2\,s^{-1}$ in a study by Yan et al.[84] Similar to the range of results and conclusions pertaining to the reactivity of SiO_2, the ionic conductivity and Li kinetics of amorphous SiO_2, as a function of lithium content is contentious. Li diffusion in Li_4SiO_4 was studied using 2-D NMR techniques, which yielded high relaxation times, correlating to high Li activation energies of 756 - 850meV and 530 - 700meV, for the crystalline[85] and polycrystalline[86] Li_4SiO_4 phases, respectively. In the amorphous phases, Gobel et al.[87] found conflicting activation energies within the same sample using NMR and electrical conductivity measurements; 228meV and 673meV. A recent study by

Ostadhossein et al. also found slow Li diffusion using reactive force fields in amorphous Li_ySiO_2 for $0.5 < y < 3.5$ and suggested a concave diffusion behavior with concentration; $10^{-15}\,cm^2\,s^{-1}$ for $y = 0.5$, increasing to $10^{-9}\,cm^2\,s^{-1}$ at $y = 1.5$ and then decreasing again to $10^{-13}\,cm^2\,s^{-1}$ at $y = 2.5$.[88]. The opposite trend is observed by Zhang et al. using AIMD, finding monotonic decreasing diffusivity for $0.1 < y < 1.0$ in amorphous Li_ySiO_2.[67] On the other hand, Du et al.[89] reported consistently high diffusivities of $10^{-4}\,cm^2\,s^{-1}$ - $10^{-5}\,cm^2\,s^{-1}$ in glassy $yLi_2O - (1-y)SiO_2$ at 800K using classical molecular dynamics simulations. Additionally, Jung et al. [63] find a high Li diffusivity of $1.8 \times 10^{-8}\,cm\,s^{-2}$ in crystalline Li_2O using NEB.

The widely varying results for Li diffusion in silicon oxides motivate a revisit, in particular using a consistent methodology, comparing transport in amorphous Si with SiO_2. Previous work has focused on crystalline systems, such as $Li_2Si_2O_5$, $Li_6Si_2O_7$, Li_4SiO_4, and Li_2O[63], and amorphous Si and Li_ySi[82, 83, 80, 81, 84], with only one study of Li_ySiO_2 for $0.1 < y < 1$[67]. In particular, the Li insertion kinetics and structural evolution of Li_ySiO_2 has only been studied, using first principles calculations, within a subset of the lithiation range, $0 < y_{Li} < 1$, despite a maximum theoretical lithiation capacity of $0 < y_{Li} < 8.2$. In this paper we investigate the lithiation thermodynamics and kinetics of amorphous Li_ySiO_2 for the full concentration range $0 < y_{Li} < 8.2$, using Density Functional Theory (DFT) and AIMD and compare its properties - using the same methodology - to the crystalline phases as well as to bulk amorphous and crystalline Si.

3.2 Computational Methods

Density Functional Theory calculations

The Vienna Ab-Initio Simulation Package (VASP)[90, 91] was used for all first-principles calculations presented. We use the projector augmented-wave (PAW) potentials[92] along with the Perdew-Burke-Ernzerhof (PBE) generalized-gradient functional (GGA).[93] In structure optimization calculations, all lattice parameters and atomic positions were fully relaxed using a plane wave cutoff of 520 eV, at a minimum reciprocal lattice k-point density of 64 per $Å^{-3}$. The parameters used for all calculations are extensively benchmarked by the Materials Project and can be found in the Python Materials Genomics (pymatgen) documentation in the MP Relax and MP Relax sets.[33] Structures for the crystalline materials were taken from the Materials Project whereas amorphous structures are created as described in section 3.2. Ab-initio molecular dynamics (AIMD) simulations were performed with the NVT ensemble as implemented in VASP using a time-step of 2 fs, with a plane wave cutoff of 400 eV and one gamma centered k-point to reduce the computational cost.

Generating Amorphous Structures

An AIMD based workflow was used to generate representative amorphous structures for Li_ySi and Li_ySiO_2, for $0 < y < 5$ according to a 'melt-quench' methodology previously demonstrated on several amorphous oxide systems[38, 37]. The workflows for generating amorphous structures are constructed using the pymatgen, Fireworks, and atomate software packages[33, 94, 95], and are available at http://github.com/materialsproject/mpmorph. First, atoms were randomly distributed in a cubic simulation cell following the desired composition using packmol[32], at a density $\sim 20\%$ larger than the crystalline compounds. Unit cell sizes were constrained to ~ 100 atoms to ensure reasonable runtime of AIMD simulations. Thus, we note that for some of the high Li content structures, few Si atoms are present. The pressure was then equilibrated through a series of constant temperature AIMD simulations at 3000 K, rescaling the unit cell between each AIMD simulation until an internal pressure of 0 bar was realized, and a stable melt is obtained. Energy equilibration was achieved in a 10 ps simulation before snapshots of the melt were collected at regular intervals from a final 10 ps production run. The snapshots of the system were quenched following a stepped cooling scheme with 400 fs cooling and 1 ps isothermal steps. Final structures were optimized using VASP with higher precision parameters compatible with the Materials Project calculations, as described above in section 3.2.

Lithiation Thermodynamics

The formation energy (U_F) for the amorphous phases is calculated with respect to crystalline termini (Si, Li, and O_2) as;

$$U_F(\mathrm{Li_ySiO_z}) = U_{\mathrm{Li_ySiO_z}} - yU_{Li} - \frac{z}{2}U_{O_2} - U_{Si} \tag{3.1}$$

where $U_{Li_ySiO_z}$, U_{Li} and U_{Si} represent the DFT-calculated ground state energies of the silicides/silicates, bcc Li and diamond cubic Si, respectively, in units of eV/atom. U_{O_2} is the energy per atom (eV/atom) of O_2 with an applied gas correction.[96] The ground state energies are used to construct the low-temperature phase diagram, and the electrode potential (E) of each phase triangle is obtained as:

$$\mu_{Li} - \mu^0_{Li} = neE \tag{3.2}$$

where μ_{Li} is the chemical potential of Li in a lithiated phase, μ^0_{Li} is the reference chemical potential of bcc Li metal, e is the elementary charge of an electron, and n is the number of Li inserted. Under this framework, the calculated electrode potentials are referenced to the Li/Li^+ reference electrode, and will be provided as such throughout this article. The chemical potentials of μ_{Li}, μ_{Si}, and μ_O in each phase region are calculated by solving a set of linear equations, one per each stable phase, as in eq. 3.3. [97]

$$G^i_{rxn} = \sum_{j=Li,Si,O_2} x^i_j \mu_j \tag{3.3}$$

Here, x represents the mole fraction of element j within phase i. At room temperature, ΔG can be approximated by the change in ground state energy, $\Delta G_{rxn} \approx \Delta U_{rxn}$.[98, 99] For the lithiation of Si, $\Delta U_{rxn} = U_F(\mathrm{Li_ySi})$, while the in the lithiation of SiO_2, $\Delta U_{rxn} = U_F(\mathrm{Li_ySiO_z}) - U_F(\mathrm{SiO_z})$.

The gravimetric capacity, C (mAh/g), of each $\mathrm{Li_ySi}$ or $\mathrm{Li_ySiO_2}$ phase is calculated according to the following equation.

$$C = \frac{yN_Ae}{MW} * 4.45 * 10^{-20} \tag{3.4}$$

Where N_A is Avogadro's number, MW is the molecular weight of the starting electrode, $28.09\,\mathrm{g\,mol^{-1}}$ and $60.08\,\mathrm{g\,mol^{-1}}$ for $\mathrm{Li_ySi}$ and $\mathrm{Li_ySiO_2}$, respectively, and $4.45 * 10^{-20}$ is the conversion factor from the elementary charge, e, to mAh.

Lithium Diffusion

Following the simulation of amorphous structures discussed in section 3.2, the Li diffusivity was calculated from AIMD simulations at 500 K, 1000 K, and 1500 K. Three starting structures, equally spaced, were chosen from the 3000 K AIMD trajectories, the volume of the cell was equilibrated for each temperature (P = 0 kbar) before production runs. From the trajectories, the mean square displacement (MSD) as a function of time t is calculated with time-averaging to improve the collected statistics as:

$$\langle \vec{r}^2(t) \rangle \approx \frac{1}{N(T-t)} \sum_{i=1}^{N} \int_0^{T-t} [\vec{r}_i(t'+t) - \vec{r}_i(t')]^2 dt' \tag{3.5}$$

Here $\vec{r}$ is the vector of unwrapped coordinates of each atom, N is the number of diffusing atoms, T is the total simulation time, t' is the lag time, and i is the Li atom index. The diffusion coefficient, D, is obtained from the slope of the MSD versus time in the linear regime. We used 200 ps AIMD simulations and an upper bound of 70 % of the maximum simulation time in determining D. [100] The diffusion coefficient at room temperature 25 °C is obtained through extrapolation of an Arrhenius model fitted to the average D values calculated for each of the three high-temperature AIMD simulations. Estimated numerical errors of the diffusion coefficient are obtained from the variance-covariance matrix, for the regression to the Arrhenius equation, through the propagation of uncertainty.

3.3 Results and Discussion

In the following sections we present and discuss the resulting Si and SiO_2 amorphous structures and their short-range order motifs and benchmark the structures against previous experimental results, as well as the phase stability, voltage profiles, and Li diffusion as a function of Li content.

Short range order and Si connectivity in amorphous Li_ySi and Li_ySiO_2

First, we establish that the resulting 'melt-quench' Li_ySi amorphous phases are good representatives of the local structures formed during electrochemical Li intercalation, e.g. by comparing them to the short-range order motifs previously established experimentally.[101, 102] To probe the medium-range order of the system, the Si networks were examined over the composition range using a clustering approach that identifies groups of Si atoms based on bonding and connectivity. Two Si are said to belong to the same aggregate if there is a path between them passing through other bonded Si atoms.[103] The clustering summarized in Figure 3.1 qualitatively agrees with previous reports[102] on Li_ySi local motifs. As a function of increasing Li content, we observe that a Si network structure is initially present before y = 0.5 (LiSi), as shown in the inset of Fig. 3.1, rapidly breaking up into smaller clusters by y = 1.7 ($Li_{12}Si_7$). Thereafter, a gradual transition occurs between y = 1.7 and y = 3.25 ($Li_{13}Si_4$) where the Si aggregates no longer percolate through the structure, leading to an increasing amount of Si dumbbells and isolated Si. The formation of small clusters previously described[102, 101, 104] appear at y = 1.7. At compositions y > 3.25, dumbbells dominate although a sizeable fraction of 4-atom clusters exhibiting linear as well 'Y' (see Fig.1) arrangements, similar to those seen in crystalline $Li_{12}Si_7$ [105], are also present. In the highest lithiated state studied, y = 4.2, isolated Si and dumbbells are the most prevalent motifs. While the breakup of the Si network and formation of clusters would be expected for random atomic configurations, with decreasing Si concentration, the formation of these Si aggregates is not commensurate of truly homogeneously distributed atoms, suggesting that the structures formed capture the chemical interactions between the Li and Si atoms. This is supported by charge population studies conducted by Chevrier et al.[106, 107] and Kim et al.[108] of amorphous and crystalline Li_ySi, which show a significant increase in Si charge state and nearly constant charge state for Li with increasing Li content, suggesting Si charge state is dependent, primarily, on its local environment. An equivalence of Si charge state in the amorphous and crystalline phase is also observed, further confirming the similarity of the Si local environment in both the amorphous and crystalline states. Hence, in summary, we believe that an acceptable agreement between the simulated amorphous Li_ySi local motifs and those found by electrochemical lithiation is established.

In order to understand the evolution of local arrangement and ionic coordination in the computationally-derived amorphous SiO_2, as a function of lithiation, we follow a similar procedure. The simulated amorphous SiO_2 structure exhibits sharp peaks corresponding to Si-Si, Si-O, and O-O bonding centered at 0.30 nm , 0.18 nm, and 0.28 nm respectively. As a comparison, the average bond lengths in the amorphous lithium silicides for Si-Si, Si-Li, and Li-Li are found at 0.24 nm, 0.26 nm, and 0.27 nm, respectively. With increased Li content in SiO_2, a new peak appears in the Si-Si bonding at 0.24 nm as seen in Fig. 3.2a, characteristic of the Si-Si bond length in Si and Li_ySi. This peak grows with the addition of Li, indicative of the formation of more Si-Si bonds, until y = 3 where the peak's decline is seen due to the formation of isolated Si atoms, characteristic to $Li_{21}Si_5$. As more Li is added, this

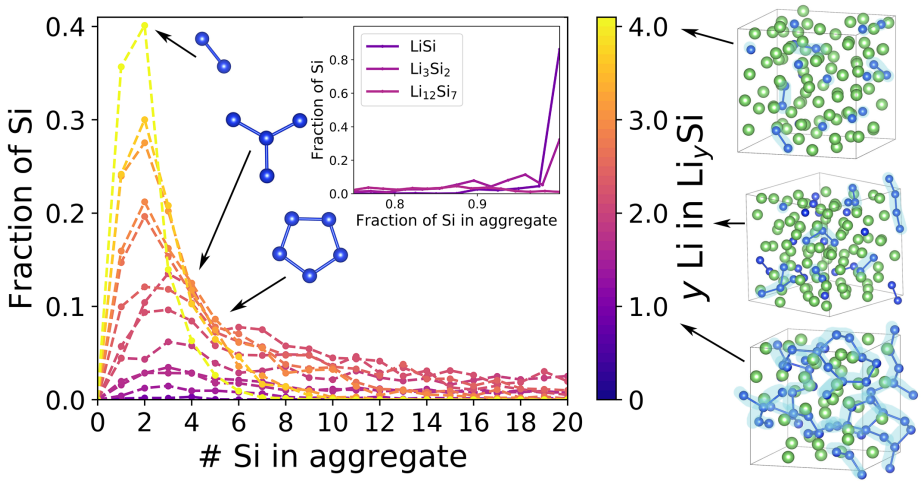

Figure 3.1: Aggregation of Si in Li_ySi for $0 < y < 4.2$, where the x-axis indicates the size of the Si group and y-axis shows the fraction of Si in each group size. Color indicates composition, as seen on the color scale. Inset shows the aggregation of Si in networked regime, with x-axis indicating fraction of Si in the simulation cell that compose the aggregate. Representative structural motifs are highlighted to the right, with Si atoms show in blue and Li atoms in green.

peak grows in magnitude until the initial 0.30 nm bonding disappears by y = 3, indicating a break up of the Si-Si network. In parallel, the O-O peak (see Fig. 3.2b) at 0.31 nm, corresponding to Li_2O bond lengths, increases in height which indicates formation of Li_2O environments. Hence, the overall trend with lithiation of amorphous SiO_2 is increasing Li-O and Li-Si bond formation, at the expense of Si-O bonding, in agreement with previous results on substoichiometric SiO_z. [109, 64]

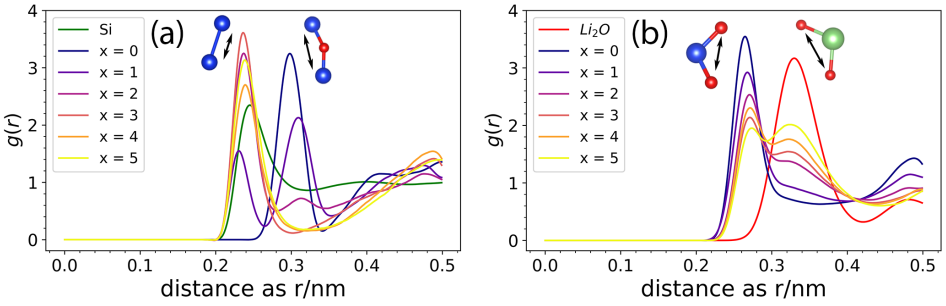

Figure 3.2: Radial distribution functions of a) Si-Si and b) O-O pairs in amorphous Li_ySiO_2

To further examine the short-range order and network formation in the silicates,the analysis applied to the lithium silicides Li_ySi is modified to extract coordination and connectivity information for the multiple species found in the Li-Si-O system. Here, Si and/or O are defined to exist in the same aggregate if a path links the two through bonded Si and/or O atoms. Within this approach, the aggregates belong to one of three groups (indicated in Figure 3.3 by color); i) those containing Si and O, ii) those with only Si, and iii) the O which only binds to Li e.g. Li_2O environments. Similar to the Si-networks in the silicides, the silicates are found to maintain large Si-O networks in amorphous SiO_2 and $LiSiO_2$ as seen in Figure 3.3. Lithiation past $LiSiO_2$ causes network fragmentation and isolation of substoichiometric SiO_z regions. Beyond z = 1, Figures 3.3b-d), the formation of Li_2O environments are also observed. Consequently, a decrease of the O/Si ratio in Li-Si-O clusters, for aggregate sizes < 0.2, between Fig 3.3c and 3.3d is observed, commensurate of the formation of Li_2O-like environments at the expense of Li_ySiO_z. Comparisons between the observed local environments and the prediction of thermodynamically stable phases are elaborated upon in Sec. 3.3.

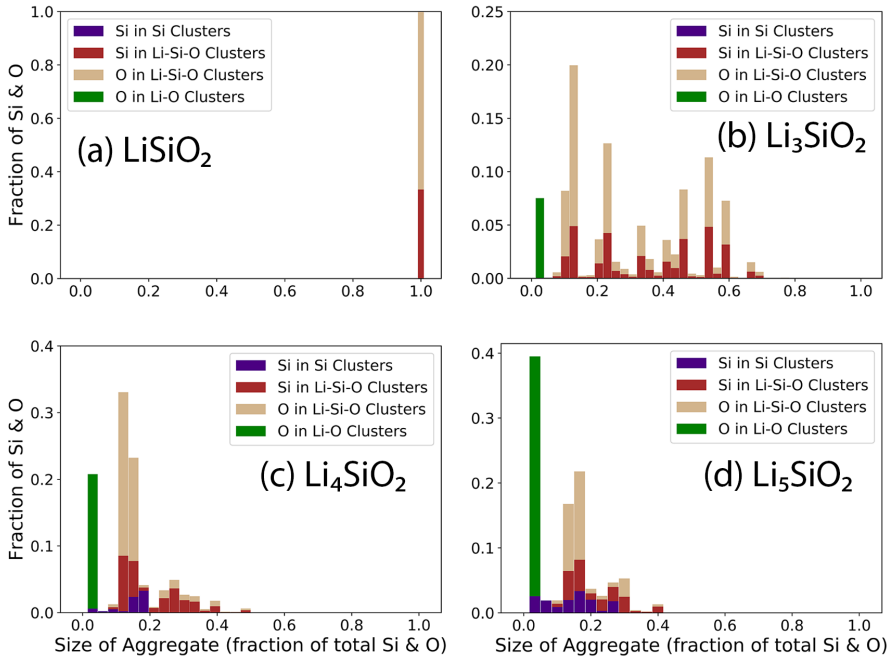

Figure 3.3: a-d) Cluster size distributions in amorphous Li_ySiO_2 for y=1, 3, 4, & 5. Similar to Fig. 3.1, the x-axis indicates the fraction of the Si & O in the structure in each cluster and the y-axis shows the fraction of Si and/or O within that cluster. Colored bars represent the Si or O in the 3 types of aggregates, as specified in the text.

The lithiation process in the Li-Si-O system

Figure 3.4a) shows the calculated Li-Si-O phase diagram at low temperature, which is constructed from the calculated formation energies (for details, see section 3.2), for the crystalline and amorphous phases respectively. The convex hull, which constructs the energy envelope of the thermodynamically stable phases,[39] is depicted with lines and the low-temperature stable phases as nodes along those lines. We emphasize that metastable compounds, e.g. those with energies above the convex hull, may be observed experimentally if the energy difference is small compared to the room temperature driving force for structural reorganization, similar to the case of amorphous Si.

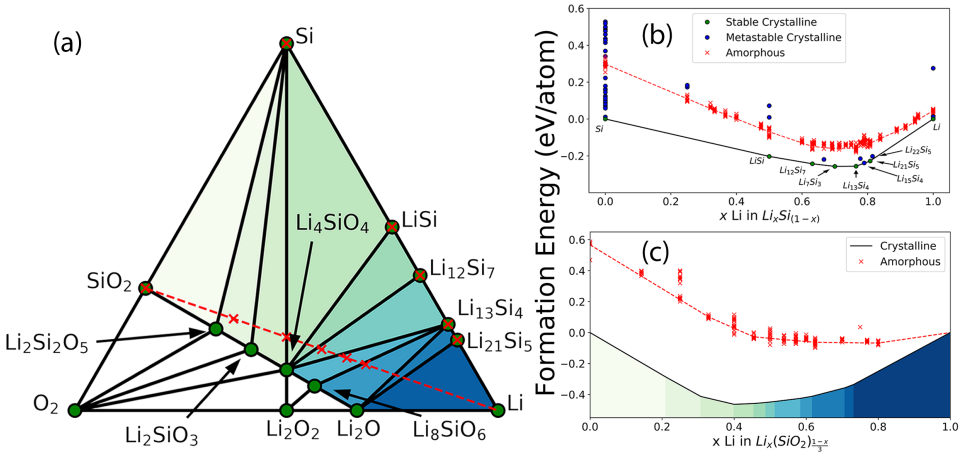

Figure 3.4: a) Si-Li-O phase diagram, including calculated amorphous states and crystalline phases from the Materials Project, shown as red X's and green circles, respectively. Also shown is the formation energies of the crystalline as well as amorphous b) Li silicides with respect to crystalline Si and Li and c) Li silicates with respect to crystalline SiO_2 and Li.

Figure 3.4b) shows the binary convex hull for the Li-Si composition line in the phase diagram, where the calculated crystalline and amorphous metastable phases are indicated. We note that $Li_{15}Si_4$ and $Li_{22}Si_5$ are both experimentally observed silicides[110, 111, 112], exhibiting formation energies of 1 meV/atom (within the accuracy of the employed DFT methodology) and 18 meV/atom above the hull, respectively. Similarly, we note that the amorphous states exhibit a high degree of metastability, ranging from 10-500 meV/atom, above the convex hull, however, the convex hull for the amorphous phases alone follow a similar trend as for their crystalline counterparts, as a function of Li content, in agreement with Kim et al.[108] This suggests that the *relative* difference in formation energy between compositions originates primarily from changes in short-range order Li-Si motifs. We note the importance of adapting the local structure to the chemical evolution, as simply replacing Si with Li on an fcc lattice is thermodynamically unfavorable.[113, 83] The formation energies,

in Fig. 3.4b), exhibit a minimum around $x = 0.75$ corresponding to the composition with the largest reaction enthalpy, with respect to the terminal phases (e.g. $yLi + Si \longrightarrow Li_ySi$). Amorphization of Si upon lithiation has previously been reported as an electrochemically-driven solid-state process[114, 115], where regions of high Li concentration contribute electrons to the antibonding sp^3 orbitals of Si, weakening the Si-Si bonds allowing the formation of metastable amorphous phases. We further note that the high degree of metastablility of the amorphous phases suggests that crystallization is limited by kinetics. Crystallization of the $Li_{15}Si_4$ phase, however, has been observed in experimental studies[116, 104] and rationalized as the interplay of higher diffusivity and the lack of Si-Si bonds in the structure. The formation energy plots in Figure 3.4 b) provide additional insight into the crystallization. After Li_xSi_{1-x} amorphization, further lithiation will trace the amorphous curve in Fig. 3.4 b), however when the driving force for lithiation reaches 0, near $x_{Li} = 0.78(3554mAh/g)$, further Li incorporation into the amorphous matrix is no longer energetically favorable. Hence, alloying with additional Li occurs only through a transformation from the amorphous to the crystalline phase, thus forming the $Li_{15}Si_4$ phase, which is the highest lithiated phase observed in experiments[102]. After c-$Li_{15}Si_4$ is formed, the formation of c-$Li_{21}Si_5$ is thermodynamically favorable, however, its absence in room temperature experiments suggests that the formation of $Li_{21}Si_5$ is kinetically hindered. This is in agreement with Kwon et al., who observe $Li_{21}Si_5$ only when lithiating between 100 - 120 °C[44].

As indicated by the dashed line in Fig. 3.4a), SiO_2 is thermodynamically driven to lithiate. The predicted lithiation process passes through ten 3-phase regions consisting of lithium silicides, silicon, and stoichiometric lithium silicates, until the end products Li_2O and $Li_{21}Si_5$ are formed. Following this compositional trajectory, we examine the calculated formation energies of a range of Li_ySiO_2 amorphous compositions, shown in Fig. 3.4c), and compare to the combined energy of the crystalline phases as obtained through the convex hull of the phase diagram (illustrated by the same color scheme in Figure 3.4a). Similar to the lithiation of Si, the amorphous structures are metastable as compared to the crystalline states and the overall shape of the lithiation convex hull is similar for both crystalline and amorphous phases. Again, the common trend suggests that the energy differences between the compositions are dominated by the local Li-Si-O environments, rather than longer range interactions, which are dissimilar in the crystalline and amorphous states. In the initial charging (lithiation of the anode), Si will be locally extruded within the native oxide layer, thereby forming lithium silicate environments. As shown in Fig. 3.4a), the formation of lithium silicates will occur for any composition of non-stoichiometric SiO_z, for $z < 2$, that may be found on the Si. Further charging will promote various Li silicide formation until Li_2O, $Li_{13}Si_4$, and $Li_{21}Si_5$ are formed. This agrees well with the analysis of local structural environments in amorphous Li_ySiO_z reported in Sec. 3.3 which predicts formation of short-range Li_2O domains past $Li_{2.9}SiO_2$. Although lithium silicides are predicted to form for $y > 2$, based on the phase diagram, pure Li-Si environments are scarce in the amorphous Li_ySiO_2 structures observed until $y = 4$ (Li_4SiO_2). We believe this may in part be due to artificial limitations in simulation unit cell size (see Section 3.2) and as such, not necessarily representative of real samples. Both clustering analysis as well as phase

diagram thermodynamics indicate that Si-only clusters are common to amorphous Li_4SiO_2 and Li_5SiO_2 (Fig. 3.3c-d)) compositions as well as amorphous $Li_{13}Si_4$ (Fig. 3.1). Both compositions lie within the phase triangle formed by the Li_4SiO_4, Li_2O, and $Li_{13}Si_4$, hence the Si dumbbells, Si_4 chains, Y shapes, and Si_5 rings present in $Li_{13}Si_4$ are expected. The silicides are distributed in clusters of size 1-6 evidenced by (relatively) large peaks around sizes 4 and 5 in Li_4SiO_2 and 1, 2, and 4 in Li_5SiO_2. We note that the composition Li_4SiO_4 forms a particularly stable node in the phase diagram, being present in 5 of the 10 phase triangles and having the lowest formation enthalpy, as seen in Fig. 3.4c). Indeed, Zhang et al.[67] observed the strong presence of both Li_2O and Li_4SiO_4 in lithiated SiO_2 - coated SiC nanowires. Similarly, Guo et al. [68] observed the presence of crystalline Li_4SiO_4 and Li_2O after the first cycle.

Voltage profile in amorphous Li_ySi and Li_ySiO_2

The equilibrium potential profiles of the systems were derived from the convex hull and phase diagram (section 3.3) as described in section 3.2. [98] Within the Materials Project, several stable crystalline lithium silicide phases exist; LiSi, $Li_{12}Si_7$, $Li_{13}Si_4$, and $Li_{21}Si_5$. Other crystalline Li_ySi phases have been experimentally observed, e.g. $Li_{22}Si_5$[110, 111, 112] which is found to be weakly metastable using the current computational methodology. In the calculated voltage profile for Li_ySi, Figure 3.5a), the crystalline states follow a stepwise curve from 0.39V to 0V. On the other hand, the lithiation potential of the amorphous lithium silicides is initially found to be higher than the crystalline counterparts, 0.50 V until $C = 954mAh/g$, where it drops below and smoothly follows the crystalline states. This is a similar trend to that found by Chevrier et al., with the exception that their initial lithiation potential is 0.43 V, a disparity, likely, arising from the difference in the method of obtaining the amorphous structures.[106]

Similar to the case of Si lithiation, the potential profile for Li_ySiO_2, shown in Figure 3.5b) was derived from the chemical potential of Li within the composition range between adjacent stable compositions. In the crystalline phases, the initial voltage of SiO_2 exceeds that of Si by almost 1 V. As lithiation progresses and a Li-Si environment forms, the voltage drops to values closer to that of Li_ySi. The amorphous phases follow a similar trajectory, initially exhibiting a potential of 1.2 V, and ending at 0.06 V. These findings agree qualitatively with experimental studies on bulk SiO_2 which exhibit voltage profiles higher than that of Si, between 1.0-1.5V. [62, 118, 119] The preferred equilibrium phase sequence upon lithiation shows the strength of, and preference towards, the formation of Li-Si and Li-O bonds at the expense of Si-O bonds. The formation of $Li_{13}Si_4$, $Li_{21}Si_5$, and Li_2O local environments is favored, even in the first charge, if the anode voltage drops below $\approx$ 100 mV vs Li/Li^+. During discharge, the lithiated composite (surface phase and bulk) will delithiate in order of increasing potential such that the lithium silicides within the oxide layer and silicides in the bulk Si will delithiate first, forming Li_ySi and Li_4SiO_4. Only after the Li_ySi phases have been completely delithiated will the Li_4SiO_4 be delithiated to form SiO_2. However, in practice, limits placed on cycling window (e.g. 3 and 4.2V in LiCoO2 based batteries[120])

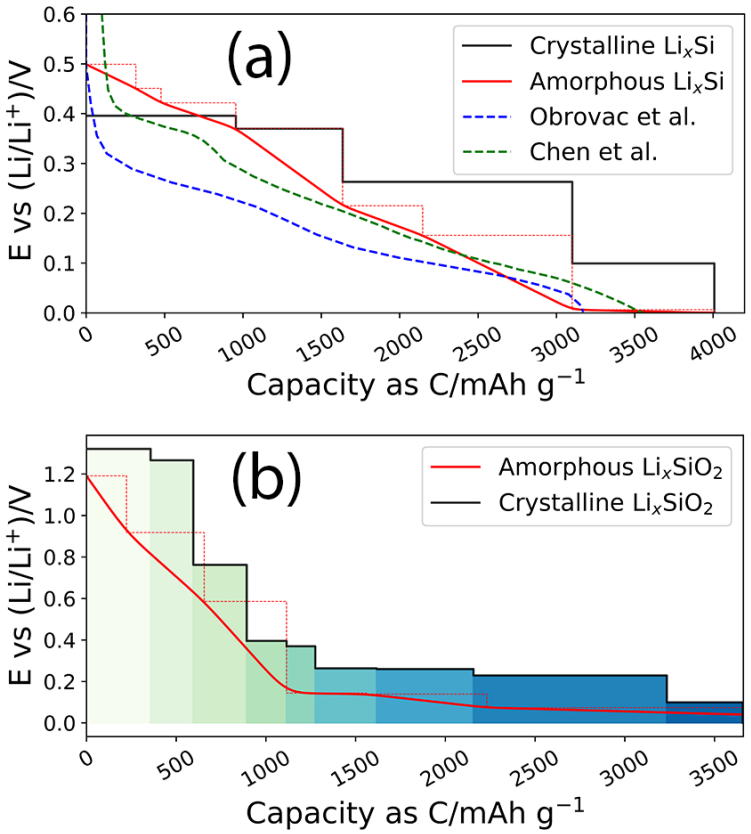

Figure 3.5: Calculated electrode potential profile (E vs (Li/Li$^+$)/V) for crystalline and amorphous a) lithium silicides in comparison with experimental curves [117, 54] and b) lithium silicates. The dashed red line in both a) and b) corresponds to the voltage of the amorphous phases as calculated from the convex hull before smoothing.

may result in loss of energy density if the delithiation potential of the silicates is not reached, rendering the lithiation of the silicates functionally irreversible. This is in agreement with experimentally observed capacity losses, from the formation of inactive/irreversible Li_ySiO_z during the cycling of Li_ySiO_z[121], SiO[122], and SiO_z[62, 123]. It is important to note that we do not explore the SiO_2/Si interface in this study and the aforementioned conclusion is drawn from the voltage profile of the bulk silicides and silicates.

Li diffusion in amorphous Li_ySi and Li_ySiO_2

Calculated Li diffusivities are shown in Figure 3.6 and tabulated with corresponding errors in Table 3.1. Previous experimental reports of lithium diffusivity in amorphous Si vary between 10^{-16} cm^2 s^{-1} - 10^{-7} cm^2 s^{-1}.[70, 71]. We find self-diffusivity values near this range for all of

Table 3.1: Calculated Li self-diffusion coefficients in lithium silicides and silicates. Reported errors are statistical errors from the non-linear fit to the Arrhenius equation.

	E vs $(Li/Li^+)/V$	Diffusivity $(D/cm^2\,s^{-1})$	Fit Error $(cm^2\,s^{-1})$
LiSi	0.32	1.49E-08	6.35E-08
$Li_{12}Si_7$	0.28	4.65E-09	1.31E-08
$Li_{13}Si_4$	0.03	2.38E-08	2.44E-08
$Li_{21}Si_5$	0	1.96E-07	2.87E-07
$LiSiO_2$	0.75	2.58E-11	5.30E-14
Li_2SiO_2	0.41	1.08E-09	3.54E-10
Li_3SiO_2	0.23	2.44E-08	3.28E-09
Li_4SiO_2	0.13	1.90E-08	5.99E-10
Li_5SiO_2	0.09	2.21E-09	2.31E-10

the amorphous lithium silicides, with a general upward trend of diffusivity with increased Li insertion (decreasing voltage), in agreement with studies by Johari et al. and Wang et al. who find diffusivity increasing to $10^{-6}\,cm^2\,s^{-1}$ in $Li_{15}Si_4$ from $10^{-9}\,cm^2\,s^{-1}$ in Si, by studying the inter-diffusion of separate Li and Si layers using AIMD at high temperature. Intuitively, as percolating Li-rich environments and pathways are formed within the amorphous matrix (cluster analysis in Sec. 3.3), we expect the Li diffusivity in Li-rich Si to approach that of amorphous Li-metal. Literature values for Li self-diffusivity in Li metal range widely from $10^{-10}\,cm^2\,s^{-1}$ to $10^{-6}\,cm^2\,s^{-1}$, [124, 125, 126], presumably for polycrystalline samples. In the amorphous silicates, the Li self-diffusivity follows a different trend with composition. For $1 \leq y \leq 2$ ($LiSiO_2$ to Li_2SiO_2) it increases by 2 orders of magnitude. Visual inspection of the Li trajectories in $LiSiO_2$ shows expected high Li residence time near O and, with large plateaus within the MSD, for each individual Li atom, followed by Li hops to neighboring Si or O, indicating strong attraction between Li-O and Li-Si which increases the barrier for Li movement. However, once sub-stoichiometric SiO_z and Si environments are formed, the Li barrier to migration is lowered as Li moves through increasingly Li-rich environments. At $y = 3.0$, we expect silicide domains corresponding to an average composition of $Li_{12}Si_7$, which exhibits a similar Li diffusivity to that found in the composite lithium silicate matrix. This confirms that the formation of these local, yet connected domains, enable faster Li diffusion. As discussed previously, the Li_4SiO_2 and Li_5SiO_2 compositions share similar clustering patterns to $Li_{13}Si_4$ which gives rise to similar Li diffusion behavior. Overall, the trend shows that the presence of SiO_2 is likely to have a detrimental effect on overall rate behavior of a Si-based anode, especially at low levels of surface oxide lithiation. Irreversible formation of Li_2O environments will present a sink for Li inventory while formation of Si and lithium silicide environments will result in a higher Li diffusivity in subsequent cycles.

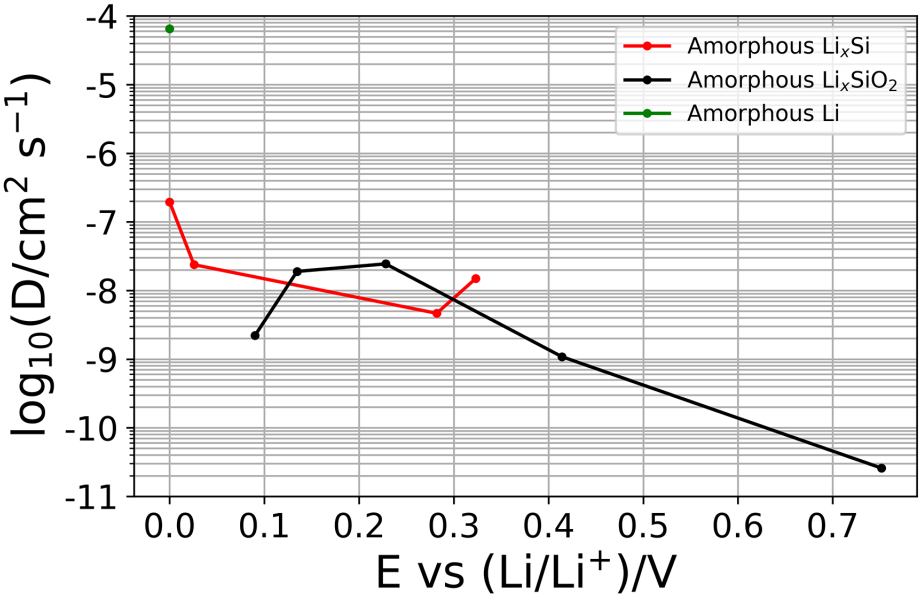

Figure 3.6: Room temperature Li self-diffusion coefficients in amorphous lithium silicides and lithium silicates as a function of electrode potential E vs (Li/Li$^+$)/V

3.4 Summary

We present first-principles calculations of amorphous Li$_y$Si and Li$_y$SiO$_z$, and evaluate their structural evolution, electrochemical voltage, and Li diffusion properties, as a function of Li concentration. The local environments in Li$_y$Si compare well with existing experimental results from electrochemical lithiation. Similar Si short-range motifs are formed in the amorphous lithium silicides as in the crystalline phases, showcasing the preference for formation of 5-membered rings, Y-shapes, and Si dumbbells. Thermodynamic lithiation potentials show that amorphous SiO$_2$ lithiates at a higher potential than Si, initially approximately 1.2 V vs Li metal. The structural evolution of the amorphous lithium silicates corroborates the thermodynamic lithiation pathway as evidenced in the phase diagram, showing strong preference towards the formation of Li-O and Si-Si bonds. Aggregation of Si in the amorphous lithium silicates also correlates well with the aggregation of the silicides within the same phase triangle. Initial electrochemical activity of SiO$_2$ is found at 1.3 V, as compared to $\sim$ 0.4 V in Si. Diffusivities of Li in the amorphous silicides are found to be high (order 10^{-9} cm^2 s^{-1} - 10^{-7} cm^2 s^{-1}), increasing with composition, while the amorphous silicates start low ($\sim 10^{-11}$ cm^2 s^{-1}), increasing to 10^{-8} cm^2 s^{-1}. Formation of percolating Li networks at higher Li concentrations coincide with higher Li transport in both the silicides and silicates. In conclusion, we find that SiO$_2$ is thermodynamically driven to lithiate, by extrusion of Si

and increased formation of Li-O bonds. SiO_2 also exhibits two orders of magnitude lower Li diffusivity at low Li concentration. Hence, excluding explicit interaction with the liquid electrolyte, we find that the SiO_2 surface may impede Li transport at low Li contents and contribute to loss of Li inventory through the formation of Li_2O during prolonged cycling.

Chapter 4

Case Study of the Silicon-Tin alloy system

This chapter contains unpublished work and research from publications in preparation.

4.1 Introduction

Increased utilization of renewable, intermittent energy resources and large-scale electrification of vehicles require continued innovation in energy storage materials and technologies. Today, commoditized Li-ion secondary batteries provide the vast majority of new installations, however, improvements in active materials are still desirable. Promising electrode formulations, such as Si-based alloy electrodes can improve the energy density of the anode, with realizable gravimetric capacities up to $3579\,\mathrm{mAhg^{-1}}$, significantly higher than graphite electrodes ($372\,\mathrm{mAhg^{-1}}$).[9, 127, 21] While much progress has been made towards the commercialization of Si-based anodes, cycle life limitations and capacity fade stemming from particle cracking, non-passivating SEI formation, and poor lithiation kinetics are still concerns.[20, 128, 129] Notably, strategies to mitigate one of these challenges often end up exacerbating others. For instance, modifying particle morphologies to decrease mechanical stresses and prevent particle cracking enhances the capacity loss due to increased surface area exposed to non-passivating SEIs[130, 128]. Tailoring the chemistry of the anode by alloying to form metal silicides or by developing composites can mitigate the volume expansion that causes the mechanical stresses, but as of yet, alloys have presented poor coulombic efficiency.[23, 21, 20]

Nevertheless, modifying the chemistry of the anode presents a practical method of tuning the performance of the amorphous Si-anode. In particular, alloying Si-anodes with Sn has garnered interest due to Sn's high innate volumetric capacity.[131, 132, 133] Tin also possesses a higher electronic conductivity ($\sim 9.2 \times 10^4\,\mathrm{S\,cm^{-1}}$) and Li-diffusion rate than Si, which may improve anode charge rates.[134] Several studies have demonstrated improved cycling for Si-Sn alloys and nanocomposites.[135, 23, 136, 137, 138, 139, 140] Hatchard

et al.[135] employed combinatorial sputter deposition to synthesize amorphous Si-Sn films, rapidly exploring a wide range of compositions. Deposited films exhibited a significant improvement in cycling stability across all compositions, although they found < 40 atom % Sn to be ideal. Improvements to capacity retention were attributed to the formation of a single $Li_nSi_{(1-z)}Sn_z$ phase during lithiation and delithation[23], as compared to the 2-phase lithiation observed in Si between a-Li_xSi ($0 \leq x \leq 3.75$) and c-$Li_{15}Si_4$. Yao et al.[136] reported excellent cycling stability in Si-Sn nanocomposites synthesized through chemical reduction, observing a reversible capacity of $700\,mAhg^{-1}$ over 200 cycles. Xu et al.[139] demonstrated Si-Sn nanocomposites, synthesized through mechanical milling, with better 1st cycle coulombic efficiency and capacity retention of $\sim$ 80% over 50 cycles as compared to $\sim$ 20% in mechanically milled Si. Relevant to kinetics, Wang et al.[141] reported nanobranched Si-Sn nanocomposites exhibiting $\sim$ 2.45 times higher Li-diffusivity than in pure, unmodified nanobranched Si. With numerous other publications reporting improved cycling and rate performance in recent years, it is fair to suggest that Si-Sn based alloy electrodes present a promising path forward.

Specifically, from a rational design perspective, it is desirable to address the fundamental mechanisms underlying possible improvements in performance. No work, to date, elucidates the Li diffusion coefficients in the Li-Si-Sn alloy system. Furthermore, no computational efforts have been undertaken to study the thermodynamics of lithiation and structural evolution of the Si-Sn system. While the reported Si-Sn immiscibility[137, 142, 136] has not been shown to be detrimental to performance and has even been used as a route for Si-Sn nanocomposite formation, a bottomup, atomistic understanding of the system's structural evolution will aid in optimizing Sn-alloying. Here, we present a combined ab-initio Molecular Dynamics (AIMD) and density functional theory(DFT) study of the thermodynamics across the amorphous Li-Si-Sn system to improve our understanding of the relative stabilities, diffusivities, and lithiation behavior as a function of Sn-alloying composition.

4.2 Methods

To explore Li diffusion and phase evolution of the Si-Sn alloy system as a function of alloy composition and Li content, we employ first-principles calculations to sample quasi-amorphous structures, low-temperature energetics, and observe the dynamics related to diffusion. Calculations were performed using the Vienna Ab-initio Simulation Package (VASP)[90, 91], with projector augmented-wave (PAW) potentials[92] and the Perdew-Burke-Ernzerhof (PBE) generalized-gradient functional (GGA).[93] Calculation parameters were chosen to be consistent with those of the Materials Project[143], which have been extensively benchmarked and are documented in the Python Materials Genomics (pymatgen) package under the MPRelaxSet, MPStaticSet, and MPMDSet.[33] As a brief summary of these parameters, geometry optimizations were performed with a plane wave cutoff of 520 eV, with a minimum reciprocal lattice k-point density of 64 per $Å^{-3}$. Single-point calculations were performed with the same cutoff but an increased k-point density of 100 per $Å^{-3}$.

Ab-initio molecular dynamics (AIMD) simulations were performed using a 2 fs time-step with a plane wave cutoff of 400eV and one gamma centered k-point.

Ab-initio Molecular Dynamics (AIMD) were employed to emulate amorphous structural configurations through a simulated 'melt-quench' process[37, 38, 41]. Cubic simulation cells of at least $\sim$ 100 atoms were generated using packmol [32]. The aforementioned workflow is implemented in mpmorph (`http://github.com/materialsproject/mpmorph`) using pymatgen[33], fireworks[94], and atomate[95]. All thermodynamic calculations utilized direct DFT structure optimization for quenching. More stable structures were obtained from AIMD quenching, at a rate of $3.97 \times 10^{14}\,\mathrm{K\,ps^{-1}}$, using an NVT thermostat, followed by DFT structure optimization, and reveal the tendency for phase segregation. Simulation cells were generated for various compositions within the Li-Si-Sn chemical system. Throughout the paper, we denote the chemical formulas as $Li_nSi_{1-z}Sn_z$ for ease of discussion when referring to moles of Li atoms alloyed per mole of the starting electrode.

Investigations of the diffusion kinetics were conducted using a minimum of three AIMD simulations at 1500 K, 1250 K, 1000 K, 750 K, and 500 K. Simulation cells were re-equilibrated at the desired temperature through volume rescaling of short timescale runs until an external pressure of 0 ± 5 kbar was achieved. Diffusion coefficients were fit from the hybrid-ensemble time-averaged mean squared displacement (MSD)[40] and room temperature diffusion coefficients were extrapolated assuming Arrhenius kinetics. To ensure sufficient events in the diffusive regime to compute appropriate MSDs, we impose a minimum diffusion distance for each specie in the trajectories. Calculations not meeting the minimum MSD or exhibiting a statistical error greater than the diffusivity are discarded. In the case of Li, we use a minimum MSD of 3 $\mathrm{Å}^2$, as compared to the maximum MSD within the ballistic regime of approximately 0.3 $\mathrm{Å}^2$.

4.3 Results and Discussion

Impact of Sn Alloying on Intrinsic Li Diffusivity

Figure 4.1 shows the room temperature Li self-diffusion coefficients for four systems spanning the Li-Si-Sn compositional space, obtained from the extrapolation of the Arrhenius fit to AIMD results (see Methods, Sec. 4.2) at higher temperatures. Comparing the pure Si and Sn phases, in general, the Li-diffusivity in Li_nSn phases are higher than their Li_nSi counterparts. Li diffusion in amorphous Sn at low lithiation is nearly 40 times faster than for amorphous Si, which qualitatively agrees with literature assessments of Li diffusivity in the two systems.[137] We find that the Li-diffusivity in Li_nSn decreases with increased Li concentration, however, we note that for $n = 2 - 3$ (66-75 atom % Li), some crystallization was observed at temperatures $\leq 750K$, which may contribute to the decrease in kinetics. Turning to the amorphous alloys of $Si_{(1-z)}Sn_z$, we find an improvement in Li diffusion when alloying with Sn up to approximately 38%. At 10% Sn content ($Li_nSi_{0.9}Sn_{0.1}$), the diffusion for $n \leq 1.5$ is equal to Li_nSi, but surpasses the Li diffusion in the Li-Si system by 1.5 to

3x for $n >= 2$ (66 atom % Li). We find amorphous $Li_nSi_{0.62}Sn_{0.38}$ to exhibit improved Li kinetics for all calculated compositions, ranging from 1.5 to 5x greater, as compared to an amorphous Si host.

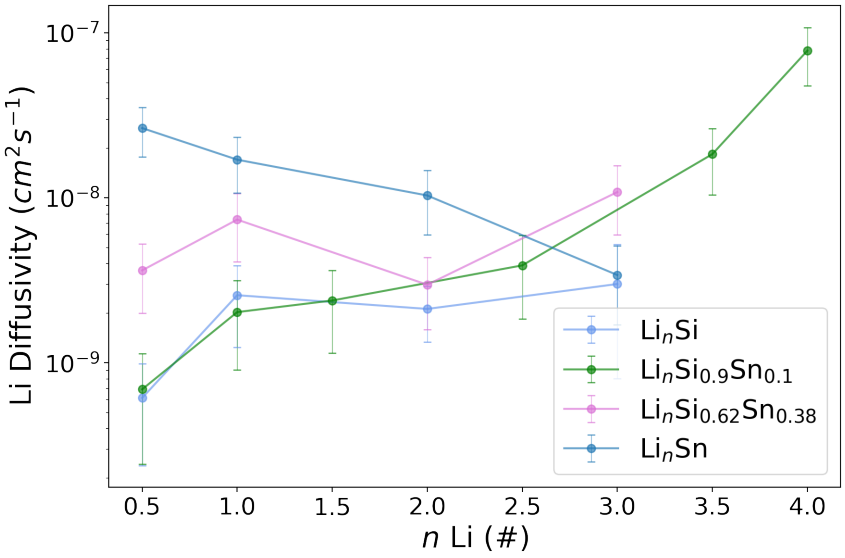

Figure 4.1: Evolution of Li self-diffusivity for various amorphous Si-Sn alloy materials. Error bars on estimated Li-diffusion coefficients account for the uncertainty resulting from time-averaging, regression, and extrapolation.

It has been previously reported that there is a strong correspondence between the melting temperature and activation energy for diffusion in metals.[144, 145] From the experimental phase diagrams, we find that for Si, the addition of Li lowers the melting point temperature, T_m, while in Sn, the addition of Li increases T_m. Thus, we may attribute the higher Li diffusivity of Li_nSn in part to the lower melting point of tin and the lithium stannides. We also note that the melting temperatures of Li_3Si and Li_3Sn are nearly equal (982K and 993K, respectively), and in our calculations, we indeed find similar Li self-diffusion coefficients in Li_3Si and Li_3Sn.[146, 147]

Phase Evolution as a function of Si-Sn intermixing and lithiation

In the following we examine the effect of lithiation on the phase evolution and kinetics within the Li-Sn-Si system. It is well documented that the Si-Sn system presents an immiscibility gap below 231.9 K across the entire Si-Sn composition range.[142] In agreement with experimental findings, the 0K Li-Si-Sn phase diagram, constructed from calculations obtained from the Materials Project, shows no stable crystalline Si-Sn phases (see Figure 4.2a). All $Si_{(1-z)}Sn_z$ phases are found above the convex hull and are thermodynamically metastable,

which means that any Si-Sn alloy synthesized will achieve lower free energy by forming distinct Si and Sn phases.

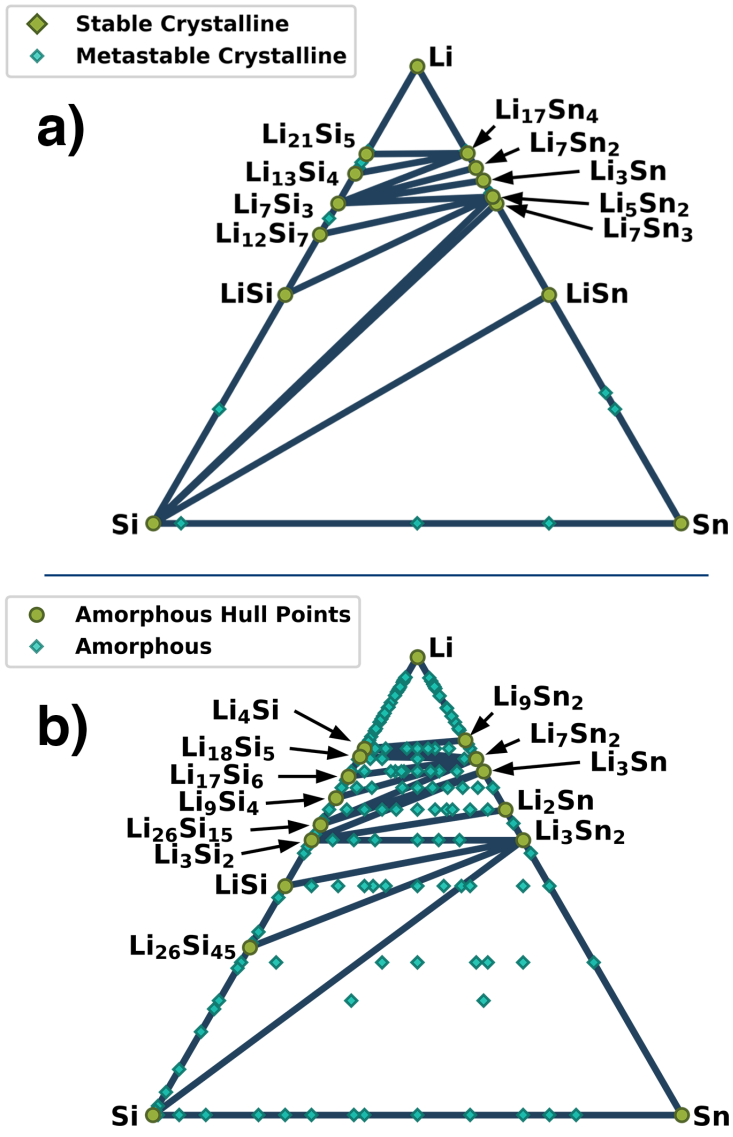

Figure 4.2: a) Crystalline phase diagram of the Li-Si-Sn chemical system. b) Amorphous convex hull with sampled off-hull amorphous compositions marked with diamonds.

Furthermore, no stable, ternary crystalline Li-Si-Sn phases are found on the Materials Project, indicating that Li-Si-Sn alloys may all be metastable (barring insufficient exploration of the chemical and structural Li-Si-Sn space). We note that the absence of low-temperature

stable $Si_{(1-z)}Sn_z$ phases does not preclude experimental observation at higher temperatures, as entropic contributions may stabilize the alloy and kinetic effects inhibit the decomposition. Phrased alternatively, any binary Si-Sn as well as ternary alloy in the Li-Si-Sn system at low temperature will be thermodynamically predisposed to phase separate into pure crystalline Li-Sn, Li-Si and pure Si/Sn, depending on composition.

Assuming slow decomposition into the stable crystalline phases, we assess the relative stability of the amorphous phases within the exclusively amorphous Li-Si-Sn system using the average formation energy of each sampled composition. Figure 4.2b shows the resulting convex hull using only the sampled amorphous structures and BCC Li. The amorphous Li-Si-Sn system tracks its crystalline counterpart, with no stable Si-Sn binary or Li-Si-Sn ternary phases. As with their crystalline counterparts, all alloyed amorphous $Si_{(1-z)}Sn_z$ phases are predicted to be thermodynamically metastable at low temperatures.

The tendency towards phase segregation and preferential bonding as a function of lithiation is also observed upon careful examination of the AIMD trajectories as well as in the amorphous structures obtained from the AIMD melt-quench procedure (see Sec. 4.2). As a general note of caution, our limited sized simulation cells cannot completely capture phase segregation, especially at high Li content, where there are only a few Si and Sn atoms, however trends can be observed. While our glassy liquid melts of $Si_{(1-z)}Sn_z$ at 5000K appear homogeneous on visual inspection, quenching results in in-homogeneous atomic arrangements with large clusters of Si and Sn, as seen in Figure 4.3a. Such local phase segregation was observed in amorphous samples relaxed by both direct DFT structure optimization and AIMD quenching. At low temperatures, we observe short-range segregation across the entire composition range, $0.1 \leq z \leq 0.9$ in $Si_{(1-z)}Sn_z$ such that the Si-Sn system favors the formation of Si-Si and Sn-Sn bonds over Si-Sn bonds. The coordination numbers (Fig. 4.3 f) confirm this trend, with Si-Sn coordination numbers much lower than that of Si-Si and Sn-Sn interactions. Interestingly, the separation of Si and Sn diminishes with lithiation (Fig. 4.3b-e), disappearing in the highly lithiated compositions, as the Li acts like a 'glue' between Si and Sn, through the formation of more favorable Li-Si and Li-Sn bonds. In the early stages of lithiation, Li primarily forms bonds with Sn, as seen by the more rapid decrease in Sn-Sn coordination (Fig. 4.3f) and the increase in Li-Sn bonding (Fig. 4.3g), while breaking up the Si-Si clusters into smaller clusters or longer chains. Further lithiation favors Si clusters of 2-5 atoms, similar to the Si aggregates observed in the binary Li-Si system [41]. At higher stages of lithiation ($n > 2$ in $Li_nSi_{(1-z)}Sn_z$), most Si and Sn atoms exist as isolated atoms, only coordinated with to Li.

A summary of the electrode characteristics for select crystalline and amorphous $Si_{1-z}Sn_z$ compositions is presented in Table 4.1. The lithiation voltage of crystalline phases is higher than the amorphous phases in both Si and Sn, indicative of a more unstable delithiated state. The average lithiation voltage is found to increase with increasing Sn content, with the lowest potentials for pure Si. This is congruent with experimental reports on $Si_{(1-z)}Sn_z$, for $0 \leq z \leq 0.45$ [135, 20] where an average lithiation voltage of $\sim 0.2\,\mathrm{V}$ is found for Si, increasing to $\sim 0.24\,\mathrm{V}$ at $Si_{0.55}Sn_{0.45}$. With no stable ternary phases, the lithiation voltage profile for the Si-Sn system is a composite of the individual Si/Sn alloying voltage profile,

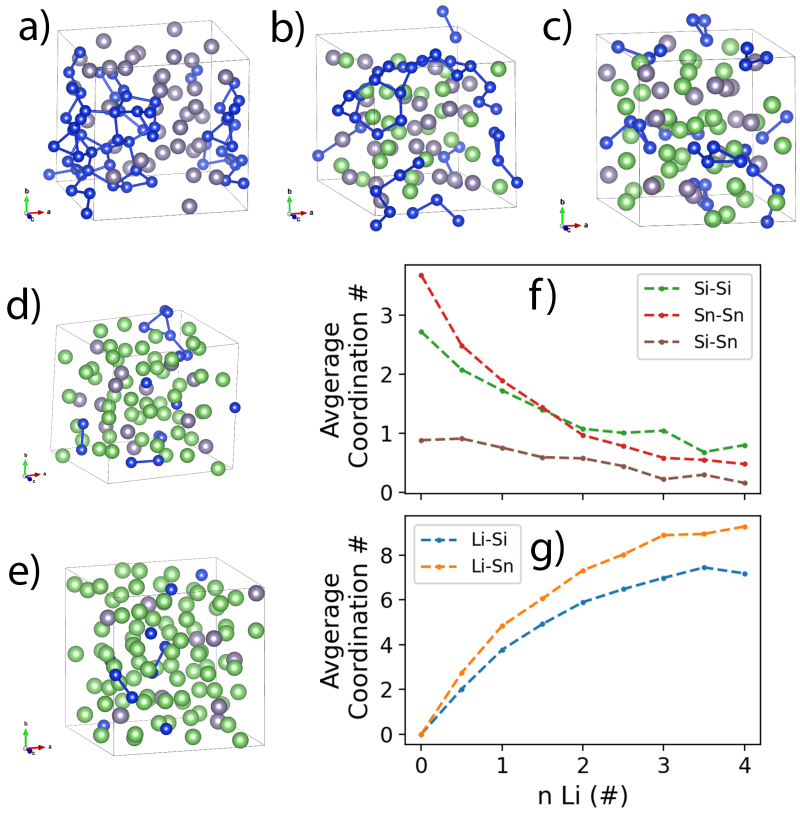

Figure 4.3: a) Representative Unit cells of various lithiation stages of $Li_nSi_{0.5}Sn_{0.5}$ a) $n = 0$, b) $n = 0.5$, c) $n = 1$, d) $x = 2$, e) $x = 4$. Li, Si, and Sn atoms are depicted as green, blue, and grey spheres, respectively. Average coordination numbers for f) host atoms (Si and Sn) and g) Li are plotted as a function of the lithium content.

such that the characteristic potentials of Li_nSi and Li_nSn are combined in descending order; Capacities at each voltage are dependent on initial Si and Sn content. The higher lithiation potential of Sn predicts a preferential bonding of Li within Sn-rich regions before Si regions, commensurate with the coordination evolution in Figure 4.3

Having explored the thermodynamics of the Li-Si-Sn system, and established its clear tendency towards phase segregation into Li-Si and Li-Sn phases - however with a higher degree of intermixing with higher Li content, we turn towards kinetics. In these glassy materials, the diffusion of the host atoms, Sn and Si, occurs through Li-Si and Li-Sn bond-breaking, bond-forming events such that the diffusion of species is necessarily co-correlated.[148] Figure 4.4 illustrates the diffusivity of Si and Sn in a range of Li-Si-Sn amorphous alloys, compared to the Li-Si and Li-Sn binaries. We observe that Si exhibits very low self-diffusivity, while the self-diffusivity of Sn is orders of magnitudes higher in the Sn-rich regimes - a trend that

Table 4.1: Electrode Characteristics for various Si-Sn alloys

	Volume Expansion (%)	Average Voltage (E)	Lithiation Capacity (# Li)	Specific Capacity ($mAhg^{-1}$)	Volumetric Capacity (AhL^{-1})
Crystalline					
Si	0-290	0.28	4.2	4020	2350
$Si_{0.9}Sn_{0.1}$	0-270	0.30	4.2	3040	2310
$Si_{0.62}Sn_{0.38}$	0-220	0.34	4.2	1820	2200
$Si_{0.5}Sn_{0.5}$	0-210	0.36	4.2	1550	2150
Sn	0-160	0.44	4.3	960	1990
Amorphous					
Si	0-400	0.20	4.0	3820	2090
$Si_{0.9}Sn_{0.1}$	0-350	0.21	4.1	2920	2020
$Si_{0.62}Sn_{0.38}$	0-320	0.22	4.2	1800	1970
$Si_{0.5}Sn_{0.5}$	0-300	0.23	4.2	1560	1940
Sn	0-260	0.25	4.5	1020	1870

is ameliorated with mixing of Si and Sn.

The dramatic and consistent modulator of Si and Sn diffusivity is lithiation. The Si-diffusivity initially trends upwards with Li concentration in Li_nSi and $Li_nSi_{0.9}Sn_{0.1}$, then decreases. By contrast, in $Li_nSi_{0.62}Sn_{0.38}$, Si-diffusivity decreases with lithiation. Sn-diffusivities in both $Li_nSi_{(1-z)}Sn_z$ and Li_nSn decrease with increasing Li concentration. The lithiation of Sn reduces the Sn diffusivity by two orders of magnitude. Combined, these trends confirm that host atom diffusion is correlated to Li diffusion at low Li concentrations.

Assuming that large-scale structural reorganization cannot occur in a kinetically limited system, where Sn and Si diffuse slowly at low temperatures and shorter time scales, we find it reasonable to deduct that nano-sized regions of a-Si and a-Sn that form during synthesis will remain at low temperatures. In such nanocomposites, Si's low lithiation potential and high specific capacity act as a storage mechanism for Li while the Sn primarily serves as a pathway for faster Li diffusion and secondary (less thermodynamically stable) storage of Li. Phrased more colloquially, and from a Li storage and transportation perspective, we visualize the composite system as Si-rich 'parking lots' and Sn-rich 'freeways'. With low

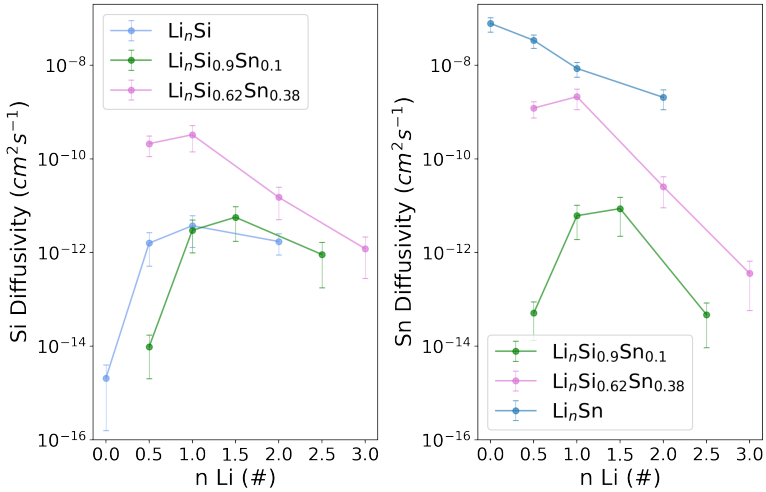

Figure 4.4: a) Si-Diffusivity and b) Sn-Diffusivity in various $Li_nSi_{(1-z)}Sn_z$ alloys

Si and Sn diffusivities at high lithium content, Si and Sn from Li_nSi and Li_nSn are not expected to significantly inter-diffuse, and the nanocomposite structure may be maintained during cycling.

At high lithiation levels, the energy above hull for the amorphous ternaries may be sufficiently low (see Figure 4.5), especially when considering free energy contributions from the entropy of mixing, to maintain a well-mixed phase throughout synthesis. Non-equilibrium materials processing techniques utilizing rapid cooling rates, such as quenching or sputtering, to prevent phase transformations may be able to form ternary a-$Li_nSi_{(1-z)}Sn_z$ phases. Combined with the low Si and Sn diffusivities, this hints at possible synthesis routes for homogeneous Si-Sn alloy through the delithiation of $Li_nSi_{(1-z)}Sn_z$ which should be beneficial as homogeneous $Si_{(1-z)}Sn_z$ materials present an increased Li-diffusivity as compared to pure Si. As the Si and Sn diffusivities are low in these amorphous ternary alloys, the formation of crystalline phases may be suppressed. Furthermore, crystalline phases such as the c-$Li_{15}Si_4$ phase, which is found to be detrimental to Si cycling, may be avoided.

4.4 Conclusion

We present an ab-initio investigation of the impacts of Sn-alloying in Si anodes for Li-ion energy storage applications. We find that the introduction of Sn improves the Li-diffusion kinetics as compared to pure Si, which correlates well with the inverse relationship between melting temperature and ionic diffusivity. This suggests that identifying alloys with low

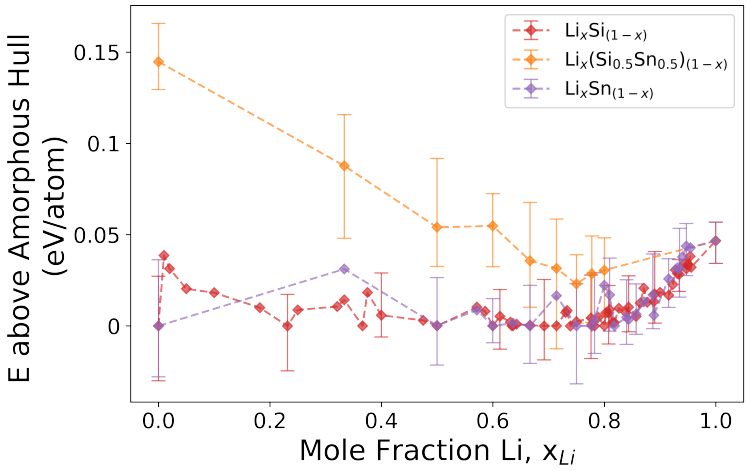

Figure 4.5: Energy above the amorphous hull for a-Li_nSi, a-$Li_nSi_{0.5}Sn_{0.5}$, and a-Li_nSn

melting temperatures may be fruitful for targeting high rate capability anodes. Our findings indicate that Li alloying with the Si-Sn electrode is coupled with the breaking of Si-Si bonds, while at higher charge, Li diffuses in Li-coordinated Sn-rich environments. The introduction of Sn decreases the number of Si-Si bonds, which, while using Si-rich environments for storage, improves overall Li diffusivity. Additionally, decreased Si-diffusivity at high lithiation may suppress the formation of crystalline stable phases, such as c-$Li_{15}Si_4$. It is worth noting that while amorphous Si-Sn is prone to short-range order Sn-rich and Si-rich regions, both offer improvements to electrode characteristics, providing high capacity storage (Si 'parking lots') with fast transport routes (Sn 'freeways'). Finally, a decrease in the driving force for phase segregation is found at higher lithium content, hinting at possible synthesis routes for more homogeneous Si-Sn alloys through the electrochemical delithiation of amorphous Li-Si-Sn alloys.

Chapter 5

High-throughput investigation of lithiation behavior of binary Si alloys

This chapter contains unpublished work and research from publications in preparation.

5.1 Introduction

Lithium-ion secondary batteries are currently the dominant energy storage technology for consumer electronic devices and are increasingly in demand as the adoption of electric vehicles and renewable energy rises.[149, 150, 151] Current generation Li-ion batteries, utilizing graphite intercalation materials, are nearing their limits for energy storage, and continued improvements in negative electrode energy density require the transition to alternative anode materials.[5] Silicon has been suggested as a replacement for graphite in Li-ion batteries due to its high theoretical capacity in conjunction with its high abundance and global production. Amorphous Si delivers up to $3579\,\mathrm{mAhg}^{-1}$ when cycled at room temperature. However, concurrently Si suffers from electrode performance degradation resulting from the significant volumetric expansion associated with Li alloying[9, 103, 102, 116] as well as the formation of an unstable solid electrolyte interphase (SEI) which leads to continuous electrolyte decomposition and loss of Li inventory.[129, 152] Strategies to mitigate volumetric expansion primarily involve nanostructuring to introduce void space, allowing for particle swelling and reducing internal stress during cycling.[9, 20] However, nanostructuring also accelerates electrolyte reduction by increasing the contact area between the active material and electrolyte, resulting in low initial coulombic efficiency.[128] Amorphous Si has yielded marked improvement in mechanical stability due to the absence of phase separation during lithiation, reducing stress originating from phase boundaries between distinct lithiated phases.[153] Attempts to promote the formation of a suitable SEI have found improved capacity retention and extended cycle life but still fall short of requirements for commercial application.[14, 13] Alloying Si with other elements is another effective strategy to mitigate volume expansion and modify SEI formation by modulating lithiation voltage, volumetric

expansion, surface reactivity, and phases formed during cycling. [154, 139, 155, 25]

Alloyed elements are either active or inactive depending on their reactivity with Li. Elements that form stable binary phases with Li (such as Si, Ge, Sn, and Sb) are considered active, while those that do not form stable binaries (e.g. Ti, Cr, Mn, and Ni) are deemed inactive.[21, 20] The alloys of active elements have received much attention, as the electrochemical characteristics of alloyed active components can be markedly different from the individual elements.[26, 20] Additionally, the presence of a third element in these glasses is associated with increased fracture toughness, leading to higher mechanical stresses during cycling which suppresses the formation of the crystalline $Li_{15}Si_4$ phase, which is known to contribute to electrode cracking and voltage hysteresis.[153, 117] Although high stress from lithiation typically results in the fracturing of Si, amorphous materials such as metallic glasses exhibit higher yield strength, fracture toughness, and resistance to crystallization and may be capable of withstanding forces associated with lithiation.[156, 157, 158] While the alloying of inactive elements, especially at high concentrations, is detrimental to energy storage capacity, the inclusion of these components lowers the maximum volumetric expansion, similar to the inclusion of void space through nanostructuring.[25] Consequently, compared to a-Si with a depth of charge restricted to similar volumetric expansion, alloys yield a decreased average voltage and increased energy density.

While much work and several extensive reviews are devoted to the performance of of Si-based alloy electrodes[21, 20, 159], most predictions of lithiation behavior use the known crystalline phases from the Materials Project[143, 43, 20]. While this approach may be sufficient in systems with high ionic diffusivity, such as Sn, which lithiate through a series of crystalline phases, ionic diffusivity in crystalline Si is sluggish and amorphization is pervasive[20, 154]. Therefore, examining the crystalline polymorphs likely results in an incomplete picture of the systems, since only a handful of lithiated compositions are represented in the calculation set. An understanding of formation of binary Si alloys and their corresponding lithiated amorphous alloys is necessary when designing alloying and conversion electrodes. In this work, we present a comprehensive ab-initio study of the thermodynamics and lithiation characteristics of amorphous binary Si-X alloys and/or compounds. Although some elements may be unsuitable for use in Li-ion batteries due to their toxicity, high cost, or low abundance, we include these elements for completeness and comparison.

5.2 Computational Methodology

Methods

For all elements investigated, we sampled amorphous structures using ab-initio molecular dynamics (AIMD) and Density Functional Theory (DFT), similar to previous work on the Li-Si and Li-Si-O systems.[41] High-throughput workflows were implemented in the mpmorph[37] software package using the atomate[95], fireworks[94], and pymatgen[33] python packages. A modification to the volume rescaling approach was necessary for robust and

accelerated convergence of equilibrated liquid melts. Density convergence was achieved by running three parallel AIMD simulations with different densities, regression analyses of the Birch-Murnaghan EOS (shown in eqn 5.1), and identifying V such that $P(V) = 0$.[34, 160].

$$P(V) = \frac{3B_0}{2}\left[\left(\frac{V_0}{V}\right)^{\left(\frac{7}{3}\right)} - \left(\frac{V_0}{V}\right)^{\left(\frac{5}{3}\right)}\right]\left\{1 + \frac{3}{4}(B_0' - 4)\left[\left(\frac{V_0}{V}\right)^{\left(\frac{2}{3}\right)} - 1\right]\right\} \quad (5.1)$$

All Density Functional Theory (DFT) calculations were performed using the Vienna Ab-initio Simulation Package (VASP)[90, 91], with projector augmented-wave (PAW) potentials[92] along with the Perdew-Burke-Ernzerhof (PBE) generalized-gradient functional (GGA)[93] and the GGA+U extension[96] where applicable. The Python Materials Genomics (pymatgen) package was used to generate input files with calculation parameters (U values, convergence criteria etc) consistent with those of the Materials Project.[33, 143] Structure optimizations were performed using the MPRelaxSet within pymatgen, with a plane wave energy cutoff of 520eV with a minimum reciprocal lattice density of 64 per Å^{-3}. AIMD simulations utilized a plane-wave cutoff of 400 eV, one Γ centered k-point, and a time step of 2 fs as documented in the MPMDSet.

Thermodynamic Stability

Formation energy is used to compare the relative stability of compounds to their elemental constituents. The formation energy for the amorphous and crystalline phases is calculated with respect to the crystalline phases according to eqn. 5.2.

$$U_F(Li_xSi_{1-x-y}X_y) = U(Li_xSi_{1-x-y}X_y) - xU(\text{c-Li}) - (1-x-y)U(\text{c-Si}) - yU(\text{c-X}) \quad (5.2)$$

To evaluate the relative stability of the crystalline phases available in the Materials Project[143], a ternary phase diagram was generated for each chemical system. The phase diagram is constructed from the convex hull of composition and formation energy (U_F), such that phases coincident with the hull represent thermodynamically stable equilibrium phases[39] at low temperatures. Tie-lines, or line segments, connecting two stable points represent a two-phase equilibrium, such that materials with composition falling on the tie line will be predisposed to decomposing to form the bounding phases. Likewise, tie-triangles correspond to three-phase equilibria, where materials with formulas coincident with the triangles are composed of the phases at the vertices.

In addition to the construction of the crystalline phase diagram, we compose a hull for the amorphous phases. This convex hull is constructed in similar manner to the crystalline phase diagram, however all the crystalline energies are omitted except for BCC Li. In the absence of long and medium-range order and insufficient kinetic energy to overcome barriers for structural reorganization, decomposition into stable crystalline phases will be slow and the amorphous hull may be used to predict the lithiation behavior of Si-X alloys. Employing anode alloys that do not react with Li tends to result in Li metal plating, which motivates the use of the BCC polymorph as a reference state for Li.

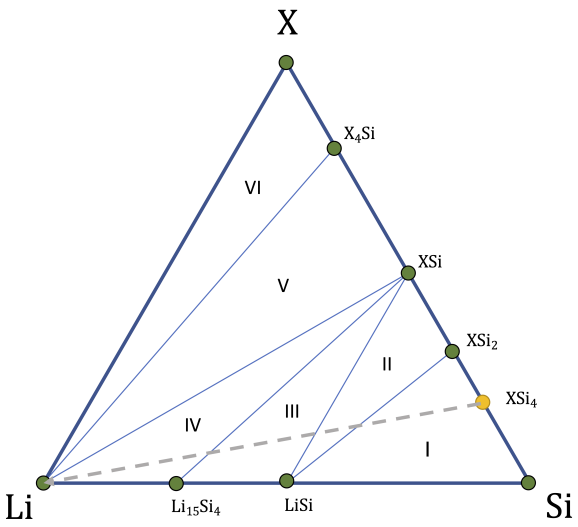

Figure 5.1: Example phase diagram for a Li-Si-X ternary system with all 3-phase equilibrium regions labeled. Stable phases are noted by green circles. Lithiation pathway of XSi_4 (marked in yellow) is drawn with a dashed grey line.

An example phase diagram is shown in Fig. 5.1 for a Li-Si-X system. Interpreting the lithiation pathway from the ternary phase diagrams follows a line segment connecting the composition with the pure Li point with considerations to the phase equilibria. A sample lithiation pathway is provided for a-XSi_4 (indicated by the yellow circle), which passes through the tie-triangles I, II, III, and IV, each corresponding to unique lithiation multi-phase stages for the material. In stage I, Li alloys with Si and extrudes XSi_2, quantities determined by applying the lever rule at the point of intersection with the XSi_2-LiSi tie line. Continued lithiation in stage II results in the displacement of XSi, a more X rich alloy, from XSi_2 and formation of more LiSi. In stage III, Li alloying converts LiSi into $Li_{15}Si_4$ with no change to XSi. Lithiation is bounded by stage IV since all present phases are in equilibrium with Li. Therefore, Li alloying is less favorable than Li plating at the electrode. Similar to stage IV, alloy formulations coincident with the XSi-X_4Si-Li (V) and X_4Si-X-Li (VI) phase equilibria are not expected to lithiate.

Extending from the convex hulls and phase diagram, the equilibrium lithiation potentials for crystalline and amorphous materials are predicted.[161, 41] As a summary, the lithium chemical potentials are determined for each three-phase equilibria in the crystalline phase diagram and amorphous convex hull. The Li chemical potentials are then related to the potential, E, by equation 5.3.

$$\mu_{Li} - \mu_{Li}^{0} = neE \tag{5.3}$$

where μ_{Li} is the chemical potential of Li within the lithiated phase, μ_{Li}^{0} is the reference chemical potential of BCC Li metal, e is the elementary charge of an electron, and n is the

moles of Li inserted per mole of the host.

The estimated full stack energy (FSE) density of an 18650 cell is calculated as a more useful metric to compare an alloy electrode with graphite, with a baseline of $726\,\mathrm{W\,h\,L^{-1}}$, as proposed by Obrovac et al.[20] The FSE density calculation is inversely related to the average voltage and directly related to the volumetric capacity, such that lower average voltage and higher volumetric capacity yields a higher FSE.

5.3 Results and Discussion

Activity of Elements

In general, the Li-activity of the pure elements in their amorphous phases tracks with that of the literature reports derived from calculations of the crystalline phases found on the ICSD and the Materials Project, as shown in fig. 5.2. Deviations include C, Cu, Mg, Ca, Sr, and Ru. While the intercalation of Li into graphite is well studied, amorphous carbon is not as well understood. Dahn et al. estimate a maximum lithiation capacity corresponding to a-$Li_{0.5}C$[162] which is enabled by lithiation of short-range graphitic environments. However, in our calculations, we find no capacity for a-C, which is attributed to the structural dissimilarity between our amorphous carbon structure and literature-reported a-C. Contrary to the disordered amalgamation of graphitic domains, our sampled a-C structures - formed through the melt-quench workflows - are comprised of layered amorphous graphene-like sheets which break down into carbon chains upon lithiation. Indeed, it is well-known that amorphous carbon capacity varies widely, depending on the degree and type of disorder.[163, 164, 165] It is generally accepted that Cu is inert; in fact, its electrochemical stability with respect to Li and high electronic conductivity have made it the most common anode current collectors.[3] However, within the Materials Project, a theoretical phase of tetragonal intermetallic $LiCu_3$ (mp-862658) is found to be stable at low temperatures. In addition, we find that the formation of amorphous intermetallic Cu-Li alloys to be stable relative to a-Cu and c-Li. Published Cu-Li phase diagrams observe solubility of Li in Cu at 23 °C, up to $Li_{13}Cu_{87}$, and depicts the existence of a Cu_2Li_3 phase between $\sim 500\,\mathrm{K}$-$840\,\mathrm{K}$, although Cu_2Li_3 is predicted from temperature dependent EMF measurements, but was not directly observed in DTA or XRD studies and has, to date, no reported structure in the ICSD.[166] In support of this, Li interdiffusion with Cu is observed in several studies, however, only a few nanograms were found to diffuse over 28 days at room temperature. [167] This suggests that alloying reactions between Li and Cu are severely kinetically hindered. From Fig. A.8, A.13, and A.30 we find no form stable amorphous Li-X phases forming with the Alkaline Earth metals (Mg, Ca, and Sr). Similarly, no stable crystalline Li-Sr phases are found. In contrast, multiple stable crystalline Li-Mg phases exist and one stable crystalline Li-Ca phase exists, although its(Li_2Ca) formation energy is only $12\,\mathrm{eV\,atom^{-1}}$. Li-Mg has been demonstrated to alloy with Li in experiments, however large capacity fade and low rate capability are observed, primarily attributed to the formation of high impedance surface films. [20] The Li_2Ca phase

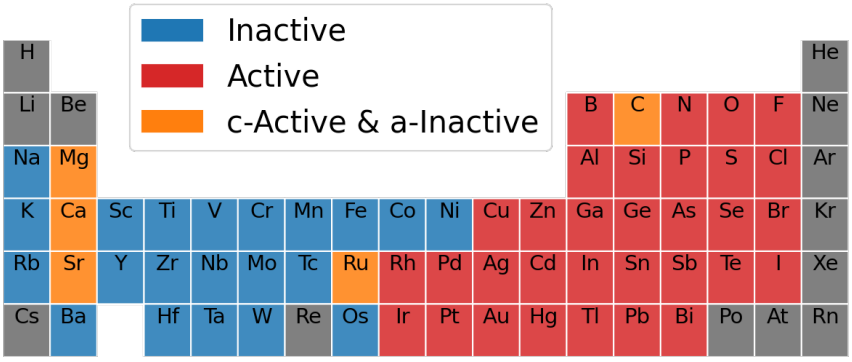

Figure 5.2: Periodic table with the predicted active (blue) and inactive elements (red). Elements in orange form thermodynamically stable crystalline binary Li-X phases, but the amorphous phases are not predicted to lithiate. The elements in grey were not included in this study.

is reported in studies, however, the plating of Li metal is observed due to the low lithiation potentials of Ca.[168] While Obrovac et al. classify Ru as an active element, it is believed that the storage of Li does not occur through an alloying or intercalation mechanism. [169] Our calculations support this fact, finding no lithiation for amorphous or crystalline Ru.

A summary of electrochemical characteristics of the active elements are tabulated in table 5.1. Most elements exhibit volumetric capacities 2-3x greater than graphite ($850\,\mathrm{AhL}^{-1}$)[2] and consequently, most alloying strategies are expected to improve on the energy density of an 18650 full cell, as compared to graphite. Notable exceptions include the Pnictogens (P, As, Sb), Chalcogens (O, S, Se, Te), and Halogens(F, Cl, Br, I) which exhibit lithiation potentials in excess of 1.0 V vs $\mathrm{Li/Li^+}$ due to the formation of highly stable ionic compounds. In full cells, these elements would not yield a high potential difference and therefore would exhibit low energy density, evidenced by the negative full stack energy (FSE) improvement in table 5.1.

Gaseous elements, such as H_2, N_2, O_2, and F_2, are omitted in table 5.1, due to the lack of a well-defined solid-state reference and the difficulty in reporting derived quantities. In addition, materials prone to gas formation would require additional considerations to alleviate internal pressure and cell swelling. These chemistries, while impractical for anode materials, have been successfully used as cathode materials in systems such as lithium-sulfur or lithium-air batteries. [170]

Binary and Ternary Si alloy formation

When alloying Si with another component, the ability of the two elements to mix and form stable binary alloys plays a significant role in the synthesis and performance of a material. When alloying with elements that form stable Si-X phases, synthesis of a phase-

Table 5.1: Electrochemical Characteristics for all amorphous active elements

	Max Volume Expansion (%)	Average Voltage (E)	Specific Capacity ($mAhg^{-1}$)	Volumetric Capacity (AhL^{-1})	FSE Improvement (%)
B	210	0.24	2480	1900	37
Al	300	0.089	2980	1880	43
P	250	0.56	3480	2110	27
S	50	1.7	2100	1770	-18
Cu	59	0.12	212	1120	28
Zn	100	0.27	410	1390	29
Ga	150	0.25	770	1710	34
Ge	310	0.25	1480	1940	37
As	180	0.69	1250	1960	21
Se	39	1.7	680	1450	-21
Br	-6	3.0	337	759	-73
Rh	310	0.13	781	2130	44
Pd	420	0.26	1010	2110	39
Ag	280	0.16	745	1850	40
Cd	220	0.12	715	1710	39
In	170	0.18	700	1680	36
Sn	260	0.25	1020	1870	36
Sb	190	0.54	880	1790	24
I	-15	2.4	212	569	-57
Te	54	1.4	421	1190	-14
Ir	200	0.26	279	1920	37
Pt	390	0.39	553	2150	34
Au	250	0.46	408	1940	29
Tl	200	0.12	525	1770	40
Pb	200	0.19	517	1740	37
Bi	180	0.43	516	1700	28

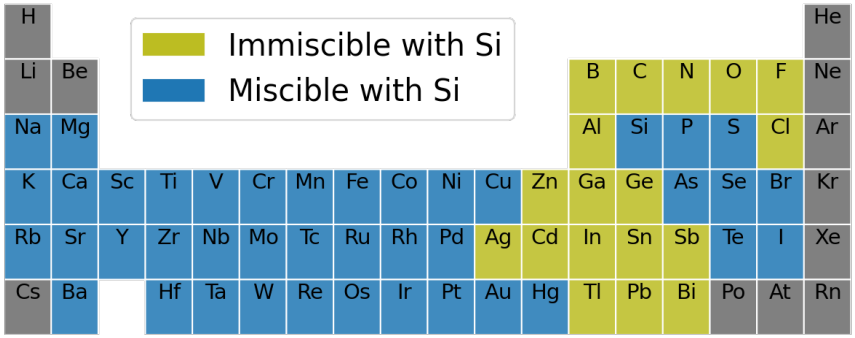

Figure 5.3: Periodic table indicating the tendency for elements to form stable alloys or phases with Si. Elements with repulsive interactions with Si are shaded in blue, while those forming bonds with Si are filled green.

pure amorphous material may be relatively easy. The elements that do not form stable Si-X phases are immiscible and will tend to decompose into a composite of two elemental phases. Multiple thermodynamic and kinetic factors govern the formation of separated phases and domain size distribution. High interfacial energy will bias towards phase segregation and promote the formation of distinct Si and X regions while contributions to the free energy from the mixing entropy will stabilize mixtures. Conversely, low solid state diffusivities may inhibit the migration of alloy components, preventing structural transformation. Hence, due to these competing factors, careful modulation of synthesis and processing conditions related to cooling rate is necessary to control phase segregation. Non-equilibrium methods such as splat quenching, sputtering, and mechanical milling may form metastable Si alloys with near homogeneous elemental distributions. An example of this is the tuning of segregation in Si-Ge alloys through annealing temperature and sputtering time presented by Kim et al[171].

Alloys of immiscible components with more uniform element dispersions will exhibit an increased formation energy relative to their composite counterparts. Using the computed formation energy as a strong indicator of lithiation potential of the host alloy or more stable lithiated intermediates results, we surmise that the increased formation energy of homogeneous alloys will translate to an increased lithiation potential, in particular at early lithiation stages.

While phase segregation is not ideal, electrodes constructed from these materials have nevertheless shown improved performance. The formation of nanocomposites of two active elements via phase segregation during synthesis has shown improved cycling, as compared to Si, and the homogenization of these materials may even be seen after cycling.[136]

The tendency for elements to form stable amorphous binary alloys, defined by the presence of at least one composition on the Si-X convex hull, with Si is shown in Fig. 5.3. Cross-referencing with the Li alloying activity (Fig. 5.2), we find that all inactive alloys

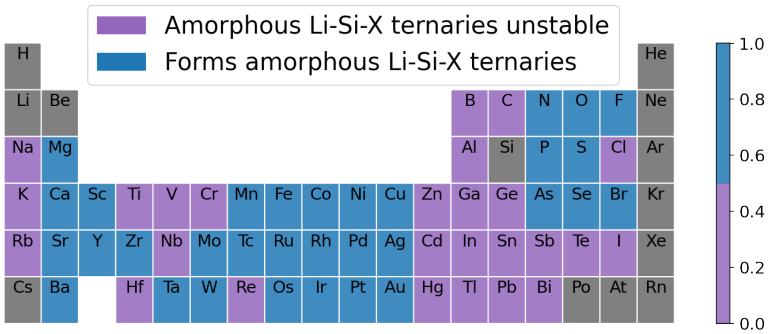

Figure 5.4: Ternary phase formation with Li and Si. Elements which form stable ternary phases are colored in blue. Elements forming ternary compounds which all lie above the convex hull are shaded purple. We note that in some systems with stable ternaries, the ternaries are stabilized by only $<5\,\mathrm{meV\,atom^{-1}}$. Caution should be exercised in interpreting this binary categorization, as numerical accuracy or entropy may destabilize the ternaries with respect to the binary alloys or pure elements.

are found to form stable crystalline Si-X phases. We find parity between the amorphous and crystalline when considering the Si-X phases, which are stable relative to their pure amorphous termini, except for C, Na, and K, for which no amorphous Si-X phases lie on the amorphous hull. In the active elements, we find B, C, and Au to form stable amorphous binary phases, but not crystalline.

Formation of a binary, however, does not preclude the phase decomposition during cycling. For chemical systems without stable ternaries, Si rich and Si poor regions may form during the alloy process with Li. Coarsening of these inhomogeneous regions is dependent on the diffusion kinetics, where fast diffusion will result in more pronounced phase separation. While Li diffusivity may be system dependent, in Si, diffusion is enhanced with Li alloying, reducing the barrier to growth of inhomogeneities[41, 80]. While nanocomposite Si-M may be able to absorb stresses caused by inhomogeneous lithiation, larger regions may strain the material more, leading to stress induced cracking. In this regard, alloys that form many thermodynamically favorable ternary phases may be more stable, since they may undergo less drastic structural reorganization during lithiation and delithiation. Inclusion of all elements into a ternary would limit the separation of X and Si atoms to a few coordination shells.

Elements with unfavorable Si-X bonding which do not form binary phases do not form stable ternaries, here defined as a composition that forms a vertex on the amorphous hull. The energy above hull for these decreases with increased Li(example seen in SI fig S43 and S42, suggesting that Li buffers the repulsive interactions through the formation of Li-X and Li-Si bonds. The energy above hull is low enough that the entropic contributions to free energy may be sufficient to stabilize these ternaries near room temperature. At

room temperature (23 °C) the entropy of mixing, estimated using Boltzmann's equation, contributes up to 28 meV atom^{-1}, therefore phases up to 28 meV atom^{-1} above the hull may be stable. Conversely, the favorability of Si-X bonds does not guarantee presence of a stable ternary phase as, for example, twelve of the elements which are miscible with Si do not form ternaries.

We find that a few elements exhibit a rich chemistry of ternary amorphous phases, including Ca, Cu, Ru, Rh, Pd, Ir, and Sr. In these systems, most calculated compositions do not deviate more than 10 meV atom^{-1} from the amorphous hull. We expect that these systems will exhibit featureless voltage curves, since there is no preferential phase/composition. This is indeed the case for $CaSi_2$, which is reported to have a featureless, sloping voltage curve.[172] The calculated discrete voltages, seen in fig. A.71, for $Ca_{0.25}Si_{0.75}$ and $Ca_{0.5}Si_{0.5}$ show several lithiation voltage steps, each with relatively small capacities and we expect that - if many more amorphous compositions were sampled - a smooth, sloping lithiation profile would emerge.

Inactive Alloys

Since all inactive elements are miscible with Si, the main differentiating factor in the evolution during lithiation is the ability to form ternary alloys. Two representative amorphous hulls for these two groups of Si/inactive alloy systems are shown in Fig. 5.5 for the Cr-Si and Fe-Si systems, respectively.

Figure 5.5a is an example of an alloy component which forms binaries with Si, but does not form favorable amorphous ternary Li-Si-X phases. The two labeled composition ranges on the Si-Nb line correspond to:

- I-a) At low concentrations of alloyed inactive elements, the early lithiation potential will match those of Si, forming two phases - a Li-Si binary phase and Si-X phase. Once all Si has been exhausted, Li-Si phases will lithiate as usual, while the Si-X phase remains unchanged. When the composition intersects the $NbSi_2$-$Li_{26}Si_{15}$, lithiation further displaces more X rich Si-X phases. Lithiation depletes the Si in Si-X, until Nb_5Si_3 is reached, where no further lithiation is expected due to the two phase equilibrium with BCC Li.

- II-a) No lithiation is expected for alloys with composition falling within this range. Because there are no nodes on the Li-Nb phase equilibrium line, no Nb is not expected to lithiate. Additionally, these phase equilibrium triangles predict a equilibria with Li, no capacity is expected since Li plating is more favorable than Li alloying.

the boundary between I-a and II-a varies among the inactive elements as well as for the amorphous and crystalline materials. Generally, alloying with X $z \geq 50$ will yield little to no capacity and should be avoided. Based on our findings, we do not recommend alloying with more than 33-40 atom % of these inactive elements, since capacity is significantly penalized above this composition.

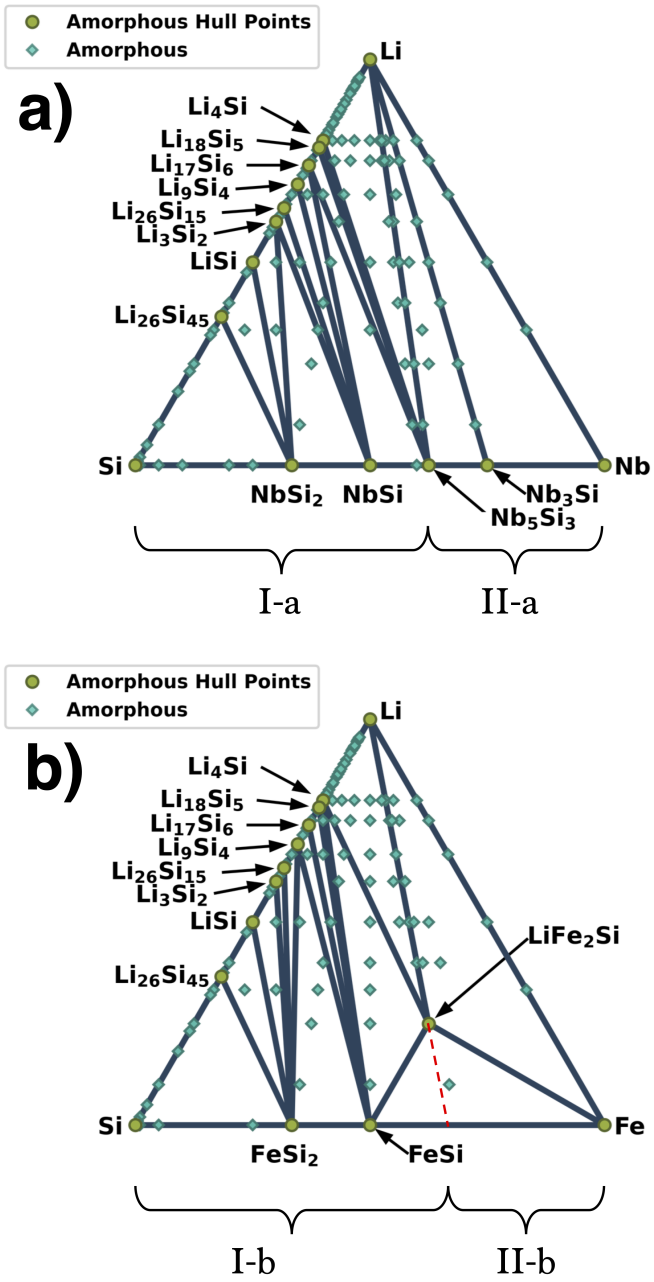

Figure 5.5: Sample amorphous hulls for Si/inactive alloys depicting chemical systems with a) no stable ternaries and b) stable ternaries formed. Stable and unstable phases are represented by green circles and teal diamonds, respectively. Red dashed line in b) is a projection of the Li-$LiFe_2Si$ tie-line and its intersection with the Si-Fe equilibrium is the cutoff between I-b and II-b

Figure 5.5b depicts an alloying element for which the of binary and ternary amorphous phases are predicted to form. The formation of ternaries may be able to extend the range of alloys with lithiation capacity. In these systems, the lithiation is bounded by the formation of the ternary Li-Si-X phase rather than a Si-X binary. While inactive components are not expected to contribute capacity and bind Si active material, the formation of a ternary phase results in additional Li storage when compared to those which do not form a ternary. In the case of Fe, the formation of $LiFe_2Si$, additional capacity is observed in Fe rich $Si_{1-z}Fe_z$ alloys (II-b in fig. 5.5), as some metal is reduced and extruded. Comparing Si-Fe to Si-Nb, an alloy with composition Nb_2Si would not alloy with Li while Fe_2Si stores one Li per host formula unit.

In both phase diagrams in 5.5, it is clear that the alloyed inactive metals do not get fully reduced and displaced, favoring the formation of intermediate binaries or ternaries, consuming Si active material. In the case of Nb, Nb_5Si_3 is formed as an inert matrix and continued cycling proceeds alloying (and dealloying) of the Li-Si binaries. It is commonly cited that alloys derived from inactive elements do not actively participate in compound formation with Li[20, 21] and follow the reaction shown in Eqns 5.4 and 5.5.
First lithiation:

$$X_zSi_{1-z} \xrightarrow[e^-]{Li^+} (1-z)Li_xSi + zX \tag{5.4}$$

Subsequent cycling:

$$Li_xSi + X \xleftrightarrow[e^-]{Li^+} Si + X \tag{5.5}$$

For an alloy to follow this chemical reaction, its corresponding phase diagram must show an equilibrium between X, Li, and an Li-Si phase. Thus, the Si-X binary phases must have a higher formation energy (less stable) than the Li-Si phases. In our calculations, the methodology for sampling amorphous configurations provides an upper bound on the formation energy, where more sampling statistics can only decrease formation energy. Therefore, in most of the inactive alloy systems, the Li-Si alloys will always be more stable than the Si-X alloys. Amorphous Mn_zSi_{1-z} is the only system found, among the amorphous and crystalline Si-X, to completely extrude Mn metal and is shown in fig. 5.6. In this system, lithiation is bounded by the Li-M-Li_4Si equilibrium with a final lithiation state coincident with the M-Li_4Si tie-line. More accurate chemical reactions to describe most Si/inactive alloy materials are shown in eqn. 5.6 and 5.7:
First lithiation:

$$X_xSi_y \xrightarrow[e^-]{Li^+} \delta Li_xSi + X_xSi_{(y-\delta)} \tag{5.6}$$

Subsequent cycling:

$$Li_xSi + X_xSi_{(y-\delta)} \xleftrightarrow[e^-]{Li^+} Si + X_xSi_{(y-\delta)} \tag{5.7}$$

where the inactive element deactivates Si active material through the formation of X rich binary alloys. Upon delithiation, Si may not quickly re-alloy with the inactive Si-X phase extruded, due to the sluggish kinetics for Si diffusion. In support of this, Yang et al. reported

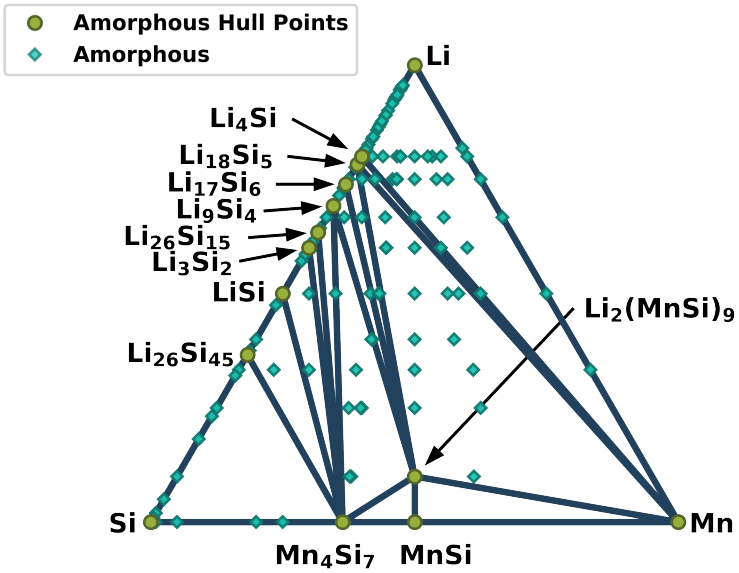

Figure 5.6: Li-Mn-Si phase diagram showing the only system tending to extrude pure metal. Any $Mn_zSi_{(1-z)}$ material will intersect the Mn-Li_4Si phase equilibrium and displace Mn metal.

electrochemically inactive $NiSi_x$ nanowires coated with Si which cycled reversibly without affecting the $NiSi_x$ core.[173, 174]

Therefore, decreased average voltage seen when alloying inactive elements may be attributed to two contributions. i) Decreased volumetric expansion as proposed by Obrovac et al.[25] This is similar to the mechanism proposed by Obrovac et al.[117], however the volumetric expansion is buffered by irreversible X_zSi_{1-z} phases rather than X. ii) Electrodes constructed from materials with higher X concentration than $\sim 33\%$ will bypass early Li_nSi ($0 \leq n \leq 1.5$) lithiation stages and start at a lower potential.

Active Alloys

The majority of Si/active systems fall into two groups: 1) elements which are immiscible with Si and do not form stable ternary phases or 2) elements that are miscible with Si and do form stable ternary phases. Only a handful of ternary alloy systems fall outside of these two groups. Ag is the only active element that is immiscible with Si and form stable amorphous ternaries. Te, I, and Hg are all miscible with Si, but do not form stable amorphous ternaries.

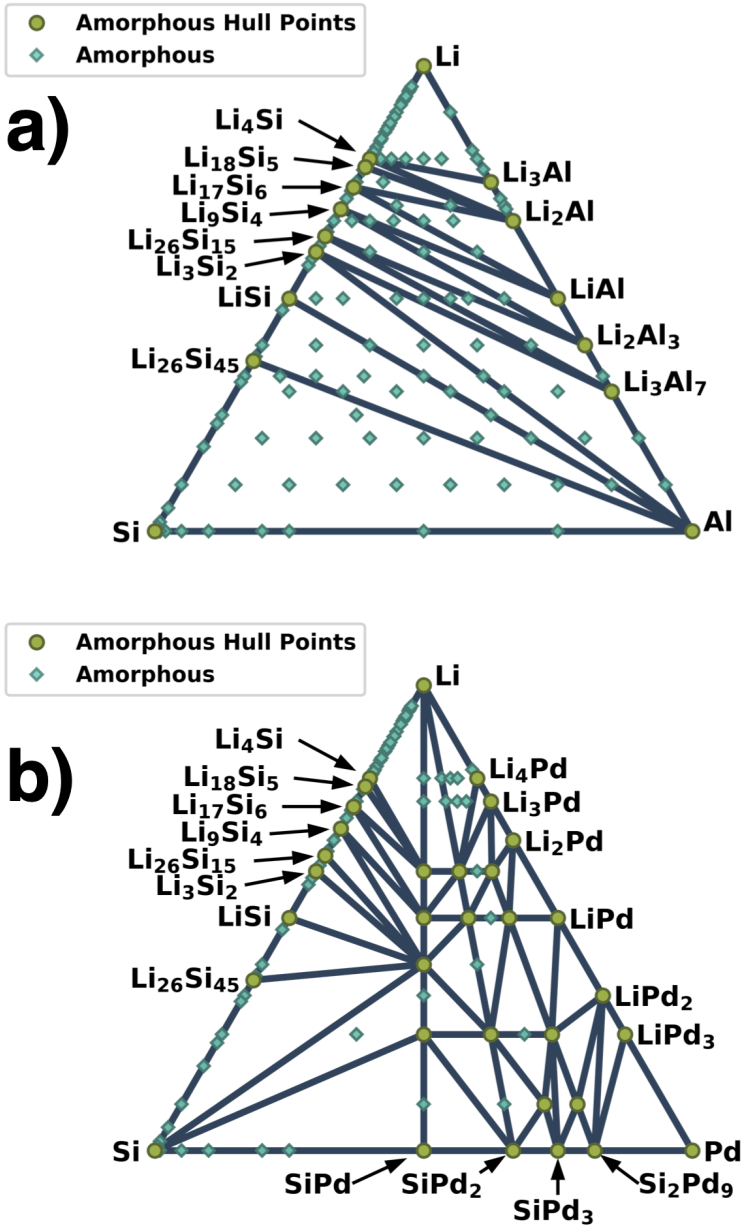

Figure 5.7: Sample amorphous hulls for Si/active alloys depicting chemical systems which are a) immiscible and do not form stable ternaries b) miscible and form stable ternaries. Stable and unstable phases are represented by green circles and teal diamonds, respectively.

Immiscible alloy components will have a high driving force for phase segregation, especially those with no ternaries. Thus, those in group 1) will tend to form a nanocomposite during synthesis, unless kinetics are significantly hindered through high quenching rate or ball milling. Alloys synthesized through this method may be highly metastable, even relative to the amorphous hull. These alloys will exhibit an increased lithiation potential during the first lithiation, along with formation of two distinct lithiation phases (one Li-X and Li-Si). In subsequent cycling, the two lithiated phases will cycle as expected for each of Li-X and Li-Si. In some of these alloys, homogeneous lithiated phases lie closer to the hull, where the entropy may be sufficient to stabilize the alloy near room temperature and phase segregation may not be observed. The tie-triangles composing the lithiation pathway followed for these materials always share an edge with Li-Si or Li-X and therefore the lithiation potential is a composite of the Si and X lithiation potentials. Because alloying with these active elements does not form irreversible phases, any Si/active alloy composition may be suitable for active materials. For highest specific capacity, a higher Si content is desirable, while for volumetric capacity it is element dependent, since some elements have comparable volumetric capacities to Si.

Materials within group (ii) should theoretically form materials with higher mechanical stability during cycling. The absence of two distinct phases during lithiation may give rise to more uniform stress distributions due to uniform lithium distribution. Many precious or rare elements, such as Pd, Rh, Pt, and Ir, which may not be practical for use in Li-ion batteries fall under this group. Early lithiation potentials in Pt and Pd based alloys are rather high ($> 0.8\,\mathrm{V}$ vs $\mathrm{Li/Li^+}$), while Rh and Ir exhibit more useful potentials ($\sim 0.55\,\mathrm{V}$ vs $\mathrm{Li/Li^+}$). Also in this group are the aforementioned elements which form highly stable compounds with Li, such O, S, Te, and Sb. While these elements do not have direct utility as anodes, they may be used in a manner similar to the inactive alloys. During the first lithiation cycle of binary Si alloys containing these elements, very stable ternary and binary phases will be formed at high potentials ($> 1.0\,\mathrm{V}$ vs $\mathrm{Li/Li^+}$). These phases will be functionally irreversible phases and may not actively participate in any reactions and would serve as a buffering matrix to accommodate stress and decrease volumetric expansion. In the case of SiO_x, cycling is found to form a Li-ion conductive Li_4SiO_4 phase during lithiation which is not associated with a large volume expansion[175, 176, 41]. Fast charge transfer at the SiO/electrolyte interface is also found, signaling that alloying with these high voltage elements may improve the rate capability of electrodes. Although these phases may be inert within the range of cycling, it is important to remember that they deplete Li inventory. Given that current cathodes are the source of Li in newly manufactured batteries, this decreases the effective reversible cathode capacity, requiring considerations such as a higher ratio of cathode to anode capacity or prelithiation of the anode.[177, 152] Zhao et al. reported on a Li_xSi/Li_2O composite anode synthesized through metallurgical prelithiation of SiO_x with $\sim 99.87\,\%$ coulombic efficiency over 400 cycles.[62]

5.4 Conclusion

In summary, we conduct an ab-initio investigation of the thermodynamic impact of alloying Si with a second component. We find that inactive components do not get fully displaced to form pure metals as literature reaction mechanisms propose. Instead, stable Si-X phases are formed which do not lithiate, binding otherwise active Si in an inactive phase which is detrimental to capacity. This results in higher capacity loss than would be expected for a non-participating additive. Si/inactive alloys, however, are capable of bypassing higher voltage Si lithiation stages, thereby decreasing the average potential and increasing energy density. A subset of Si/active alloys are found to favor phase separation to form nanocomposite materials which match the lithiation potentials of the individual alloy components. The remaining Si/active elements will displace stable ionic compounds when reacting with Li, which are functionally irreversible due to high (de)lithiation potential($\geq$ 1.0 V vs Li/Li^+). These may be function in a similar manner to inactive phases in Si/inactive alloys, although they deplete Li inventory rather than Si active material.

Chapter 6

Conclusion and Further Work

6.1 Conclusion

In this dissertation, an evaluation of the lithiation thermodynamics and electrode characteristics was presented for amorphous binary alloys between Si and the group 1-17 elements. We find the Li-alloying capability of the group 1-17 elements to match well with the previous reports, except for a handful of elements (namely Cu, Mg, Ca, Sr, and Ru). Based on reactivity to Li, the added elements are partitioned into two groups of active and inactive elements.

Active elements are not miscible with Si(do not form stable materials with Si), that is, the resulting Si-X alloy are predicted decompose to form distinct Si and X phases either during synthesis or during cycling. Therefore, lithiation potentials are expected to be a composite of the characteristic voltage plateaus for each individual element. This gives active alloys the ability to tailor the lithiation voltage within a wide range (0 V-3.0 V) by modulating alloyed element and quantity. We posit that melting temperature is the main factor in ion mobility, finding Li-diffusivity of these elements to increase as the material is charged and Li is inserted. In support of this, Li_xSi, Li_xSiSn and Li_xSiO_2 decrease in melting point with alloyed Li, while the Li-diffusivity increases. In contrast, Sn has a low intrinsic melting temperature, leading to high Li-diffusivity, however Li alloying elevates melting temperature and slows diffusion. Phase segregation is not necessarily detrimental to electrode performance, and improved electrode performance is predicted for homogeneous and heterogeneous mixtures. Additionally, when alloying Si-Sn with Li, the thermodynamic driving force for phase segregation is decreased. At higher Li content, and accommodating for entropy and decreased Si-diffusivity at high Li content, decomposition may not be observed at room temperature.

As inactive added components do not alloy with Li, derivative Si-alloys exhibit decreased Li storage capacity, however may show an increased energy density when utilized in a full cell. Inactive components decrease the average lithiation potential by bypassing the initial lithiation of tetrahedrally coordinated Si in favor of Si chains and agglomerates. Addition-

ally, a decreased volumetric expansion results in further decreased lithiation potential when compared to Si. While this effect is beneficial at lower concentrations, the capacity rapidly decreases as inactive components are alloyed, with a maximum concentration of 33 %.

6.2 Further Work

This dissertation primarily covers alloying-type electrodes based on Si alloy materials, focusing on the structural evolution and thermodynamics during lithiation. There remain many unanswered questions that would benefit from continued research.

The Li-diffusivity is of great importance to the performance of alloy electrodes in full cells. High Li-diffusivities are expected to yield electrodes with higher rate performance and lower overpotentials during charge and discharge, resulting in higher reversible energy density. Our results show that alloying Si with other elements presents an avenue to modulate the Li-diffusivity by tailoring the bonding environments encountered by Li and Si. While we were able to ascertain the Li self-diffusion coefficients for specific Li-Si and Li-Si-Sn alloys, the computational expense of AIMD simulations prohibited a high-throughput evaluation of Li-diffusivity. However, machine learned, Deep Neural Network (DNN) interatomic potentials, such as DeePMD[178, 179], have advanced tremendously in recent years, improving chemical accuracy and decreasing the necessary training data. Machine Learned interatomic potentials bridge the gap between the accuracy of first-principles molecular dynamics and the scalability and speed of classical molecular dynamics. Additionally, they eliminate the empirical nature of classical force fields. With the large quantity of AIMD simulations generated when simulating amorphous structures, Deep Neural Network potentials may be trained for many chemical systems. This would enable the rapid exploration of Li-diffusivity in the vast alloy chemical space. Further sampling of quasi-amorphous structures would additionally be accelerated, although it remains to be seen if these DNN potentials are capable of accurately extrapolating to higher chemical spaces which may not be represented in the training set. For example, could a model trained with structures containing 1, 2, or 3 elements accurately describe quaternary compounds?

While alloying of Si with one component is an effective strategy of tailoring electrode performance, the alloying of multiple components provide additional routes to alter the electrochemical behavior of Si anodes. Schnabel et al.[154] reported on an amorphous $Al_{64}Si_{25}Mn_{11}$ anode exhibiting $> 900\,\mathrm{mAhg^{-1}}$. Reduced parasitic electrolyte reduction was found for this combination of active and inactive components compared to pure Si or Al. The use of multiple components, especially with multiple inactive components, is a growing area of research.[20, 21] However, experimental exploration will be slow due to the combinatorial explosion when considering three or more elements. Therefore, a computational approach will enable rapid screening of alloy compositions in parallel, especially if the DNN interatomic potentials mentioned above can be leveraged. Combinatorial or robotic synthesis platforms are increasingly being used and may accelerate the discovery of alloy electrodes. Leveraging both automated synthesis and computational modeling to guide synthesis efforts

and validation may significantly reduce the cost and effort required to explore the large alloy space.

Similar to Si, Sn is a promising electrode material due to its high volumetric capacity and Li-diffusivity. Aside from metal silicides, Sn-based alloys are perhaps the second most studied alloy-type electrode.[180, 27, 136] Composite tin-based amorphous electrodes, composed of Sn, Co, and C, have previously been commercialized by Sony in 2005 under the trademark "Nexelion," exhibiting reversible capacities 28% higher than graphite.[180] Given the higher intrinsic Li-diffusivity and electronic conductivity in Sn, it is clear that Sn has suitable electrochemical properties, although, like Si, Sn suffers from pulverization stemming from volumetric expansion. Nanostructuring has increased reversible capacity and extended cycle life, but repeated cycling leads to particle agglomeration.[181] The use of nanostructured composite materials and intermetallic alloys is a promising alternative to nanosized materials. The approach applied in this thesis to Si can be used to evaluate the viability of Sn-based intermetallics. Slight modification to the methodology may be necessary due to Sn's tendency to crystallize during cycling, although intermetallics with more elements may resist crystallization and phase segregation.[181]

Bibliography

[1] Kristin Persson et al. "Lithium diffusion in graphitic carbon". In: *Journal of Physical Chemistry Letters* 1.8 (2010), pp. 1176–1180. ISSN: 19487185. DOI: 10.1021/jz100188d.

[2] Runwei Mo et al. "Tin-graphene tubes as anodes for lithium-ion batteries with high volumetric and gravimetric energy densities". In: *Nature Communications* 11.1 (2020), pp. 1–11. ISSN: 20411723. DOI: 10.1038/s41467-020-14859-z. URL: http://dx.doi.org/10.1038/s41467-020-14859-z.

[3] Jakob Asenbauer et al. "The success story of graphite as a lithium-ion anode material – fundamentals, remaining challenges, and recent developments including silicon (oxide) composites". In: *Sustainable Energy & Fuels* 4.11 (2020), pp. 5387–5416. ISSN: 2398-4902. DOI: 10.1039/D0SE00175A. URL: http://xlink.rsc.org/?DOI=D0SE00175A.

[4] Kristin Persson et al. "Thermodynamic and kinetic properties of the Li-graphite system from first-principles calculations". In: *Physical Review B* 82.12 (2010), p. 125416. ISSN: 1098-0121. DOI: 10.1103/PhysRevB.82.125416. URL: https://link.aps.org/doi/10.1103/PhysRevB.82.125416.

[5] M Stanley Whittingham. "Ultimate Limits to Intercalation Reactions for Lithium Batteries". In: *Chemical Reviews* 114.23 (Dec. 2014), pp. 11414–11443. ISSN: 0009-2665. DOI: 10.1021/cr5003003. URL: https://pubs.acs.org/doi/10.1021/cr5003003.

[6] Andy Brunning. *Periodic Table of Annual Production of Elements*. Nov. 2021. URL: https://www.compoundchem.com/2019advent/day19/.

[7] M. N. Obrovac and Leif Christensen. "Structural Changes in Silicon Anodes during Lithium Insertion/Extraction". In: *Electrochemical and Solid-State Letters* 7.5 (2004), A93–A96. ISSN: 10990062. DOI: 10.1149/1.1652421. URL: http://esl.ecsdl.org/cgi/doi/10.1149/1.1652421.

[8] Hunjoon Jung et al. "Amorphous silicon anode for lithium-ion rechargeable batteries". In: *Journal of Power Sources* 115.2 (2003), pp. 346–351. ISSN: 03787753. DOI: 10.1016/S0378-7753(02)00707-3.

[9] Candace Chan et al. "High-performance lithium battery anodes using silicon nanowires". In: *Nature Nanotechnology* 3.1 (2007), pp. 31–35. ISSN: 1748-3387. DOI: doi:10.1038/nnano.2007.411. URL: citeulike-article-id:7465929%5Cnhttp://dx.doi.org/10.1038/nnano.2007.411.

[10] Nian Liu et al. "A yolk-shell design for stabilized and scalable Li-ion battery alloy anodes". In: *Nano Letters* 12.6 (2012), pp. 3315–3321. ISSN: 15306984. DOI: 10.1021/nl3014814.

[11] Hui Wu et al. "Stable cycling of double-walled silicon nanotube battery anodes through solid–electrolyte interphase control". In: *Nature Nanotechnology* 7.5 (2012), pp. 310–315. ISSN: 1748-3387. DOI: 10.1038/nnano.2012.35. URL: http://www.nature.com/doifinder/10.1038/nnano.2012.35.

[12] Liangdong Lin et al. "Mesoporous Amorphous Silicon: A Simple Synthesis of a High-Rate and Long-Life Anode Material for Lithium-Ion Batteries". In: *Angewandte Chemie International Edition* 55.45 (Nov. 2016), pp. 14063–14066. ISSN: 14337851. DOI: 10.1002/anie.201608146. URL: http://doi.wiley.com/10.1002/anie.201608146.

[13] Yunya Zhang et al. "Silicon Anodes with Improved Calendar Life Enabled By Multivalent Additives". In: *Advanced Energy Materials* (2021). ISSN: 16146840. DOI: 10.1002/aenm.202101820.

[14] Binghong Han et al. "Using Mixed Salt Electrolytes to Stabilize Silicon Anodes for Lithium-Ion Batteries via in Situ Formation of Li–M–Si Ternaries (M = Mg, Zn, Al, Ca)". In: *ACS Applied Materials & Interfaces* 11 (2019), pp. 29780–29790. ISSN: 1944-8244. DOI: 10.1021/acsami.9b07270.

[15] Ivana Hasa et al. "Electrochemical Reactivity and Passivation of Silicon Thin-Film Electrodes in Organic Carbonate Electrolytes". In: *ACS Applied Materials and Interfaces* 12.36 (2020), pp. 40879–40890. ISSN: 19448252. DOI: 10.1021/acsami.0c09384.

[16] S. F. Lux et al. "The mechanism of HF formation in LiPF6 based organic carbonate electrolytes". In: *Electrochemistry Communications* 14.1 (2012), pp. 47–50. ISSN: 13882481. DOI: 10.1016/j.elecom.2011.10.026.

[17] M. S. Ding et al. "Change of Conductivity with Salt Content, Solvent Composition, and Temperature for Electrolytes of LiPF[sub 6] in Ethylene Carbonate-Ethyl Methyl Carbonate". In: *Journal of The Electrochemical Society* 148.10 (2001), A1196. ISSN: 00134651. DOI: 10.1149/1.1403730.

[18] Michael S. Ding and T. Richard Jow. "Conductivity and Viscosity of PC-DEC and PC-EC Solutions of LiPF[sub 6]". In: *Journal of The Electrochemical Society* 150.5 (2003), A620. ISSN: 00134651. DOI: 10.1149/1.1566019.

[19] Ryan T. Pekarek et al. "Intrinsic chemical reactivity of solid-electrolyte interphase components in silicon-lithium alloy anode batteries probed by FTIR spectroscopy". In: *Journal of Materials Chemistry A* 8.16 (2020), pp. 7897–7906. ISSN: 20507496. DOI: 10.1039/c9ta13535a.

[20] M. N. Obrovac and V. L. Chevrier. "Alloy negative electrodes for Li-ion batteries". In: *Chemical Reviews* 114.23 (2014), pp. 11444–11502. ISSN: 15206890. DOI: 10.1021/cr500207g.

[21] Bo Ding et al. "A Review of Metal Silicides for Lithium-Ion Battery Anode Application". In: *Acta Metallurgica Sinica (English Letters)* 34.3 (Mar. 2021), pp. 291–308. ISSN: 1006-7191. DOI: 10.1007/s40195-020-01095-z. URL: https://doi.org/10.1007/s40195-020-01095-z%20https://link.springer.com/10.1007/s40195-020-01095-z.

[22] Tahar Azib et al. "Ni-Sn intermetallics as an efficient buffering matrix of Si anodes in Li-ion batteries". In: *Journal of Materials Chemistry A* 8.35 (2020), pp. 18132–18142. ISSN: 20507496. DOI: 10.1039/d0ta06047j.

[23] T. D. Hatchard, M. N. Obrovac, and J. R. Dahn. "A Comparison of the Reactions of the SiSn, SiAg, and SiZn Binary Systems with L3i". In: *Journal of The Electrochemical Society* 153.2 (2006), A282. ISSN: 00134651. DOI: 10.1149/1.2140607. URL: http://jes.ecsdl.org/cgi/doi/10.1149/1.2140607.

[24] M. D. Fleischauer, J. M. Topple, and J. R. Dahn. "Combinatorial investigations of Si-M (M = Cr + Ni, Fe, Mn) thin film negative electrode materials". In: *Electrochemical and Solid-State Letters* 8.2 (2005). ISSN: 10990062. DOI: 10.1149/1.1850395.

[25] M. N. Obrovac et al. "Alloy design for lithium-ion battery anodes". In: *Journal of the Electrochemical Society* 154.9 (2007), pp. 849–855. ISSN: 00134651. DOI: 10.1149/1.2752985.

[26] Hansu Kim et al. "The Insertion Mechanism of Lithium into Mg2Si Anode Material for Li-Ion Batteries". In: *Journal of The Electrochemical Society* 146.12 (1999), pp. 4401–4405. ISSN: 0013-4651. DOI: 10.1149/1.1392650.

[27] Cheol-Min Park et al. "Li-alloy based anode materials for Li secondary batteries". In: *Chemical Society Reviews* 39.8 (2010), p. 3115. ISSN: 0306-0012. DOI: 10.1039/b919877f. URL: http://xlink.rsc.org/?DOI=b919877f.

[28] Andreas Netz, Robert A. Huggins, and Werner Weppner. "The formation and properties of amorphous silicon as negative electrode reactant in lithium systems". In: *Journal of Power Sources* 119-121 (2003), pp. 95–100. ISSN: 03787753. DOI: 10.1016/S0378-7753(03)00132-0.

[29] Andreas Netz and Robert A. Huggins. "Amorphous silicon formed in situ as negative electrode reactant in lithium cells". In: *Solid State Ionics* 175.1-4 (2004), pp. 215–219. ISSN: 01672738. DOI: 10.1016/j.ssi.2003.11.048.

[30] Yong Ning Zhou et al. "Nanostructured NiSi thin films as a new anode material for lithium ion batteries". In: *Electrochemistry Communications* 13.6 (2011), pp. 546–549. ISSN: 13882481. DOI: 10.1016/j.elecom.2011.03.006.

[31] G. X. Wang et al. "Nanocrystalline NiSi alloy as an anode material for lithium-ion batteries". In: *Journal of Alloys and Compounds* 306.1-2 (2000), pp. 249–252. ISSN: 09258388. DOI: 10.1016/S0925-8388(00)00775-1.

[32] L Martinez et al. "PACKMOL: A Package for Building Initial Configurations for Molecular Dynamics Simulations". In: *Journal of computational chemistry* 30.10 (2009), pp. 2158–2159. ISSN: 1096-987X. DOI: 10.1002/jcc.21224.

[33] Shyue Ping Ong et al. "Python Materials Genomics (pymatgen): A robust, open-source python library for materials analysis". In: *Computational Materials Science* 68 (2013), pp. 314–319. ISSN: 09270256. DOI: 10.1016/j.commatsci.2012.10.028. URL: http://dx.doi.org/10.1016/j.commatsci.2012.10.028.

[34] Francis Birch. "Finite elastic strain of cubic crystals". In: *Physical Review* 71.11 (1947), pp. 809–824. ISSN: 0031899X. DOI: 10.1103/PhysRev.71.809.

[35] Mathieu Leocmach. *Pyboo: A Python package to compute bond orientational order parameters*. 2017. DOI: 10.5281/zenodo.1066568. URL: https://github.com/MathieuLeocmach/pyboo.

[36] Naveen Michaud-Agrawal et al. "Software News and Updates MDAnalysis: A Toolkit for the Analysis of Molecular Dynamics Simulations". In: *Journal of computational chemistry* 32 (2011), pp. 2319–2327. ISSN: 1096-987X. DOI: 10.1002/jcc.

[37] Muratahan Aykol et al. "Thermodynamic limit for synthesis of metastable inorganic materials". In: *Science Advances* 4.4 (2018), eaaq0148. ISSN: 23752548. DOI: 10.1126/sciadv.aaq0148.

[38] Muratahan Aykol and Kristin A. Persson. "Oxidation Protection with Amorphous Surface Oxides: Thermodynamic Insights from Ab Initio Simulations on Aluminum". In: *ACS Applied Materials and Interfaces* 10.3 (2018), pp. 3039–3045. ISSN: 19448252. DOI: 10.1021/acsami.7b14868.

[39] Shyue Ping Ong et al. "Li - Fe - P - O2 phase diagram from first principles calculations". In: *Chemistry of Materials* 20.5 (2008), pp. 1798–1807. ISSN: 08974756. DOI: 10.1021/cm702327g.

[40] Changho Kim, Oleg Borodin, and George Em Karniadakis. "Quantification of sampling uncertainty for molecular dynamics simulation: Time-dependent diffusion coefficient in simple fluids". In: *Journal of Computational Physics* 302 (2015), pp. 485–508. ISSN: 10902716. DOI: 10.1016/j.jcp.2015.09.021. URL: http://dx.doi.org/10.1016/j.jcp.2015.09.021.

[41] Eric Sivonxay, Muratahan Aykol, and Kristin A. Persson. "The lithiation process and Li diffusion in amorphous SiO2 and Si from first-principles". In: *Electrochimica Acta* 331.xxxx (2020), p. 135344. ISSN: 00134686. DOI: 10.1016/j.electacta.2019.135344. URL: https://doi.org/10.1016/j.electacta.2019.135344.

[42] Jiajun Chen. "Recent progress in advanced materials for lithium ion batteries". In: *Materials* 6.1 (2013), pp. 156–183. ISSN: 19961944. DOI: 10.3390/ma6010156.

[43] Naoki Nitta and Gleb Yushin. "High-capacity anode materials for lithium-ion batteries: Choice of elements and structures for active particles". In: *Particle and Particle Systems Characterization* 31.3 (2014), pp. 317–336. ISSN: 15214117. DOI: 10.1002/ppsc.201300231.

[44] Ji Y. Kwon, Ji Heon Ryu, and Seung M. Oh. "Performance of electrochemically generated Li21Si5 phase for lithium-ion batteries". In: *Electrochimica Acta* 55.27 (2010), pp. 8051–8055. ISSN: 00134686. DOI: 10.1016/j.electacta.2010.01.054.

[45] Georgios A Tritsaris et al. "Di ff usion of Lithium in Bulk Amorphous Silicon : A Theoretical Study". In: (2012).

[46] Tzu Liang Chan and James R. Chelikowsky. "Controlling diffusion of lithium in silicon nanostructures". In: *Nano Letters* 10.3 (2010), pp. 821–825. ISSN: 15306984. DOI: 10.1021/nl903183n.

[47] Anix Casimir et al. "Silicon-based anodes for lithium-ion batteries: Effectiveness of materials synthesis and electrode preparation". In: *Nano Energy* 27 (2016), pp. 359–376. ISSN: 22112855. DOI: 10.1016/j.nanoen.2016.07.023. URL: http://dx.doi.org/10.1016/j.nanoen.2016.07.023.

[48] Daniel Thomas et al. "The heat capacity and entropy of lithium silicides over the temperature range from (2 to 873)K". In: *The Journal of Chemical Thermodynamics* 64 (2013), pp. 205–225. ISSN: 00219614. DOI: 10.1016/j.jct.2013.05.018. URL: http://linkinghub.elsevier.com/retrieve/pii/S0021961413001730.

[49] Won-Seok Chang et al. "Quartz (SiO2): a new energy storage anode material for Li-ion batteries". In: *Energy & Environmental Science* 5.5 (2012), p. 6895. ISSN: 1754-5692. DOI: 10.1039/c2ee00003b. URL: http://xlink.rsc.org/?DOI=c2ee00003b.

[50] Mingyan Wu et al. "In situ formed Si nanoparticle network with micron-sized Si particles for lithium-ion battery anodes". In: *Nano Letters* 13.11 (2013), pp. 5397–5402. ISSN: 15306984. DOI: 10.1021/nl402953h.

[51] Liangbing Hu et al. "Si nanoparticle-decorated Si nanowire networks for Li-ion battery anodes". In: *Chem. Commun.* 47.1 (2011), pp. 367–369. ISSN: 1359-7345. DOI: 10.1039/C0CC02078H. URL: http://xlink.rsc.org/?DOI=C0CC02078H.

[52] Hong Li et al. "Crystal structural evolution of nano-Si anode caused by lithium insertion and extraction at room temperature". In: *Solid State Ionics* 135.1-4 (2000), pp. 181–191. ISSN: 01672738. DOI: 10.1016/S0167-2738(00)00362-3.

[53] Ki Lyoung Lee et al. "Electrochemical characteristics of a-Si thin film anode for Li-ion rechargeable batteries". In: *Journal of Power Sources* 129.2 (2004), pp. 270–274. ISSN: 03787753. DOI: 10.1016/j.jpowsour.2003.10.013.

[54] L. B. Chen et al. "An amorphous Si thin film anode with high capacity and long cycling life for lithium ion batteries". In: *Journal of Applied Electrochemistry* 39.8 (2009), pp. 1157–1162. ISSN: 0021891X. DOI: 10.1007/s10800-008-9774-1.

[55] Yan Yao et al. "Interconnected silicon hollow nanospheres for lithium-ion battery anodes with long cycle life". In: *Nano Letters* 11.7 (2011), pp. 2949–2954. ISSN: 15306984. DOI: 10.1021/nl201470j.

[56] Xiaolin Li et al. "Hollow core–shell structured porous Si–C nanocomposites for Li-ion battery anodes". In: *Journal of Materials Chemistry* 22.22 (2012), p. 11014. ISSN: 0959-9428. DOI: 10.1039/c2jm31286g. URL: http://xlink.rsc.org/?DOI=c2jm31286g.

[57] Li-feng Cui et al. "Crystalline-Amorphous Core - Shell Silicon Nanowires for High Capacity and High Current Battery Electrodes 2009". In: (2009).

[58] Hyesun Kim and Jaephil Cho. "Superior Lithium Electroactive Mesoporous Si @ Carbon Core - Shell Nanowires for Lithium Battery Anode Material". In: *Nano Lett.* 8.11 (2008), pp. 3688–3691. DOI: 10.1021/nl801853x.

[59] B. E. Deal and A. S. Grove. "General relationship for the thermal oxidation of silicon". In: *Journal of Applied Physics* 36.12 (1965), pp. 3770–3778. ISSN: 00218979. DOI: 10.1063/1.1713945.

[60] N V Rumak and V V Khatko. "Structure and Properties of Silicon Dioxide Thermal Films (II)". In: *Physica Status Solidi (a)* 477.86 (1984), pp. 477–484.

[61] M. Morita et al. "Growth of native oxide on a silicon surface". In: *Journal of Applied Physics* 68.3 (1990), pp. 1272–1281. ISSN: 00218979. DOI: 10.1063/1.347181.

[62] Jie Zhao et al. "Metallurgically lithiated SiOx anode with high capacity and ambient air compatibility". In: *Proceedings of the National Academy of Sciences* 113.27 (2016), pp. 7408–7413. ISSN: 0027-8424. DOI: 10.1073/pnas.1603810113. URL: http://www.pnas.org/lookup/doi/10.1073/pnas.1603810113.

[63] Sung Chul Jung et al. "Atomic-Level Understanding toward a High-Capacity and High-Power Silicon Oxide (SiO) Material". In: *Journal of Physical Chemistry C* 120.2 (2016), pp. 886–892. ISSN: 19327455. DOI: 10.1021/acs.jpcc.5b10589.

[64] Chia Yun Chou and Gyeong S. Hwang. "Lithiation behavior of silicon-rich oxide (SiO1/3): A first-principles study". In: *Chemistry of Materials* 25.17 (2013), pp. 3435–3440. ISSN: 08974756. DOI: 10.1021/cm401303n.

[65] S. Xun et al. "The Effects of Native Oxide Surface Layer on the Electrochemical Performance of Si Nanoparticle-Based Electrodes". In: *Journal of The Electrochemical Society* 158.12 (2011), A1260. ISSN: 00134651. DOI: 10.1149/2.007112jes. URL: http://jes.ecsdl.org/cgi/doi/10.1149/2.007112jes.

[66] Nava Ariel et al. "Electrochemically controlled transport of lithium through ultrathin SiO2". In: *Journal of Applied Physics* 98.2 (2005). ISSN: 00218979. DOI: 10.1063/1.1989431.

[67] Yuefei Zhang et al. "Lithiation of SiO2 in Li-Ion Batteries: In Situ Transmission Electron Microscopy Experiments and Theoretical Studies". In: *Nano letters* 14 (2014), pp. 7161–7170. ISSN: 1530-6992. DOI: 10.1021/nl503776u.

[68] Bingkun Guo et al. "Electrochemical reduction of nano-SiO2 in hard carbon as anode material for lithium ion batteries". In: *Electrochemistry Communications* 10.12 (2008), pp. 1876–1878. ISSN: 13882481. DOI: 10.1016/j.elecom.2008.09.032. URL: http://dx.doi.org/10.1016/j.elecom.2008.09.032.

[69] Nan Yan et al. "Hollow Porous SiO2 Nanocubes Towards High-performance Anodes for Lithium-ion Batteries". In: *Scientific Reports* 3.1 (2013), p. 1568. ISSN: 2045-2322. DOI: 10.1038/srep01568. URL: http://www.nature.com/articles/srep01568.

[70] Erwin Hüger et al. "Lithium transport through nanosized amorphous silicon layers". In: *Nano Letters* 13.3 (2013), pp. 1237–1244. ISSN: 15306984. DOI: 10.1021/nl304736t.

[71] T. L. Kulova et al. "Lithium intercalation into amorphous-silicon thin films: An electrochemical-impedance study". In: *Russian Journal of Electrochemistry* 42.7 (2006), pp. 708–714. ISSN: 1023-1935. DOI: 10.1134/S1023193506070032. URL: http://link.springer.com/10.1134/S1023193506070032.

[72] Andreas Dunst et al. "Fast Li+Self-Diffusion in Amorphous Li-Si Electrochemically Prepared from Semiconductor Grade, Monocrystalline Silicon: Insights from Spin-Locking Nuclear Magnetic Relaxometry". In: *Journal of Physical Chemistry C* 119.22 (2015), pp. 12183–12192. ISSN: 19327455. DOI: 10.1021/acs.jpcc.5b02490.

[73] C. S. Fuller and J. A. Ditzenberger. "Diffusion of lithium into germanium and silicon [1]". In: *Physical Review* 91.1 (1953), p. 193. ISSN: 0031899X. DOI: 10.1103/PhysRev.91.193.

[74] Kazutaka Yoshimura et al. "Measurement of the diffusion rate of Li in silicon by the use of bipolar cells". In: *Journal of Power Sources* 174.2 (2007), pp. 653–657. ISSN: 03787753. DOI: 10.1016/j.jpowsour.2007.06.115.

[75] K. Yoshimura et al. "Determination of the Diffusion Coefficient of Lithium in Silicon". In: 441 (2005), p. 2017.

[76] Musheng Wu, Bo Xu, and Chuying Ouyang. "Physics of electron and lithium-ion transport in electrode materials for Li-ion batteries". In: *Chinese Physics B* 25.1 (2015). ISSN: 20583834. DOI: 10.1088/1674-1056/25/1/018206.

[77] N. Ding et al. "Determination of the diffusion coefficient of lithium ions in nano-Si". In: *Solid State Ionics* 180.2-3 (2009), pp. 222–225. ISSN: 01672738. DOI: 10.1016/j.ssi.2008.12.015. URL: http://dx.doi.org/10.1016/j.ssi.2008.12.015.

[78] E. M. Pell. "Diffusion Rate of Li in Si at Low Temperatures". In: *Physical Review* 119.4 (1960), pp. 1222–1225.

[79] Erwin Hüger, Lars Dörrer, and Harald Schmidt. "Permeation, Solubility, Diffusion and Segregation of Lithium in Amorphous Silicon Layers". In: *Chemistry of Materials* 30.10 (2018), pp. 3254–3264. ISSN: 0897-4756. DOI: 10.1021/acs.chemmater.8b00186. URL: http://pubs.acs.org/doi/10.1021/acs.chemmater.8b00186.

[80] Priya Johari, Yue Qi, and Vivek B. Shenoy. "The mixing mechanism during lithiation of Si negative electrode in Li-ion batteries: An Ab initio molecular dynamics study". In: *Nano Letters* 11.12 (2011), pp. 5494–5500. ISSN: 15306984. DOI: 10.1021/nl203302d.

[81] Zhiguo Wang et al. "Composition Dependence of Lithium Diffusion in Lithium Silicide: A Density Functional Theory Study". In: *ChemElectroChem* 2.9 (2015), pp. 1292–1297. ISSN: 21960216. DOI: 10.1002/celc.201500201.

[82] Georgios A. Tritsaris et al. "Diffusion of lithium in bulk amorphous silicon: A theoretical study". In: *Journal of Physical Chemistry C* 116.42 (2012), pp. 22212–22216. ISSN: 19327447. DOI: 10.1021/jp307221q.

[83] Janghyuk Moon et al. "Ab initio and kinetic Monte Carlo simulation study of lithiation in crystalline and amorphous silicon". In: *Journal of Power Sources* 272 (2014), pp. 1010–1017. ISSN: 03787753. DOI: 10.1016/j.jpowsour.2014.09.004.

[84] Xin Yan, Afif Gouissem, and Pradeep Sharma. "Atomistic insights into Li-ion diffusion in amorphous silicon". In: *Mechanics of Materials* 91 (2015), pp. 306–312. ISSN: 01676636. DOI: 10.1016/j.mechmat.2015.04.001. URL: http://dx.doi.org/10.1016/j.mechmat.2015.04.001.

[85] Zhi Xu and Jonathan F Stebbins. "Cation Dynamics and Diffusion in Lithium Orthosilicate : Two-Dimensional Lithium-6 NMR A". In: *Science* 270.5240 (1995), pp. 1332–1334.

[86] Martin Wilkening and Paul Heitjans. "Extremely slow cation exchange processes in Li4SiO4 probed directly by two-time 7Li stimulated-echo nuclear magnetic resonance spectroscopy". In: *Journal of Physics Condensed Matter* 18.43 (2006), pp. 9849–9862. ISSN: 09538984. DOI: 10.1088/0953-8984/18/43/007.

[87] Elke Göbel et al. "7Li NMR spectra, nuclear relaxation, and lithium ion motion in alkali silicate, borate, and phosphate glasses". In: *Journal of Magnetic Resonance (1969)* 36.3 (1979), pp. 371–387. ISSN: 00222364. DOI: 10.1016/0022-2364(79)90114-8.

[88] Alireza Ostadhossein et al. "Atomic Insight into the Lithium Storage and Diffusion Mechanism of SiO2/Al2O3 Electrodes of Lithium Ion Batteries: ReaxFF Reactive Force Field Modeling". In: *The Journal of Physical Chemistry A* 120.13 (2016), pp. 2114–2127. ISSN: 1089-5639. DOI: 10.1021/acs.jpca.5b11908. URL: http://pubs.acs.org/doi/10.1021/acs.jpca.5b11908.

[89] Jincheng Du and Chao Hsu Chen. "Structure and lithium ion diffusion in lithium silicate glasses and at their interfaces with lithium lanthanum titanate crystals". In: *Journal of Non-Crystalline Solids* 358.24 (2012), pp. 3531–3538. ISSN: 00223093. DOI: 10.1016/j.jnoncrysol.2012.05.015. URL: http://dx.doi.org/10.1016/j.jnoncrysol.2012.05.015.

[90] G. Kresse and J. Furthmüller. "Efficiency of ab-initio total energy calculations for metals and semiconductors using a plane-wave basis set". In: *Computational Materials Science* 6.1 (1996), pp. 15–50. ISSN: 09270256. DOI: 10.1016/0927-0256(96)00008-0.

[91] G. Kresse and J. Furthmüller. "Efficient iterative schemes for ab initio total-energy calculations using a plane-wave basis set". In: *Physical Review B - Condensed Matter and Materials Physics* 54.16 (1996), pp. 11169–11186. ISSN: 1550235X. DOI: 10.1103/PhysRevB.54.11169.

[92] P. E. Blöchl. "Projector augmented-wave method". In: *Physical Review B* 50.24 (1994), pp. 17953–17979. ISSN: 01631829. DOI: 10.1103/PhysRevB.50.17953.

[93] John P. Perdew, Kieron Burke, and Matthias Ernzerhof. "Generalized gradient approximation made simple". In: *Physical Review Letters* 77.18 (1996), pp. 3865–3868. ISSN: 10797114. DOI: 10.1103/PhysRevLett.77.3865.

[94] Anubhav Jain et al. "FireWorks: a dynamic workflow system designed for high-throughput applications". In: *Concurrency and Computation: Practice and Experience* 27.17 (Dec. 2015), pp. 5037–5059. ISSN: 15320626. DOI: 10.1002/cpe.3505. URL: http://doi.wiley.com/10.1002/cpe.3505.

[95] Kiran Mathew et al. "Atomate: A high-level interface to generate, execute, and analyze computational materials science workflows". In: *Computational Materials Science* 139 (Nov. 2017), pp. 140–152. ISSN: 09270256. DOI: 10.1016/j.commatsci.2017.07.030. URL: http://perssongroup.lbl.gov/papers/mathew-2017-atomate.pdf%20http://linkinghub.elsevier.com/retrieve/pii/S0927025617303919.

[96] Lei Wang, Thomas Maxisch, and Gerbrand Ceder. "Oxidation energies of transition metal oxides within the GGA+U framework". In: *Physical Review B - Condensed Matter and Materials Physics* 73.19 (2006), pp. 1–6. ISSN: 10980121. DOI: 10.1103/PhysRevB.73.195107.

[97] Yongli Wang, Yongsheng Zhang, and C. Wolverton. "First-principles studies of phase stability and crystal structures in Li-Zn mixed-metal borohydrides". In: *Physical Review B - Condensed Matter and Materials Physics* 88.2 (2013), pp. 1–10. ISSN: 10980121. DOI: 10.1103/PhysRevB.88.024119.

[98] M. K. Aydinol et al. "Ab initio study of lithium intercalation in metal oxides and metal dichalcogenides". In: *Physical Review B* 56.3 (1997), pp. 1354–1365. ISSN: 0163-1829. DOI: 10.1103/PhysRevB.56.1354. URL: http://link.aps.org/doi/10.1103/PhysRevB.56.1354.

[99] Alexander Urban, Dong-Hwa Seo, and Gerbrand Ceder. "Computational understanding of Li-ion batteries". In: *npj Computational Materials* 2.October 2015 (2016), p. 16002. ISSN: 2057-3960. DOI: 10.1038/npjcompumats.2016.2. URL: http://www.nature.com/articles/npjcompumats20162.

[100] Xingfeng He et al. "Statistical variances of diffusional properties from ab initio molecular dynamics simulations". In: *npj Computational Materials* 4.1 (2018). ISSN: 20573960. DOI: 10.1038/s41524-018-0074-y. URL: http://dx.doi.org/10.1038/s41524-018-0074-y.

[101] Thomas K J Koster et al. "Resolving the different silicon clusters in Li 12Si 7 by 29Si and 6,7Li solid-state NMR spectroscopy". In: *Angewandte Chemie - International Edition* 50.52 (2011), pp. 12591–12594. ISSN: 14337851. DOI: 10.1002/anie.201105998.

[102] Baris Key et al. "Real-time NMR investigations of structural changes in silicon electrodes for lithium-ion batteries". In: *Journal of the American Chemical Society* 131.26 (2009), pp. 9239–9249. ISSN: 00027863. DOI: 10.1021/ja8086278.

[103] Han-Hsin Chiang, Jian-Ming Lu, and Chin-Lung Kuo. "First-principles study of the structural and dynamic properties of the liquid and amorphous Li–Si alloys". In: *The Journal of Chemical Physics* 144.3 (2016), p. 034502. ISSN: 0021-9606. DOI: 10.1063/1.4939716. URL: http://aip.scitation.org/doi/10.1063/1.4939716.

[104] K Ogata et al. "Revealing lithium-silicide phase transformations in nano-structured silicon-based lithium ion batteries via in situ NMR spectroscopy." In: *Nature communications* 5 (2014), p. 3217. ISSN: 2041-1723. DOI: 10.1038/ncomms4217. URL: http://www.ncbi.nlm.nih.gov/pubmed/24488002%5Cnhttp://www.nature.com/ncomms/2014/140203/ncomms4217/full/ncomms4217.html.

[105] Reinhard Nesper, Hans Georg von Schnering, and Jan Curda. "Li12Si7, eine Verbindung mit trigonal-planaren Si4-Clustern und isometrischen Si5-Ringen". In: *Chemische Berichte* 119.12 (1986), pp. 3576–3590. ISSN: 10990682. DOI: 10.1002/cber.19861191207.

[106] V. L. Chevrier and J. R. Dahn. "First principles studies of disordered lithiated silicon". In: *Journal of the Electrochemical Society* 157.4 (2010), pp. 392–398. ISSN: 00134651. DOI: 10.1149/1.3294772.

[107] V. L. Chevrier, J. W. Zwanziger, and J. R. Dahn. "First principles study of Li-Si crystalline phases: Charge transfer, electronic structure, and lattice vibrations". In: *Journal of Alloys and Compounds* 496.1-2 (2010), pp. 25–36. ISSN: 09258388. DOI: 10.1016/j.jallcom.2010.01.142. URL: http://dx.doi.org/10.1016/j.jallcom.2010.01.142.

[108] Hyunwoo Kim et al. "Structure and properties of Li-Si alloys: A first-principles study". In: *Journal of Physical Chemistry C* 115.5 (2011), pp. 2514–2521. ISSN: 19327447. DOI: 10.1021/jp1083899.

[109] Hyun Jung et al. "Atomistics of the lithiation of oxidized silicon (SiOx) nanowires in reactive molecular dynamics simulations". In: *Phys. Chem. Chem. Phys.* 18.47 (2016), pp. 32078–32086. ISSN: 1463-9076. DOI: 10.1039/C6CP06158C. URL: http://xlink.rsc.org/?DOI=C6CP06158C.

[110] C. John Wen and Robert A. Huggins. "Chemical diffusion in intermediate phases in the lithium-silicon system". In: *Journal of Solid State Chemistry* 37.3 (1981), pp. 271–278. ISSN: 1095726X. DOI: 10.1016/0022-4596(81)90487-4.

[111] Yoshiyuki Kubota et al. "Crystal and electronic structure of Li15Si4". In: *Journal of Applied Physics* 102.5 (2007). ISSN: 00218979. DOI: 10.1063/1.2775999.

[112] Shoutao Zhang et al. "Silicon Framework-Based Lithium Silicides at High Pressures". In: *ACS Applied Materials and Interfaces* 8.26 (2016), pp. 16761–16767. ISSN: 19448252. DOI: 10.1021/acsami.6b04308.

[113] Sung Chul Jung and Young Kyu Han. "Ab initio molecular dynamics simulation of lithiation-induced phase-transition of crystalline silicon". In: *Electrochimica Acta* 62 (2012), pp. 73–76. ISSN: 00134686. DOI: 10.1016/j.electacta.2011.11.093. URL: http://dx.doi.org/10.1016/j.electacta.2011.11.093.

[114] Zhiguo Wang et al. "Electron-rich driven electrochemical solid-state amorphization in Li-Si alloys". In: *Nano Letters* 13.9 (2013), pp. 4511–4516. ISSN: 15306984. DOI: 10.1021/nl402429a.

[115] Pimpa Limthongkul et al. "Electrochemically-driven solid-state amorphization in lithium-silicon alloys and implications for lithium storage". In: *Acta Materialia* 51.4 (2003), pp. 1103–1113. ISSN: 13596454. DOI: 10.1016/S1359-6454(02)00514-1.

[116] Jing Li and J. R. Dahn. "An In Situ X-Ray Diffraction Study of the Reaction of Li with Crystalline Si". In: *Journal of The Electrochemical Society* 154.3 (2007), A156. ISSN: 00134651. DOI: 10.1149/1.2409862. URL: http://jes.ecsdl.org/cgi/doi/10.1149/1.2409862.

[117] M. N. Obrovac and L. J. Krause. "Reversible Cycling of Crystalline Silicon Powder". In: *Journal of The Electrochemical Society* 154.2 (2007), A103. ISSN: 00134651. DOI: 10.1149/1.2402112. URL: http://jes.ecsdl.org/cgi/doi/10.1149/1.2402112.

[118] Zachary Favors et al. "Stable Cycling of SiO2 Nanotubes as High-Performance Anodes for Lithium-Ion Batteries". In: *Scientific Reports* 4.1 (2015), p. 4605. ISSN: 2045-2322. DOI: 10.1038/srep04605. URL: http://www.nature.com/articles/srep04605.

[119] Qian Sun, Bing Zhang, and Zheng-Wen Fu. "Lithium electrochemistry of SiO2 thin film electrode for lithium-ion batteries". In: *Applied Surface Science* 254.13 (Apr. 2008), pp. 3774–3779. ISSN: 01694332. DOI: 10.1016/j.apsusc.2007.11.058. URL: http://linkinghub.elsevier.com/retrieve/pii/S0169433207016832.

[120] H Xia et al. "Electrochemical behavior and Li Diffusion Study of LiCo2 thin film electrodes prepared by PLD". In: (2007). URL: http://hdl.handle.net/1721.1/35827.

[121] Yun Xu et al. "Mechanical Properties and Chemical Reactivity of Li x SiO y Thin Films". In: *ACS Applied Materials and Interfaces* 10.44 (2018), pp. 38558–38564. ISSN: 19448252. DOI: 10.1021/acsami.8b10895.

[122] Yoon Hwa, Cheol Min Park, and Hun Joon Sohn. "Modified SiO as a high performance anode for Li-ion batteries". In: *Journal of Power Sources* 222 (2013). ISSN: 03787753. DOI: 10.1016/jjpowsour.2012.08.060.

[123] J. K. Lee, W. Y. Yoon, and B. K. Kim. "Kinetics of Reaction Products of Silicon Monoxide with Controlled Amount of Li-Ion Insertion at Various Current Densities for Li-Ion Batteries". In: *Journal of the Electrochemical Society* 161.6 (2014), A927–A933. ISSN: 0013-4651. DOI: 10.1149/2.040406jes. URL: http://jes.ecsdl.org/cgi/doi/10.1149/2.040406jes.

[124] M. Mali et al. "6Li and 7Li diffusion coefficients in solid lithium measured by the NMR pulsed field gradient technique". In: *Journal of Physics F: Metal Physics* 18.3 (1988), pp. 403–412. ISSN: 03054608. DOI: 10.1088/0305-4608/18/3/011.

[125] P. Heitjans et al. "Self-diffusion in solid lithium probed by spin-lattice relaxation of 8Li nuclei". In: *Journal of Physics F: Metal Physics* 15.1 (1985), pp. 41–54. ISSN: 03054608. DOI: 10.1088/0305-4608/15/1/009.

[126] A. Lodding, J. N. Mundy, and A Ott. "Isotope inter- diffusion and self- diffusion in solid lithium metal". In: *Phys Status Solidi* 38.2 (1970), pp. 559–569. URL: /home/ihorn/CORE/Bibus/lodding1970.pdf.

[127] Huajun Tian et al. "High capacity group-IV elements (Si, Ge, Sn) based anodes for lithium-ion batteries". In: *Journal of Materiomics* 1.3 (2015), pp. 153–169. ISSN: 23528478. DOI: 10.1016/j.jmat.2015.06.002. URL: http://www.sciencedirect.com/science/article/pii/S2352847815000477.

[128] Yan Jin et al. "Challenges and recent progress in the development of Si anodes for lithium-ion battery". In: *Advanced Energy Materials* 7.23 (2017). ISSN: 16146840. DOI: 10.1002/aenm.201700715.

[129] Yanli Yin et al. "Nonpassivated Silicon Anode Surface". In: *ACS Applied Materials and Interfaces* 12.23 (2020), pp. 26593–26600. ISSN: 19448252. DOI: 10.1021/acsami.0c03799.

[130] Yang He et al. "Progressive growth of the solid–electrolyte interphase towards the Si anode interior causes capacity fading". In: *Nature Nanotechnology* (2021). ISSN: 17483395. DOI: 10.1038/s41565-021-00947-8. URL: http://dx.doi.org/10.1038/s41565-021-00947-8.

[131] I. A. Courtney et al. "Ab initio calculation of the lithium-tin voltage profile". In: *Physical Review B* 58.23 (Dec. 1998), pp. 15583–15588. ISSN: 0163-1829. DOI: 10.1103/PhysRevB.58.15583. URL: https://link.aps.org/doi/10.1103/PhysRevB.58.15583.

[132] Gaelle Derrien et al. "Nanostructured Sn-C composite as an advanced anode material in high-performance lithium-ion batteries". In: *Advanced Materials* 19.17 (2007), pp. 2336–2340. ISSN: 09359648. DOI: 10.1002/adma.200700748.

[133] Noriyuki Tamura et al. "Study on the anode behavior of Sn and Sn-Cu alloy thin-film electrodes". In: *Journal of Power Sources* 107.1 (2002), pp. 48–55. ISSN: 03787753. DOI: 10.1016/S0378-7753(01)00979-X.

[134] *ElementData*. Wolfram Research. 2014. URL: https://reference.wolfram.com/language/ref/ElementData.html.

[135] T. D. Hatchard and J. R. Dahn. "Study of the Electrochemical Performance of Sputtered Si[sub 1 x]Sn[sub x] Films". In: *Journal of The Electrochemical Society* 151.10 (2004), A1628. ISSN: 00134651. DOI: 10.1149/1.1790533. URL: http://jes.ecsdl.org/cgi/doi/10.1149/1.1790533.

[136] Kang Yao et al. "Chemical Reduction Synthesis and Electrochemistry of Si-Sn Nanocomposites as High-Capacity Anodes for Li-Ion Batteries". In: *Journal of Physical Chemistry Letters* 9.17 (2018), pp. 5130–5134. ISSN: 19487185. DOI: 10.1021/acs.jpclett.8b02066.

[137] Xingcheng Xiao et al. "Phase-separated silicon-tin nanocomposites for high capacity negative electrodes in lithium ion batteries". In: *Journal of Power Sources* 214 (2012), pp. 258–265. ISSN: 03787753. DOI: 10.1016/j.jpowsour.2012.04.028.

[138] L. Y. Beaulieu et al. "The Electrochemical Reaction of Li with Amorphous Si-Sn Alloys". In: *Journal of The Electrochemical Society* 150.2 (2003), A149. ISSN: 00134651. DOI: 10.1149/1.1530151.

[139] Jing Xu et al. "Facile Synthesis and Electrochemistry of Si-Sn-C Nanocomposites for High-Energy Li-Ion Batteries". In: *Journal of The Electrochemical Society* 164.7 (2017), A1378–A1383. ISSN: 0013-4651. DOI: 10.1149/2.0241707jes.

[140] M. J. Loveridge et al. "Binder-free Sn-Si heterostructure films for high capacity Li-ion batteries". In: *RSC Advances* 8.30 (2018), pp. 16726–16737. ISSN: 20462069. DOI: 10.1039/c7ra13489d.

[141] Chao Wang et al. "Composite of tin and silicon with nanostructure as high performance lithium-ion battery anode". In: *International Journal of Electrochemical Science* 15 (2020), pp. 3054–3067. ISSN: 14523981. DOI: 10.20964/2020.04.34.

[142] R.W. Olesinkski and G.J. Abbaschian. "The Si-Sn (Silicon-Tin) System". In: *Bulletin of Alloy Phase Diagrams* 5.3 (1984), pp. 273–276.

[143] Anubhav Jain et al. "Commentary: The materials project: A materials genome approach to accelerating materials innovation". In: *APL Materials* 1.1 (2013). ISSN: 2166532X. DOI: 10.1063/1.4812323.

[144] N. Matsuura, G. M. Hood, and H. Zou. "The correspondence between self-diffusion properties and melting temperatures for α-Zr and α-Ti". In: *Journal of Nuclear Materials* 238.2-3 (1996), pp. 260–263. ISSN: 00223115. DOI: 10.1016/S0022-3115(96)00458-8.

[145] G.P. Tiwari and R.S. Mehrotra. "Diffusion and Melting". In: *Defect and Diffusion Forum* 279 (2008), pp. 23–37. ISSN: 1662-9507. DOI: 10.4028/www.scientific.net/ddf.279.23.

[146] H. Okamoto. "Li-Si (Lithium-Silicon)". In: *Journal of Phase Equilibria and Diffusion* 30.1 (2009), pp. 118–119. ISSN: 1547-7037. DOI: 10.1007/s11669-008-9431-8.

[147] Ronald A. Guidotti and Patrick J. Masset. "Thermally activated ("thermal") battery technology. Part IV. Anode materials". In: *Journal of Power Sources* 183.1 (2008), pp. 388–398. ISSN: 03787753. DOI: 10.1016/j.jpowsour.2008.04.090.

[148] Wenhui Wan et al. "First principles study of lithium insertion in bulk silicon". In: *Journal of Physics Condensed Matter* 22.41 (2010). ISSN: 09538984. DOI: 10.1088/0953-8984/22/41/415501.

[149] Yanyan Zhao et al. "A Review on Battery Market Trends, Second-Life Reuse, and Recycling". In: *Sustainable Chemistry* 2.1 (2021), pp. 167–205. DOI: 10.3390/suschem2010011.

[150] *Global EV Outlook 2020*. International Energy Agency. 2020. URL: https://www.iea.org/reports/global-ev-outlook-2020.

[151] Chengjian Xu et al. "Future material demand for automotive lithium-based batteries". In: *Communications Materials* 1.1 (2020). ISSN: 2662-4443. DOI: 10.1038/s43246-020-00095-x. URL: http://dx.doi.org/10.1038/s43246-020-00095-x.

[152] Fangzhou Zhang and Jianping Yang. "Boosting initial coulombic efficiency of Si-based anodes: a review". In: *Emergent Materials* 3.3 (2020), pp. 369–380. ISSN: 2522574X. DOI: 10.1007/s42247-020-00080-7.

[153] Kevin Rhodes et al. "Understanding the Degradation of Silicon Electrodes for Lithium-Ion Batteries Using Acoustic Emission". In: *Journal of The Electrochemical Society* 157.12 (2010), A1354. ISSN: 00134651. DOI: 10.1149/1.3489374.

[154] Manuel Schnabel et al. "Stable SEI Formation on Al-Si-Mn Metallic Glass Li-Ion Anode". In: *Journal of The Electrochemical Society* 168.10 (2021), p. 100521. ISSN: 0013-4651. DOI: 10.1149/1945-7111/ac2d3f.

[155] T. D. Hatchard et al. "Electrochemical performance of SiAlSn films prepared by combinatorial sputtering". In: *Electrochemical and Solid-State Letters* 6.7 (2003), pp. 129–132. ISSN: 10990062. DOI: 10.1149/1.1574231.

[156] Akihisa Inoue. "High Strength Bulk Amorphous Alloys with Low Critical Cooling Rates (¡I¿Overview¡/I¿)". In: *Materials Transactions, JIM* 36.7 (1995), pp. 866–875. ISSN: 0916-1821. DOI: 10.2320/matertrans1989.36.866. URL: https://www.jstage.jst.go.jp/article/matertrans1989/36/7/36_7_866/_article.

[157] W. L. Johnson. "Bulk amorphous metal-An emerging engineering material". In: *Jom* 54.3 (2002), pp. 40–43. ISSN: 10474838. DOI: 10.1007/BF02822619.

[158] Mingwei Chen. "A brief overview of bulk metallic glasses". In: *NPG Asia Materials* 3.9 (2011), pp. 82–90. ISSN: 18844049. DOI: 10.1038/asiamat.2011.30.

[159] Zhi yuan Feng et al. "Review of silicon-based alloys for lithium-ion battery anodes". In: *International Journal of Minerals, Metallurgy and Materials* 28.10 (2021), pp. 1549–1564. ISSN: 1869103X. DOI: 10.1007/s12613-021-2335-x.

[160] F D Murnaghan. "Physics: f. d. murnaghan". In: (1944), pp. 244–247.

[161] Anton Van Der Ven et al. "Rechargeable Alkali-Ion Battery Materials: Theory and Computation". In: *Chemical Reviews* 120.14 (2020), pp. 6977–7019. ISSN: 15206890. DOI: 10.1021/acs.chemrev.9b00601.

[162] J. R. Dahn, R. E. Mar, and Alyaa Abouzeid. "Combinatorial Study of Sn[sub 1 x]Co[sub x] (0¡x¡0.6) and [Sn[sub 0.55]Co[sub 0.45]][sub 1 y]C[sub y] (0¡y¡0.5) Alloy Negative Electrode Materials for Li-Ion Batteries". In: *Journal of The Electrochemical Society* 153.2 (2006), A361. ISSN: 00134651. DOI: 10.1149/1.2150160. URL: https://iopscience.iop.org/article/10.1149/1.2150160.

[163] J. Robertson. "Amorphous carbon". In: *Advances in Physics* 35.4 (1986), pp. 317–374. ISSN: 14606976. DOI: 10.1080/00018738600101911.

[164] M. P. Ho and A. K.T. Lau. "Amorphous carbon nanocomposites". In: *Fillers and Reinforcements for Advanced Nanocomposites* 2 (2015), pp. 309–328. DOI: 10.1016/B978-0-08-100079-3.00012-0.

[165] Sekhar Chandra Ray. "Introduction: carbon and carbon nanomaterials". In: *Magnetism and Spintronics in Carbon and Carbon Nanostructured Materials* (2020), pp. 23–45. DOI: 10.1016/b978-0-12-817680-1.00002-0.

[166] H. Okamoto. "Cu-Li (Copper-Lithium)". In: *Journal of Phase Equilibria and Diffusion* 32.2 (2011), p. 172. ISSN: 18637345. DOI: 10.1007/s11669-010-9840-3.

[167] Rico Rupp et al. "Lithium Diffusion in Copper". In: *Journal of Physical Chemistry Letters* 10.17 (2019), pp. 5206–5210. ISSN: 19487185. DOI: 10.1021/acs.jpclett.9b02014.

[168] Weishang Jia et al. "A dual-phase Li-Ca alloy with a patternable and lithiophilic 3D framework for improving lithium anode performance". In: *Journal of Materials Chemistry A* 7.39 (2019), pp. 22377–22384. ISSN: 20507496. DOI: 10.1039/c9ta08798b.

[169] Yunok Kim et al. "Additional Lithium Storage on Dynamic Electrode Surface by Charge Redistribution in Inactive Ru Metal". In: *Small* 16.1 (Jan. 2020), p. 1905868. ISSN: 16136829. DOI: 10.1002/smll.201905868. URL: https://onlinelibrary.wiley.com/doi/10.1002/smll.201905868.

[170] Asbjørn Ulvestad et al. "Substoichiometric silicon nitride - An anode material for Li-ion batteries promising high stability and high capacity". In: *Scientific Reports* 8.1 (2018), pp. 1–13. ISSN: 20452322. DOI: 10.1038/s41598-018-26769-8.

[171] Hyungki Kim et al. "Germanium Silicon Alloy Anode Material Capable of Tunable Overpotential by Nanoscale Si Segregation". In: *Nano Letters* 15.6 (2015), pp. 4135–4142. ISSN: 15306992. DOI: 10.1021/acs.nanolett.5b01257.

[172] J. Wolfenstine. "CaSi2 as an anode for lithium-ion batteries". In: *Journal of Power Sources* 124.1 (2003), pp. 241–245. ISSN: 03787753. DOI: 10.1016/S0378-7753(03)00731-6.

[173] Kibum Kang et al. "Kinetics-driven high power Li-ion battery with A-Si/NiSix core-shell nanowire anodes". In: *Chemical Science* 2.6 (2011), pp. 1090–1093. ISSN: 20416520. DOI: 10.1039/c0sc00628a.

[174] Ning Du et al. "Ni3Si2-Si nanowires on Ni foam as a high-performance anode of Li-ion batteries". In: *Electrochemistry Communications* 13.12 (2011), pp. 1443–1446. ISSN: 13882481. DOI: 10.1016/j.elecom.2011.09.017. URL: http://dx.doi.org/10.1016/j.elecom.2011.09.017.

[175] Taeahn Kim, Sangjin Park, and Seung M. Oh. "Solid-State NMR and Electrochemical Dilatometry Study on Li[sup +] Uptake/Extraction Mechanism in SiO Electrode". In: *Journal of The Electrochemical Society* 154.12 (2007), A1112. ISSN: 00134651. DOI: 10.1149/1.2790282.

[176] M. A. Al-Maghrabi et al. " Combinatorial Studies of Si 1 x O x as a Potential Negative Electrode Material for Li-Ion Battery Applications ". In: *Journal of The Electrochemical Society* 160.9 (2013), A1587–A1593. ISSN: 0013-4651. DOI: 10.1149/2.115309jes.

[177] Fei Wang et al. "Prelithiation: A Crucial Strategy for Boosting the Practical Application of Next-Generation Lithium Ion Battery". In: *ACS Nano* 15.2 (Feb. 2021), pp. 2197–2218. ISSN: 1936-0851. DOI: 10.1021/acsnano.0c10664. URL: https://pubs.acs.org/doi/10.1021/acsnano.0c10664.

[178] Han Wang et al. "DeePMD-kit: A deep learning package for many-body potential energy representation and molecular dynamics". In: *Computer Physics Communications* 228 (2018), pp. 178–184. ISSN: 00104655. DOI: 10.1016/j.cpc.2018.03.016. URL: https://doi.org/10.1016/j.cpc.2018.03.016.

[179] Linfeng Zhang et al. "End-to-end symmetry preserving inter-atomic potential energy model for finite and extended systems". In: *Advances in Neural Information Processing Systems* 2018-Decem.NeurIPS 2018 (2018), pp. 4436–4446. ISSN: 10495258.

[180] Haoyi Mou et al. "Tin and Tin Compound Materials as Anodes in Lithium-Ion and Sodium-Ion Batteries: A Review". In: *Frontiers in Chemistry* 8.March (2020), pp. 1–14. ISSN: 22962646. DOI: 10.3389/fchem.2020.00141.

[181] Min Gu Park et al. "Sn-Based Nanocomposite for Li-Ion Battery Anode with High Energy Density, Rate Capability, and Reversibility". In: *ACS Nano* 12.3 (2018), pp. 2955–2967. ISSN: 1936086X. DOI: 10.1021/acsnano.8b00586.

Appendix A

Supplemental Information for Chapter 5

A.1 Formation Energies for Li-Si-X alloys

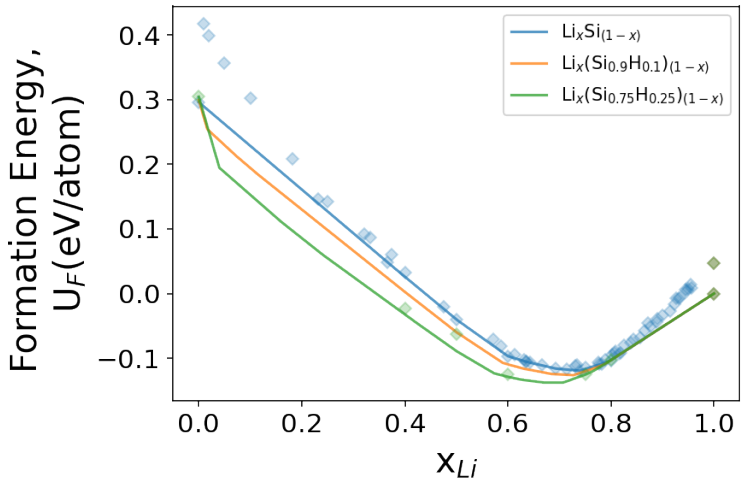

Figure A.1: Formation energy as a function of Li content for select compositions in the H-Li-Si chemical system. Lines represent cross-sectional planes of the amorphous hull. Calculated amorphous phases, coincident with the cross-sections, are marked with diamonds.

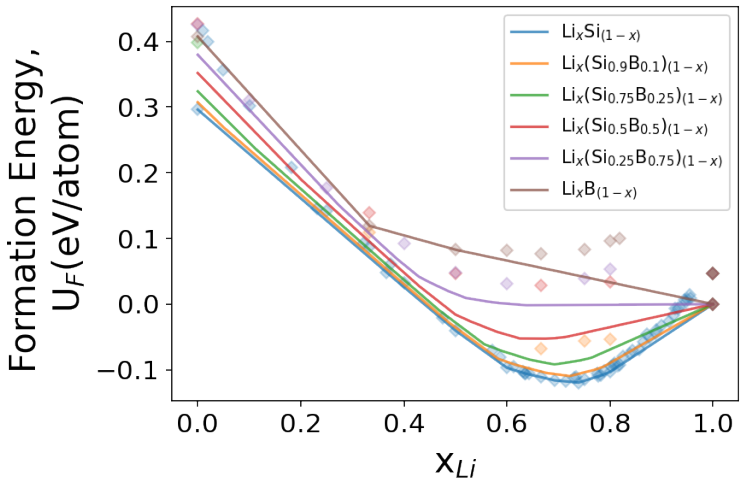

Figure A.2: Formation energy as a function of Li content for select compositions in the B-Li-Si chemical system. Lines represent cross-sectional planes of the amorphous hull. Calculated amorphous phases, coincident with the cross-sections, are marked with diamonds.

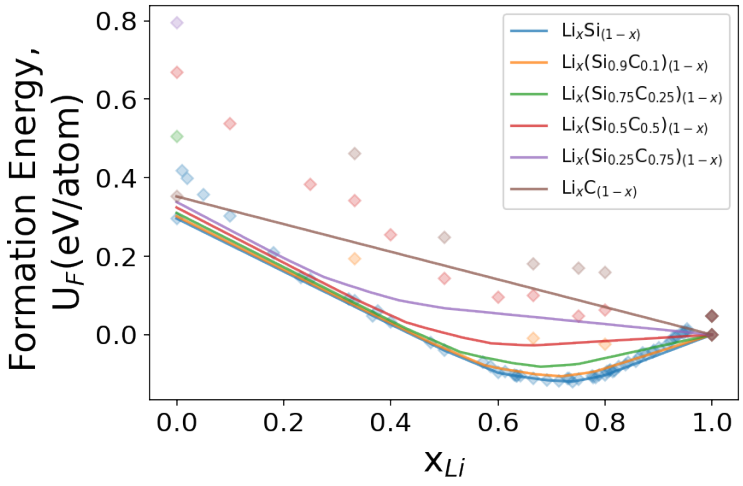

Figure A.3: Formation energy as a function of Li content for select compositions in the C-Li-Si chemical system. Lines represent cross-sectional planes of the amorphous hull. Calculated amorphous phases, coincident with the cross-sections, are marked with diamonds.

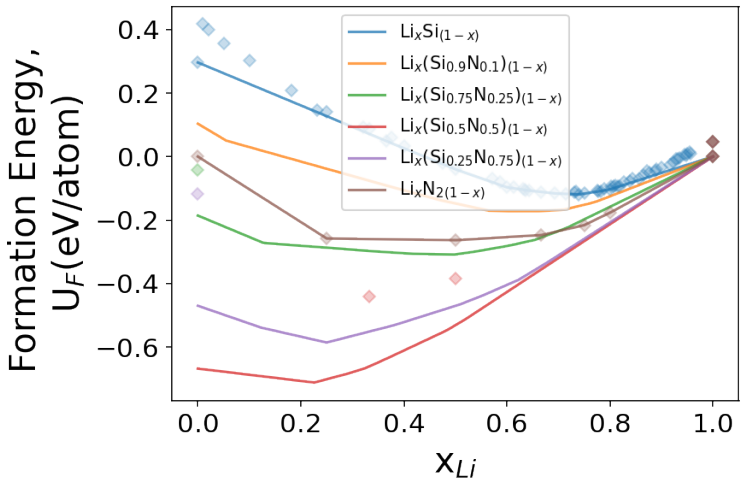

Figure A.4: Formation energy as a function of Li content for select compositions in the Li-N-Si chemical system. Lines represent cross-sectional planes of the amorphous hull. Calculated amorphous phases, coincident with the cross-sections, are marked with diamonds.

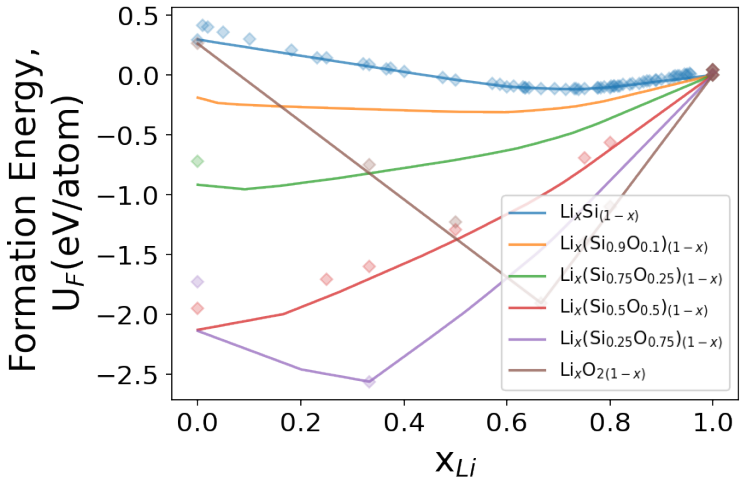

Figure A.5: Formation energy as a function of Li content for select compositions in the Li-O-Si chemical system. Lines represent cross-sectional planes of the amorphous hull. Calculated amorphous phases, coincident with the cross-sections, are marked with diamonds.

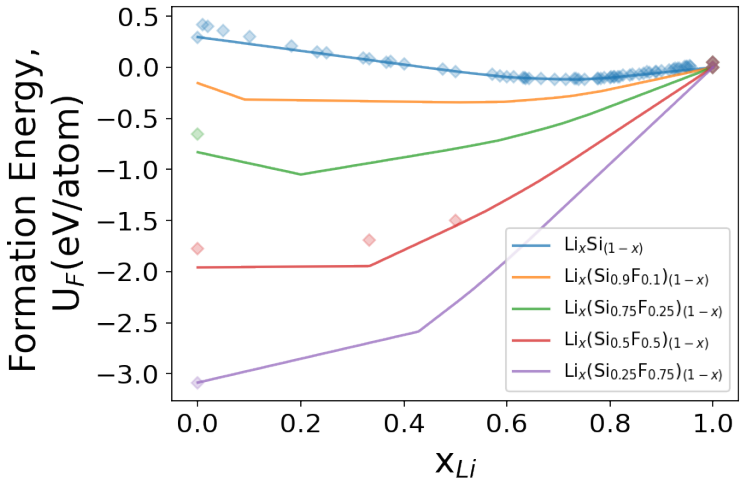

Figure A.6: Formation energy as a function of Li content for select compositions in the F-Li-Si chemical system. Lines represent cross-sectional planes of the amorphous hull. Calculated amorphous phases, coincident with the cross-sections, are marked with diamonds.

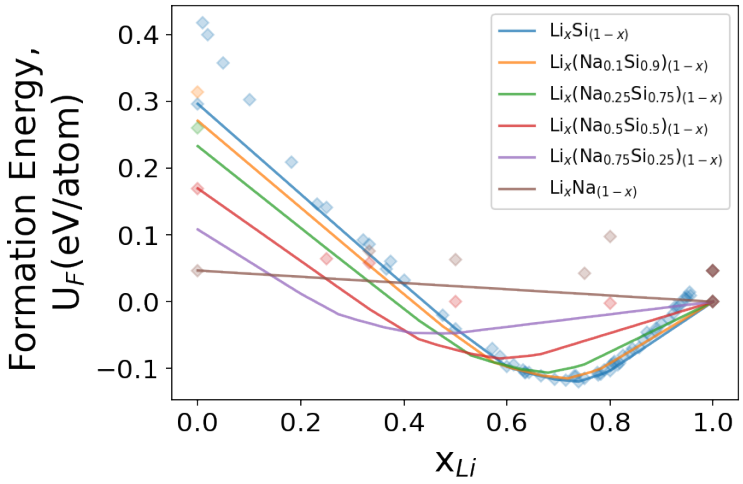

Figure A.7: Formation energy as a function of Li content for select compositions in the Li-Na-Si chemical system. Lines represent cross-sectional planes of the amorphous hull. Calculated amorphous phases, coincident with the cross-sections, are marked with diamonds.

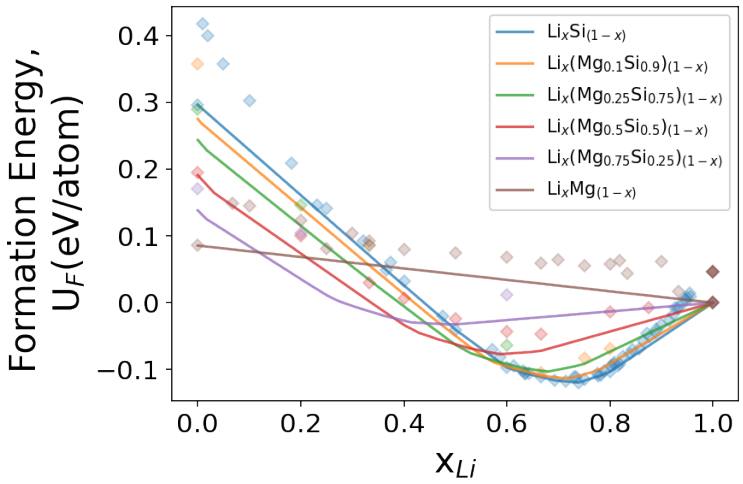

Figure A.8: Formation energy as a function of Li content for select compositions in the Li-Mg-Si chemical system. Lines represent cross-sectional planes of the amorphous hull. Calculated amorphous phases, coincident with the cross-sections, are marked with diamonds.

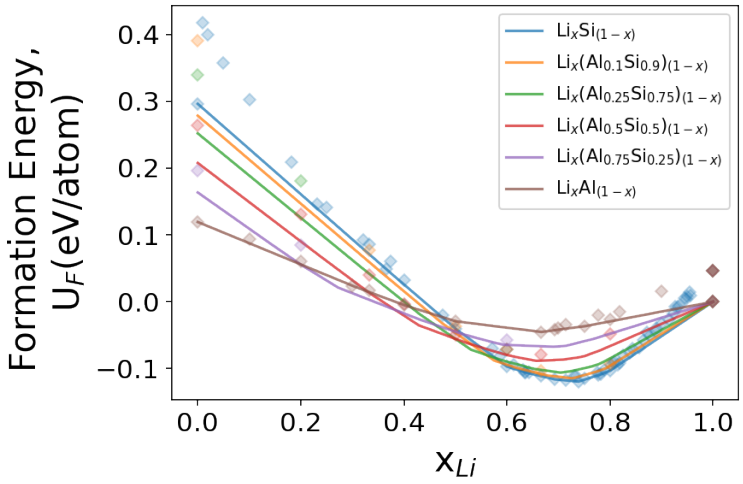

Figure A.9: Formation energy as a function of Li content for select compositions in the Al-Li-Si chemical system. Lines represent cross-sectional planes of the amorphous hull. Calculated amorphous phases, coincident with the cross-sections, are marked with diamonds.

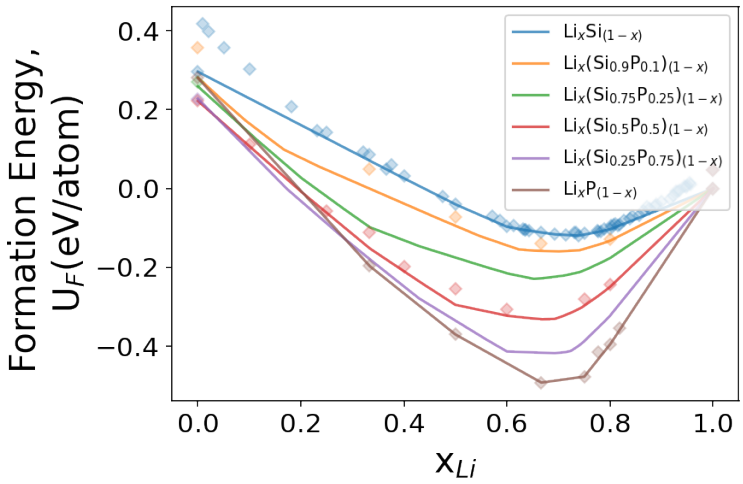

Figure A.10: Formation energy as a function of Li content for select compositions in the Li-P-Si chemical system. Lines represent cross-sectional planes of the amorphous hull. Calculated amorphous phases, coincident with the cross-sections, are marked with diamonds.

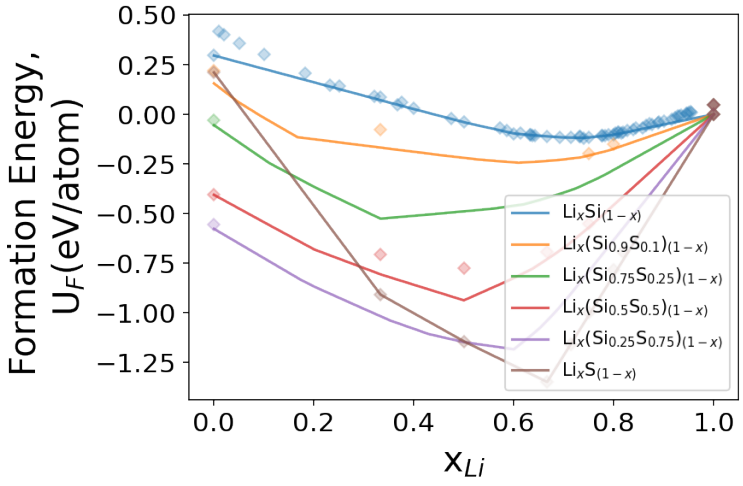

Figure A.11: Formation energy as a function of Li content for select compositions in the Li-S-Si chemical system. Lines represent cross-sectional planes of the amorphous hull. Calculated amorphous phases, coincident with the cross-sections, are marked with diamonds.

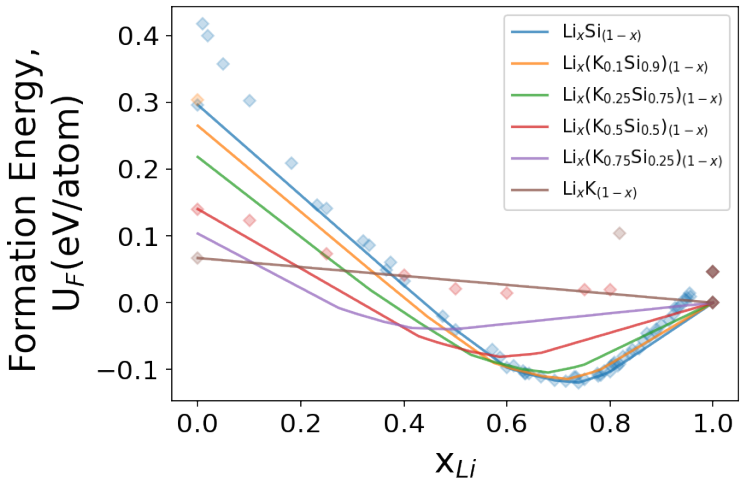

Figure A.12: Formation energy as a function of Li content for select compositions in the K-Li-Si chemical system. Lines represent cross-sectional planes of the amorphous hull. Calculated amorphous phases, coincident with the cross-sections, are marked with diamonds.

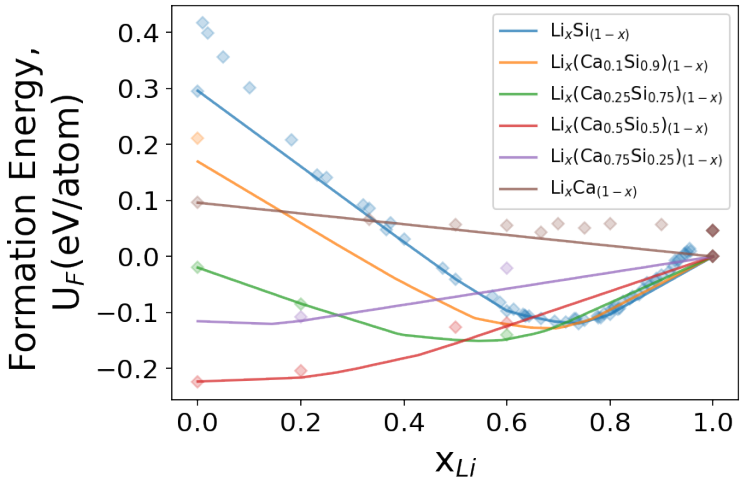

Figure A.13: Formation energy as a function of Li content for select compositions in the Ca-Li-Si chemical system. Lines represent cross-sectional planes of the amorphous hull. Calculated amorphous phases, coincident with the cross-sections, are marked with diamonds.

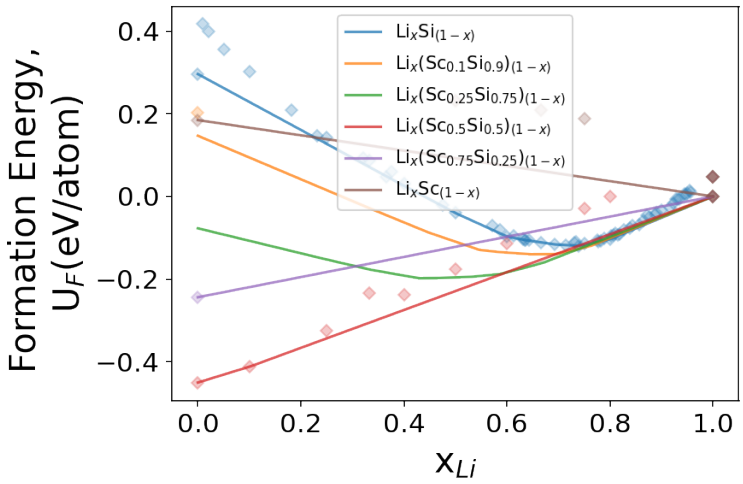

Figure A.14: Formation energy as a function of Li content for select compositions in the Li-Sc-Si chemical system. Lines represent cross-sectional planes of the amorphous hull. Calculated amorphous phases, coincident with the cross-sections, are marked with diamonds.

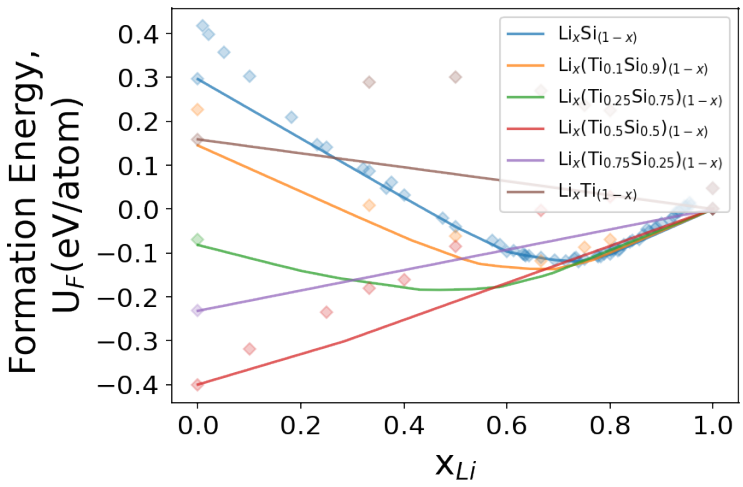

Figure A.15: Formation energy as a function of Li content for select compositions in the Li-Si-Ti chemical system. Lines represent cross-sectional planes of the amorphous hull. Calculated amorphous phases, coincident with the cross-sections, are marked with diamonds.

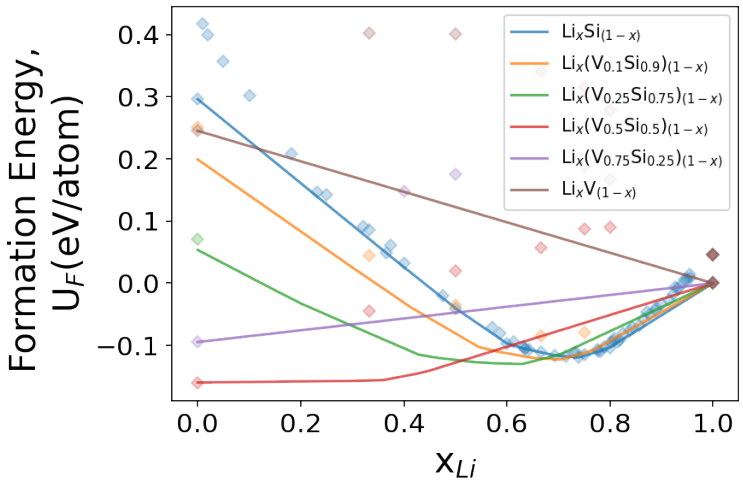

Figure A.16: Formation energy as a function of Li content for select compositions in the Li-Si-V chemical system. Lines represent cross-sectional planes of the amorphous hull. Calculated amorphous phases, coincident with the cross-sections, are marked with diamonds.

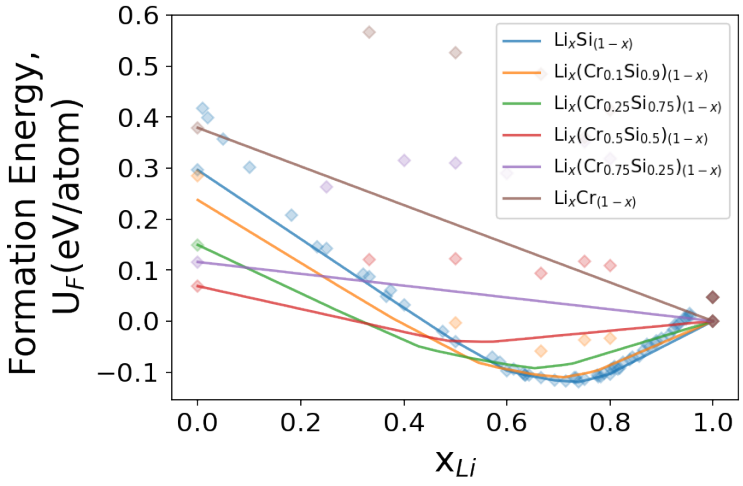

Figure A.17: Formation energy as a function of Li content for select compositions in the Cr-Li-Si chemical system. Lines represent cross-sectional planes of the amorphous hull. Calculated amorphous phases, coincident with the cross-sections, are marked with diamonds.

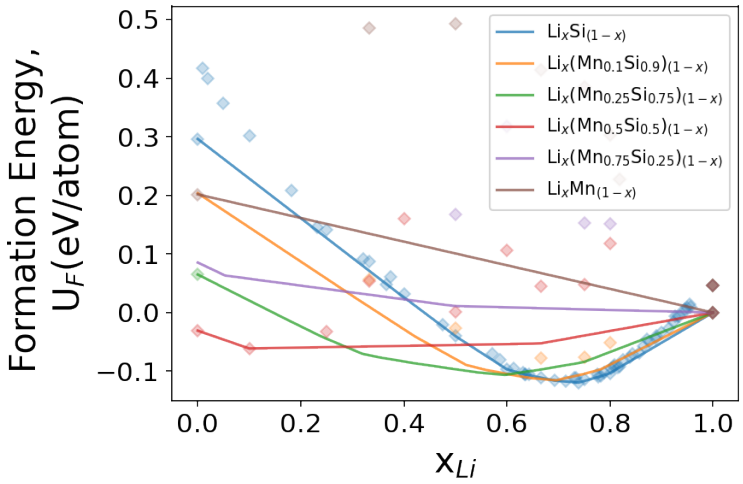

Figure A.18: Formation energy as a function of Li content for select compositions in the Li-Mn-Si chemical system. Lines represent cross-sectional planes of the amorphous hull. Calculated amorphous phases, coincident with the cross-sections, are marked with diamonds.

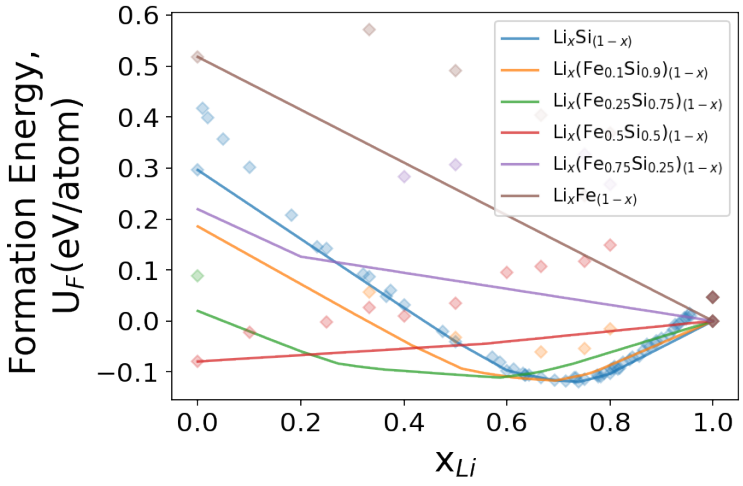

Figure A.19: Formation energy as a function of Li content for select compositions in the Fe-Li-Si chemical system. Lines represent cross-sectional planes of the amorphous hull. Calculated amorphous phases, coincident with the cross-sections, are marked with diamonds.

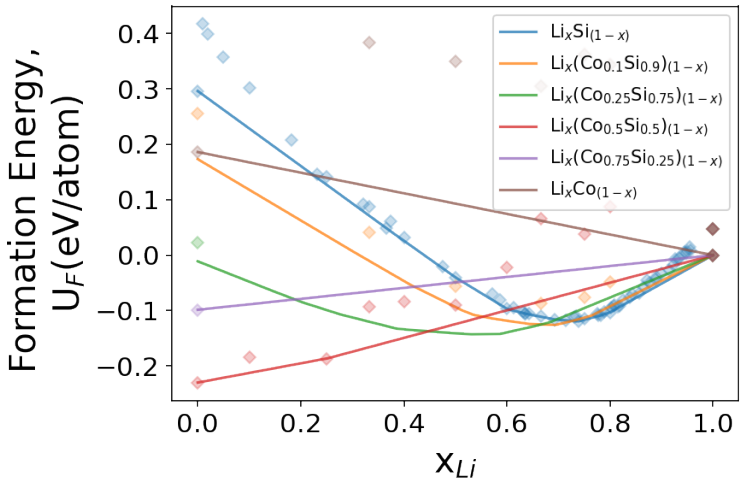

Figure A.20: Formation energy as a function of Li content for select compositions in the Co-Li-Si chemical system. Lines represent cross-sectional planes of the amorphous hull. Calculated amorphous phases, coincident with the cross-sections, are marked with diamonds.

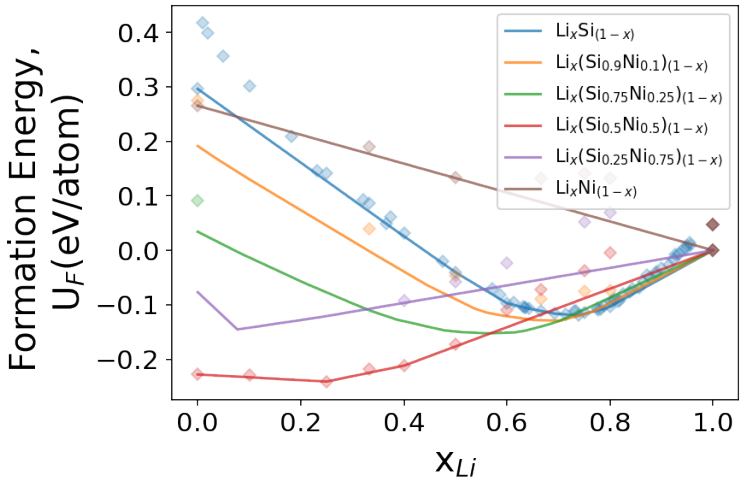

Figure A.21: Formation energy as a function of Li content for select compositions in the Li-Ni-Si chemical system. Lines represent cross-sectional planes of the amorphous hull. Calculated amorphous phases, coincident with the cross-sections, are marked with diamonds.

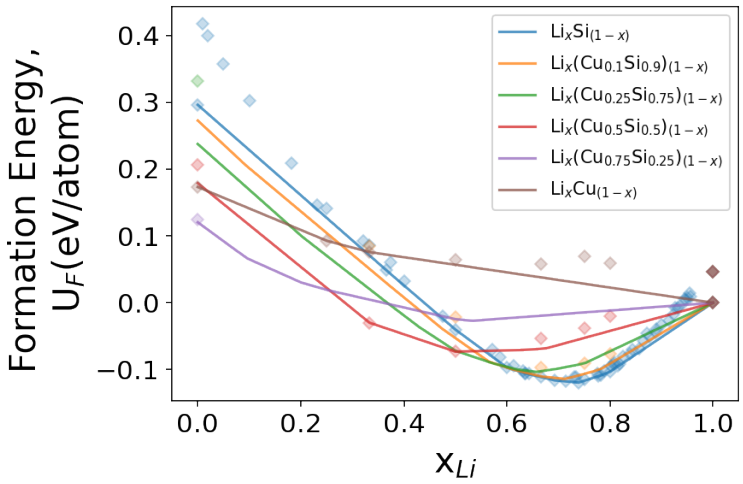

Figure A.22: Formation energy as a function of Li content for select compositions in the Cu-Li-Si chemical system. Lines represent cross-sectional planes of the amorphous hull. Calculated amorphous phases, coincident with the cross-sections, are marked with diamonds.

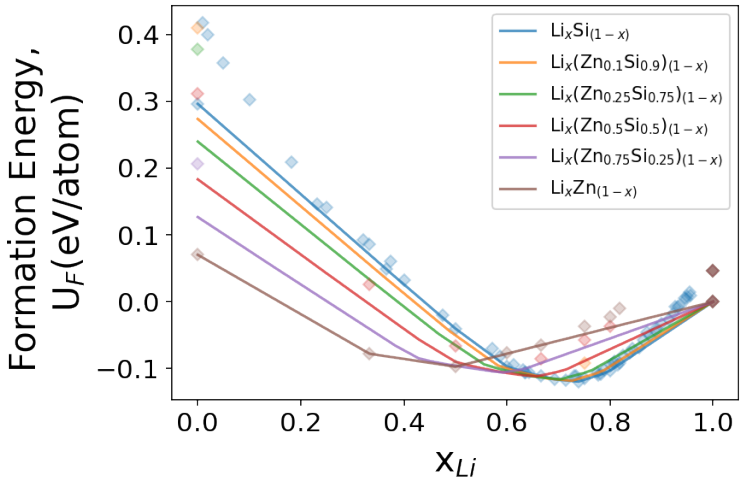

Figure A.23: Formation energy as a function of Li content for select compositions in the Li-Si-Zn chemical system. Lines represent cross-sectional planes of the amorphous hull. Calculated amorphous phases, coincident with the cross-sections, are marked with diamonds.

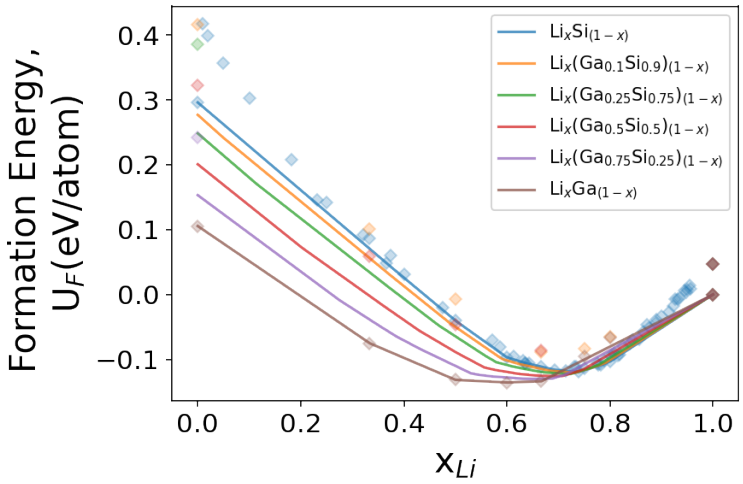

Figure A.24: Formation energy as a function of Li content for select compositions in the Ga-Li-Si chemical system. Lines represent cross-sectional planes of the amorphous hull. Calculated amorphous phases, coincident with the cross-sections, are marked with diamonds.

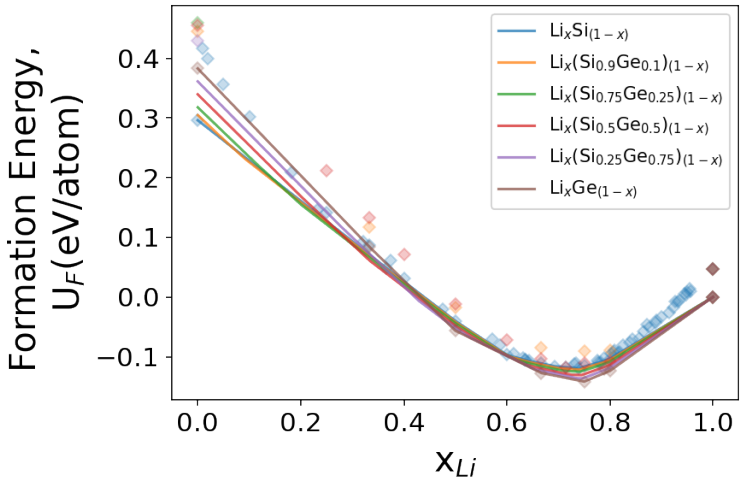

Figure A.25: Formation energy as a function of Li content for select compositions in the Ge-Li-Si chemical system. Lines represent cross-sectional planes of the amorphous hull. Calculated amorphous phases, coincident with the cross-sections, are marked with diamonds.

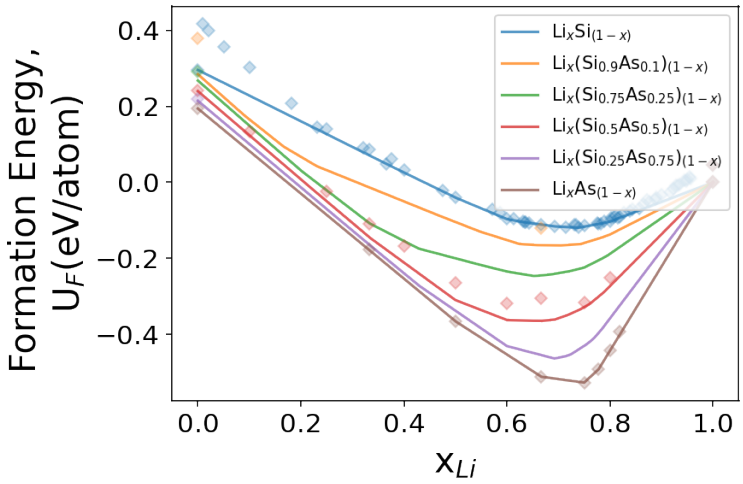

Figure A.26: Formation energy as a function of Li content for select compositions in the As-Li-Si chemical system. Lines represent cross-sectional planes of the amorphous hull. Calculated amorphous phases, coincident with the cross-sections, are marked with diamonds.

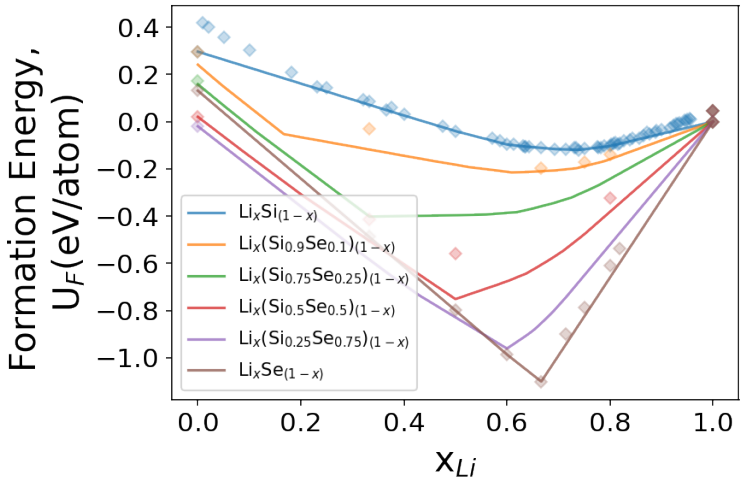

Figure A.27: Formation energy as a function of Li content for select compositions in the Li-Se-Si chemical system. Lines represent cross-sectional planes of the amorphous hull. Calculated amorphous phases, coincident with the cross-sections, are marked with diamonds.

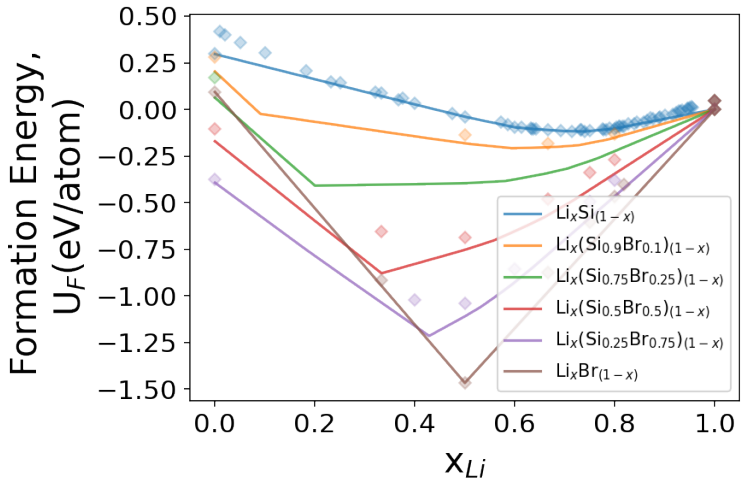

Figure A.28: Formation energy as a function of Li content for select compositions in the Br-Li-Si chemical system. Lines represent cross-sectional planes of the amorphous hull. Calculated amorphous phases, coincident with the cross-sections, are marked with diamonds.

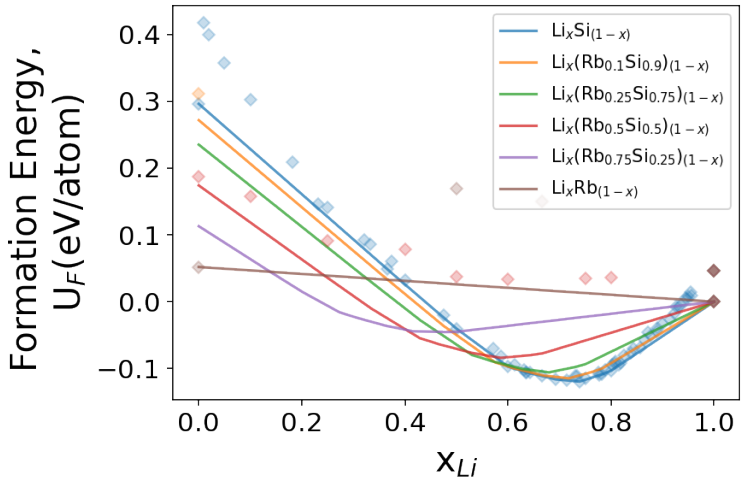

Figure A.29: Formation energy as a function of Li content for select compositions in the Li-Rb-Si chemical system. Lines represent cross-sectional planes of the amorphous hull. Calculated amorphous phases, coincident with the cross-sections, are marked with diamonds.

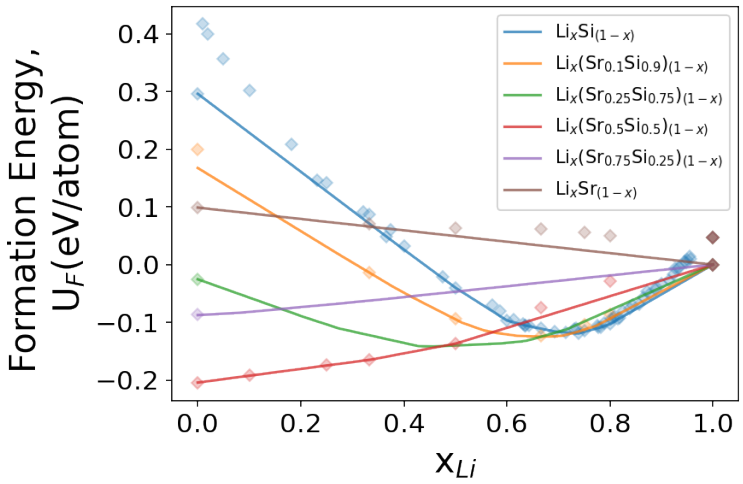

Figure A.30: Formation energy as a function of Li content for select compositions in the Li-Si-Sr chemical system. Lines represent cross-sectional planes of the amorphous hull. Calculated amorphous phases, coincident with the cross-sections, are marked with diamonds.

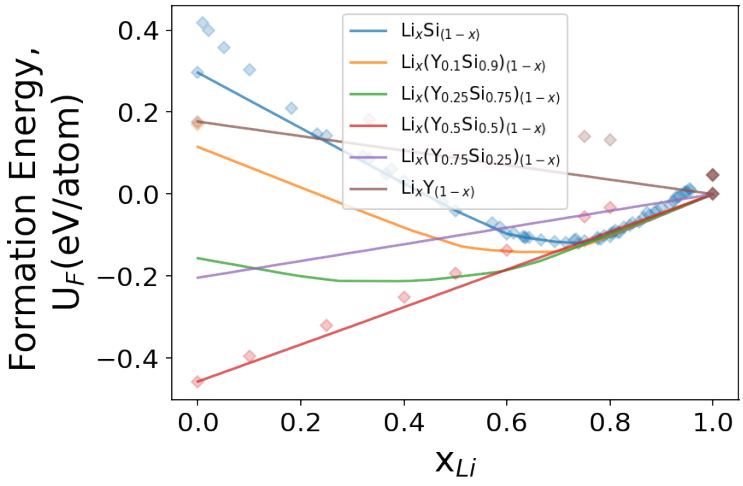

Figure A.31: Formation energy as a function of Li content for select compositions in the Li-Si-Y chemical system. Lines represent cross-sectional planes of the amorphous hull. Calculated amorphous phases, coincident with the cross-sections, are marked with diamonds.

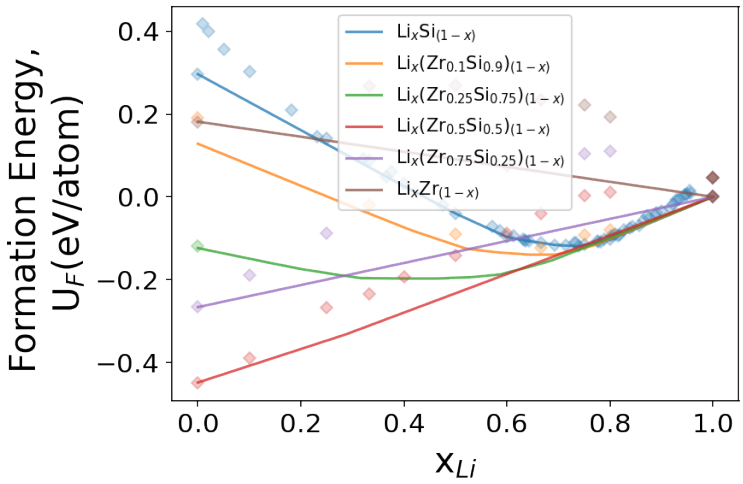

Figure A.32: Formation energy as a function of Li content for select compositions in the Li-Si-Zr chemical system. Lines represent cross-sectional planes of the amorphous hull. Calculated amorphous phases, coincident with the cross-sections, are marked with diamonds.

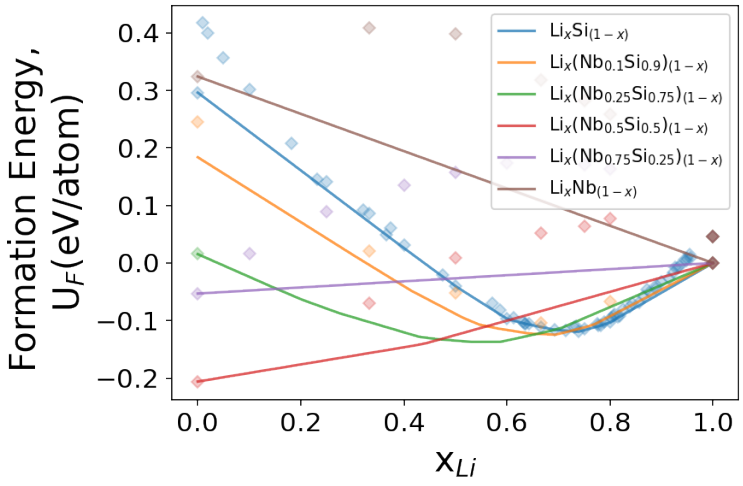

Figure A.33: Formation energy as a function of Li content for select compositions in the Li-Nb-Si chemical system. Lines represent cross-sectional planes of the amorphous hull. Calculated amorphous phases, coincident with the cross-sections, are marked with diamonds.

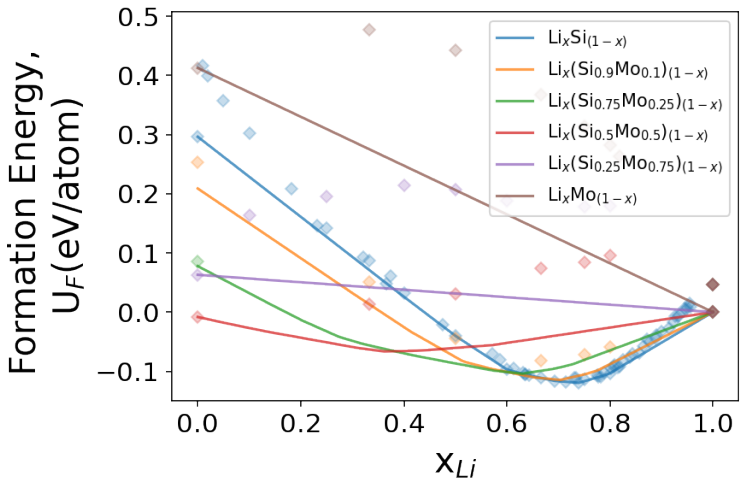

Figure A.34: Formation energy as a function of Li content for select compositions in the Li-Mo-Si chemical system. Lines represent cross-sectional planes of the amorphous hull. Calculated amorphous phases, coincident with the cross-sections, are marked with diamonds.

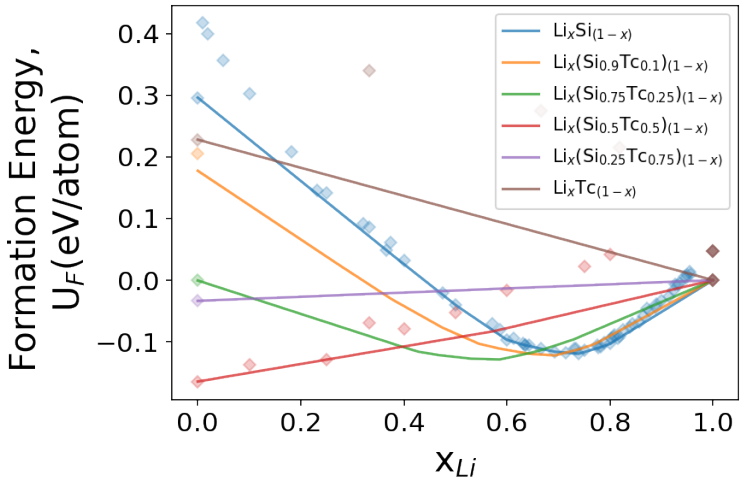

Figure A.35: Formation energy as a function of Li content for select compositions in the Li-Si-Tc chemical system. Lines represent cross-sectional planes of the amorphous hull. Calculated amorphous phases, coincident with the cross-sections, are marked with diamonds.

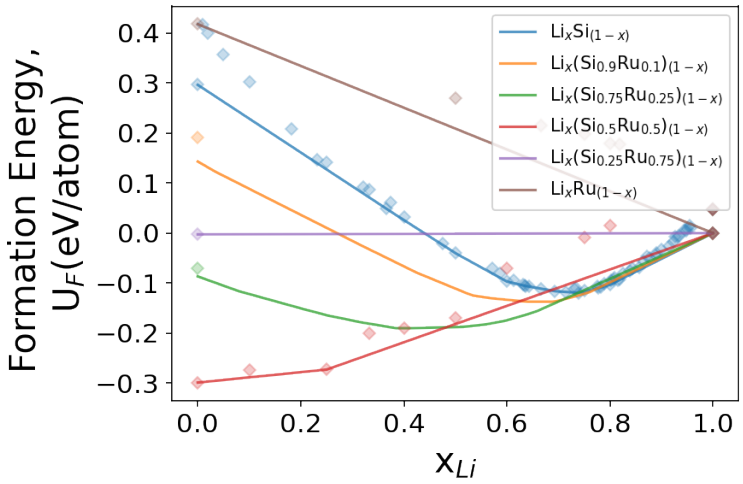

Figure A.36: Formation energy as a function of Li content for select compositions in the Li-Ru-Si chemical system. Lines represent cross-sectional planes of the amorphous hull. Calculated amorphous phases, coincident with the cross-sections, are marked with diamonds.

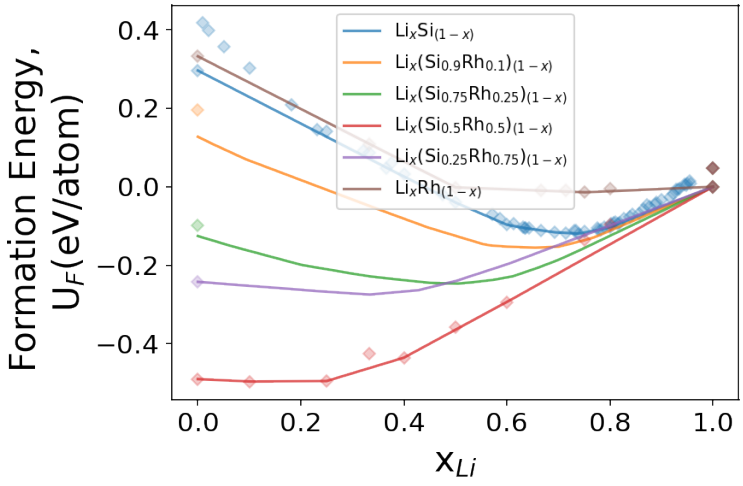

Figure A.37: Formation energy as a function of Li content for select compositions in the Li-Rh-Si chemical system. Lines represent cross-sectional planes of the amorphous hull. Calculated amorphous phases, coincident with the cross-sections, are marked with diamonds.

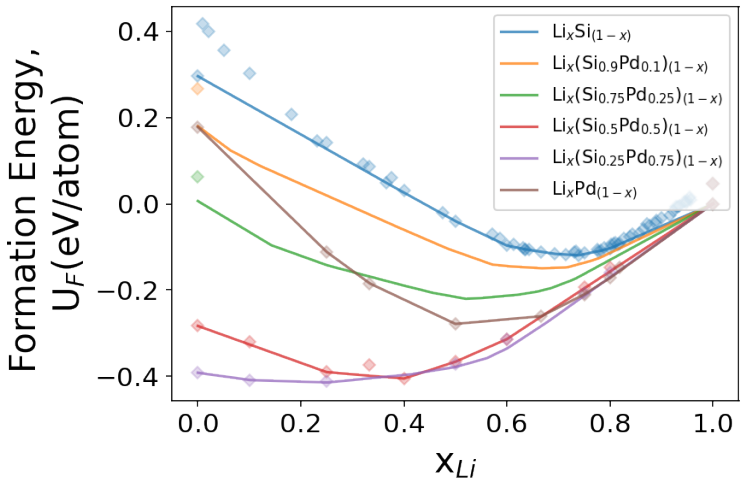

Figure A.38: Formation energy as a function of Li content for select compositions in the Li-Pd-Si chemical system. Lines represent cross-sectional planes of the amorphous hull. Calculated amorphous phases, coincident with the cross-sections, are marked with diamonds.

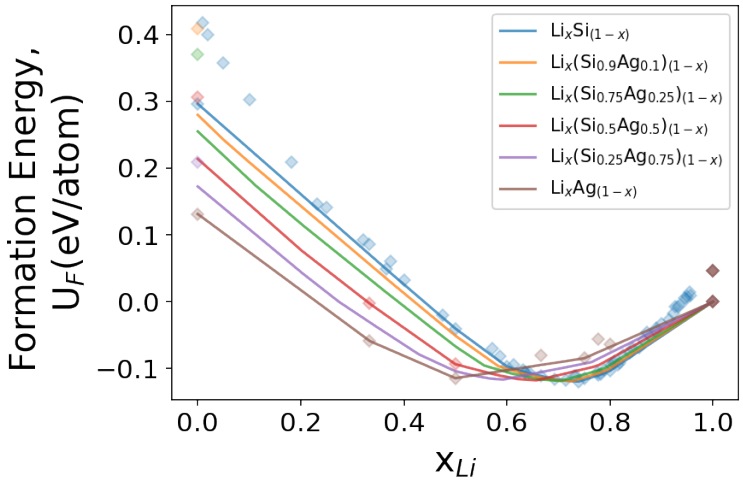

Figure A.39: Formation energy as a function of Li content for select compositions in the Ag-Li-Si chemical system. Lines represent cross-sectional planes of the amorphous hull. Calculated amorphous phases, coincident with the cross-sections, are marked with diamonds.

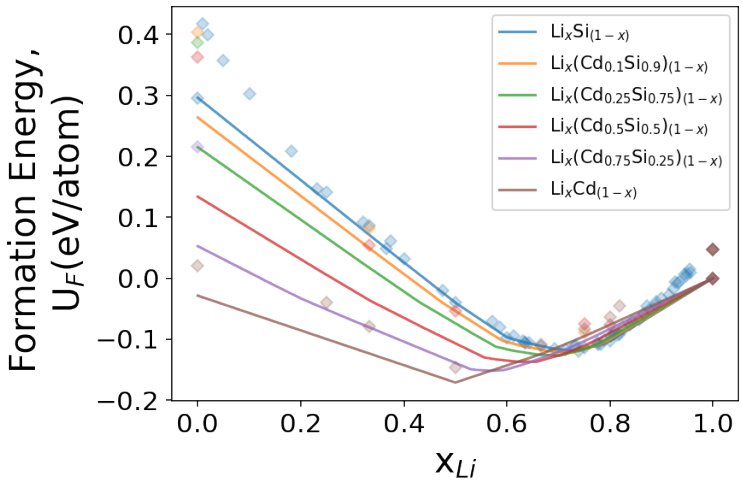

Figure A.40: Formation energy as a function of Li content for select compositions in the Cd-Li-Si chemical system. Lines represent cross-sectional planes of the amorphous hull. Calculated amorphous phases, coincident with the cross-sections, are marked with diamonds.

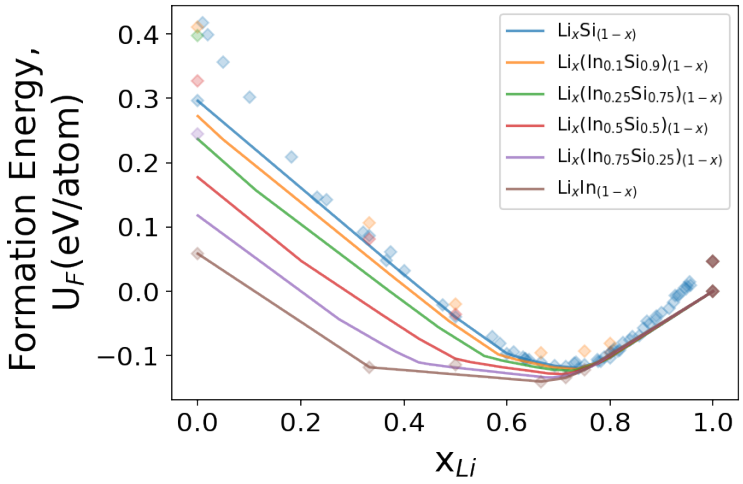

Figure A.41: Formation energy as a function of Li content for select compositions in the In-Li-Si chemical system. Lines represent cross-sectional planes of the amorphous hull. Calculated amorphous phases, coincident with the cross-sections, are marked with diamonds.

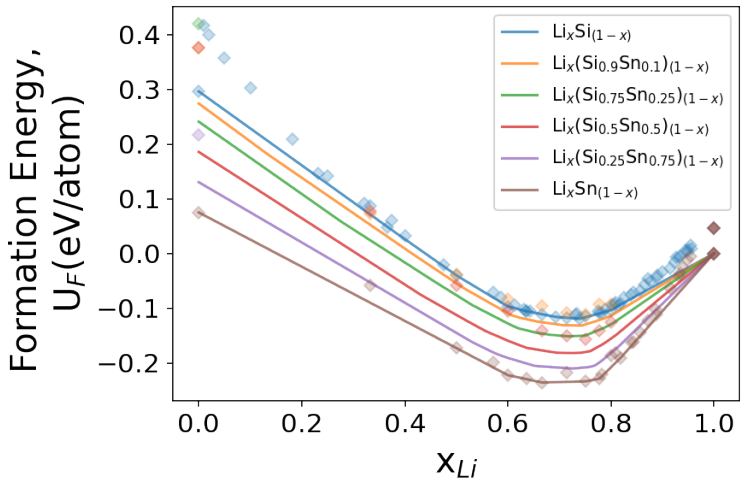

Figure A.42: Formation energy as a function of Li content for select compositions in the Li-Si-Sn chemical system. Lines represent cross-sectional planes of the amorphous hull. Calculated amorphous phases, coincident with the cross-sections, are marked with diamonds.

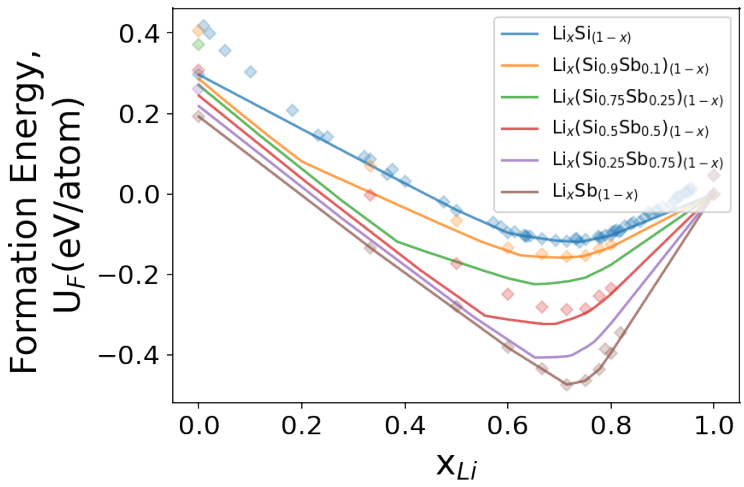

Figure A.43: Formation energy as a function of Li content for select compositions in the Li-Sb-Si chemical system. Lines represent cross-sectional planes of the amorphous hull. Calculated amorphous phases, coincident with the cross-sections, are marked with diamonds.

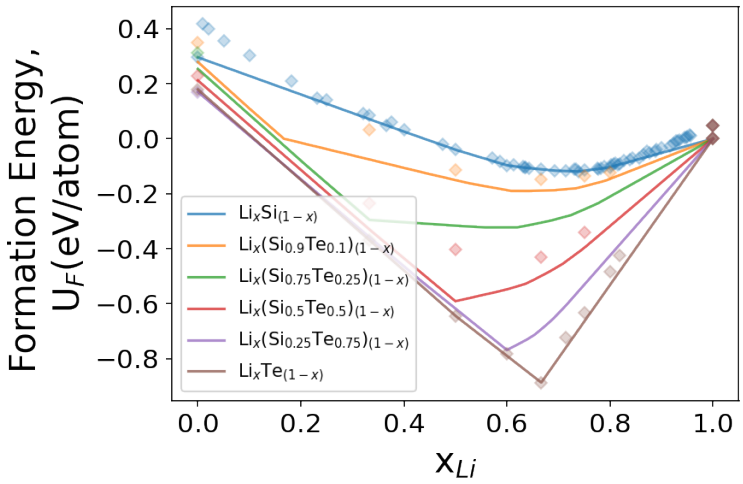

Figure A.44: Formation energy as a function of Li content for select compositions in the Li-Si-Te chemical system. Lines represent cross-sectional planes of the amorphous hull. Calculated amorphous phases, coincident with the cross-sections, are marked with diamonds.

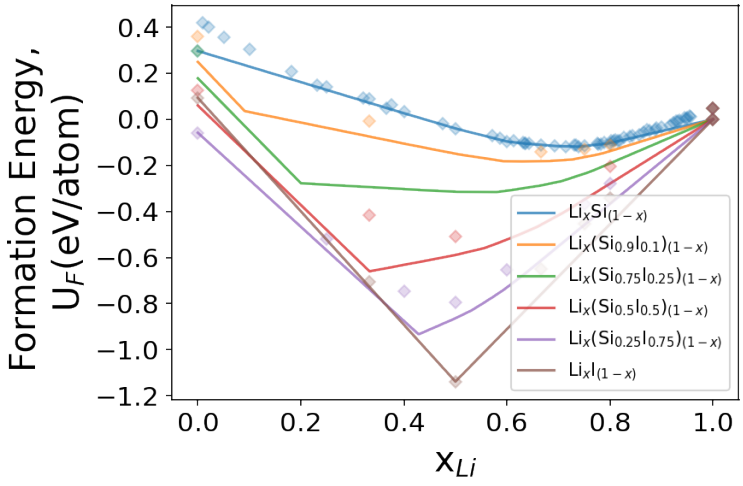

Figure A.45: Formation energy as a function of Li content for select compositions in the I-Li-Si chemical system. Lines represent cross-sectional planes of the amorphous hull. Calculated amorphous phases, coincident with the cross-sections, are marked with diamonds.

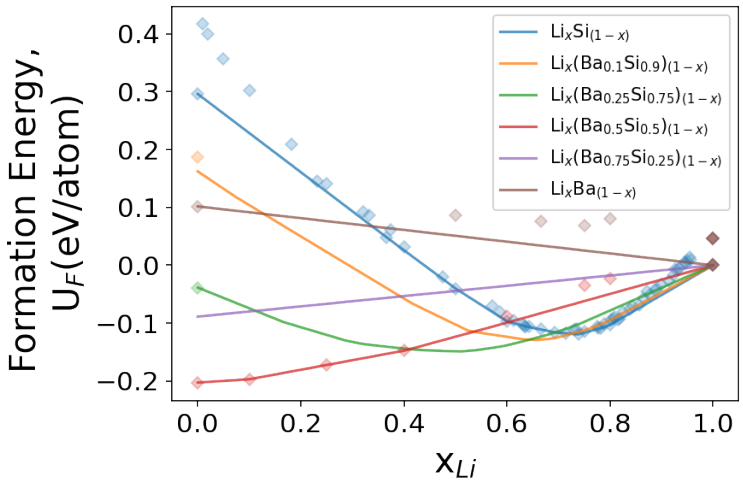

Figure A.46: Formation energy as a function of Li content for select compositions in the Ba-Li-Si chemical system. Lines represent cross-sectional planes of the amorphous hull. Calculated amorphous phases, coincident with the cross-sections, are marked with diamonds.

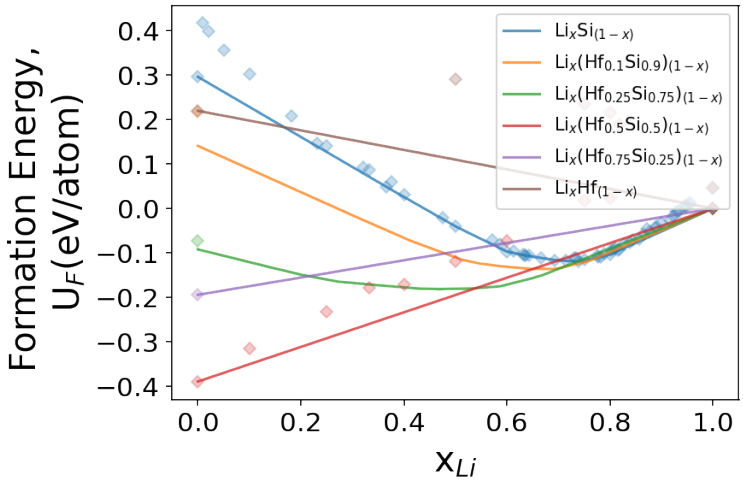

Figure A.47: Formation energy as a function of Li content for select compositions in the Hf-Li-Si chemical system. Lines represent cross-sectional planes of the amorphous hull. Calculated amorphous phases, coincident with the cross-sections, are marked with diamonds.

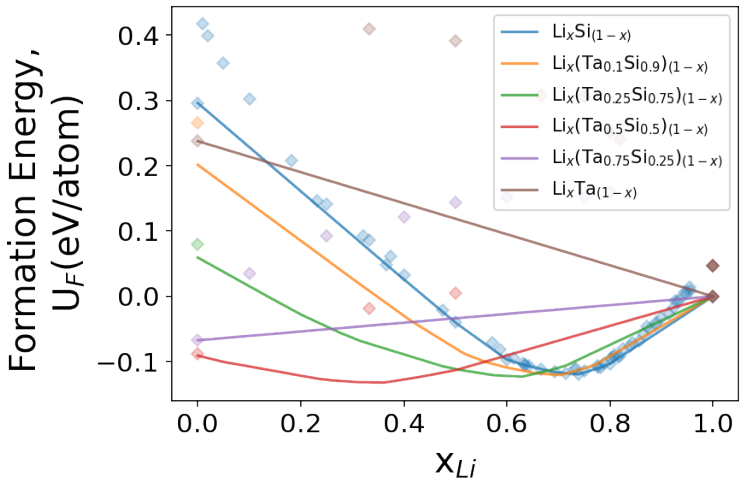

Figure A.48: Formation energy as a function of Li content for select compositions in the Li-Si-Ta chemical system. Lines represent cross-sectional planes of the amorphous hull. Calculated amorphous phases, coincident with the cross-sections, are marked with diamonds.

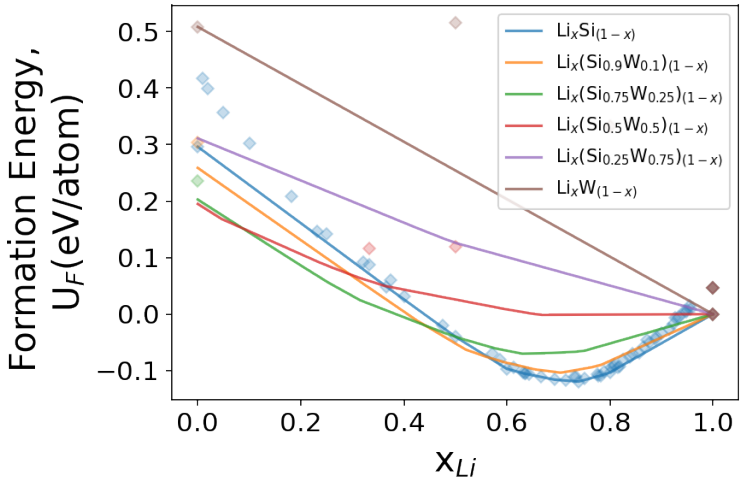

Figure A.49: Formation energy as a function of Li content for select compositions in the Li-Si-W chemical system. Lines represent cross-sectional planes of the amorphous hull. Calculated amorphous phases, coincident with the cross-sections, are marked with diamonds.

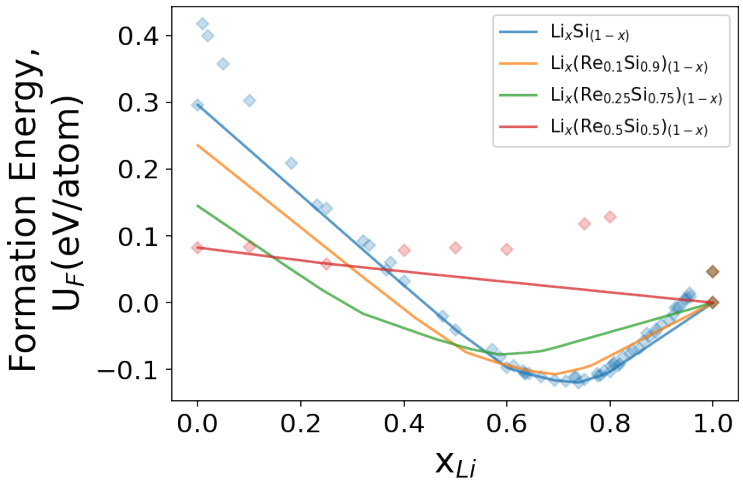

Figure A.50: Formation energy as a function of Li content for select compositions in the Li-Re-Si chemical system. Lines represent cross-sectional planes of the amorphous hull. Calculated amorphous phases, coincident with the cross-sections, are marked with diamonds.

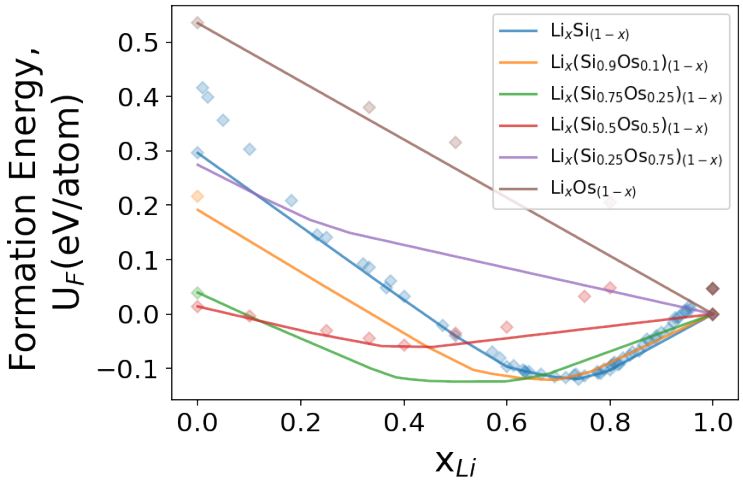

Figure A.51: Formation energy as a function of Li content for select compositions in the Li-Os-Si chemical system. Lines represent cross-sectional planes of the amorphous hull. Calculated amorphous phases, coincident with the cross-sections, are marked with diamonds.

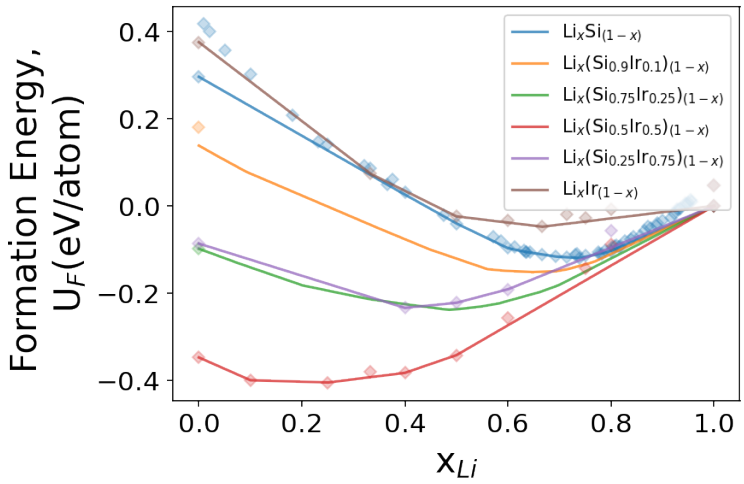

Figure A.52: Formation energy as a function of Li content for select compositions in the Ir-Li-Si chemical system. Lines represent cross-sectional planes of the amorphous hull. Calculated amorphous phases, coincident with the cross-sections, are marked with diamonds.

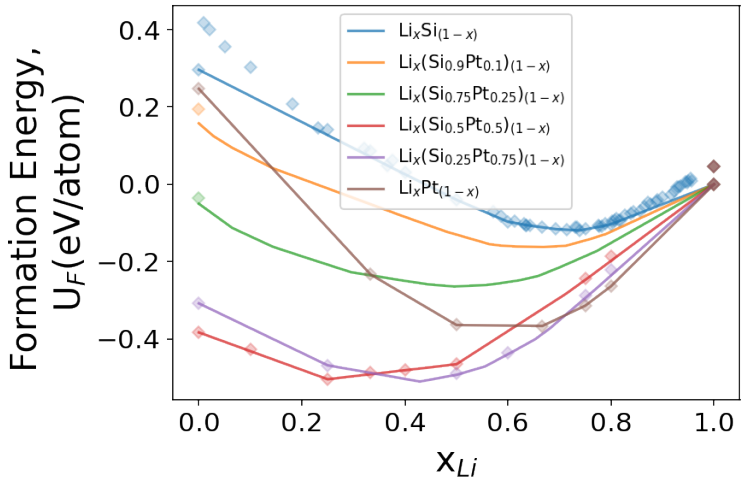

Figure A.53: Formation energy as a function of Li content for select compositions in the Li-Pt-Si chemical system. Lines represent cross-sectional planes of the amorphous hull. Calculated amorphous phases, coincident with the cross-sections, are marked with diamonds.

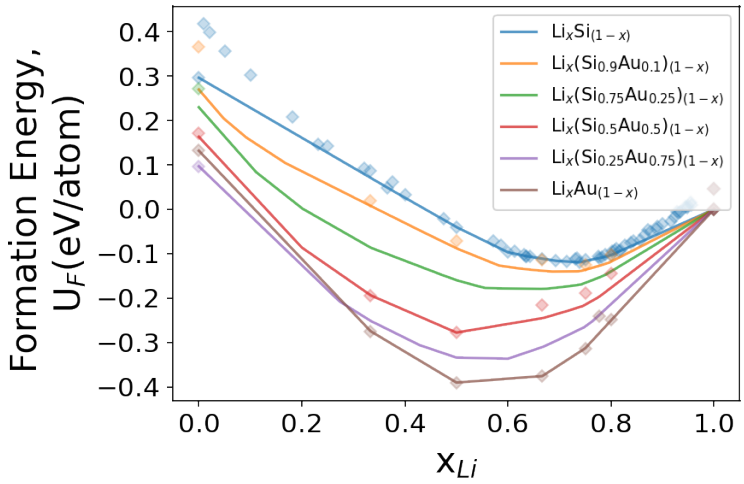

Figure A.54: Formation energy as a function of Li content for select compositions in the Au-Li-Si chemical system. Lines represent cross-sectional planes of the amorphous hull. Calculated amorphous phases, coincident with the cross-sections, are marked with diamonds.

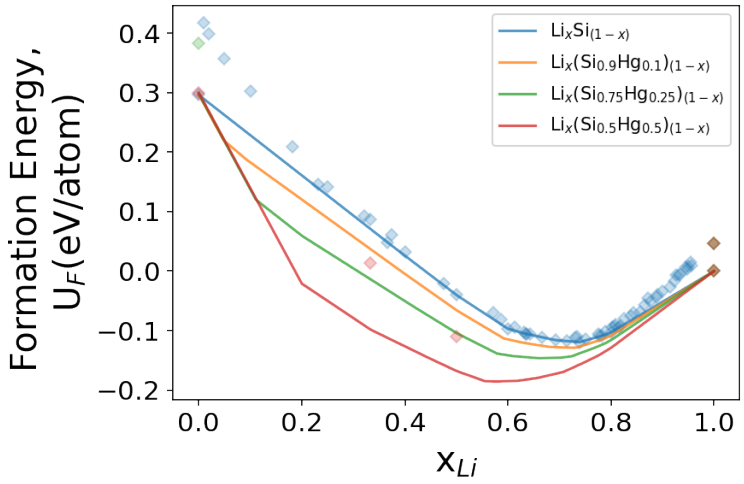

Figure A.55: Formation energy as a function of Li content for select compositions in the Hg-Li-Si chemical system. Lines represent cross-sectional planes of the amorphous hull. Calculated amorphous phases, coincident with the cross-sections, are marked with diamonds.

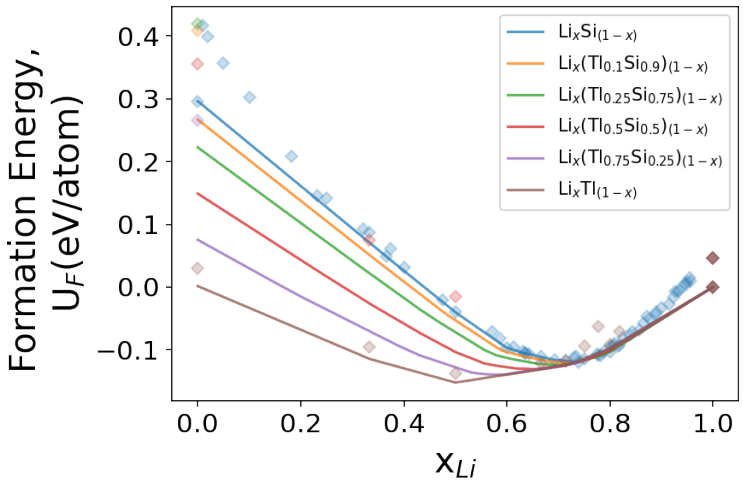

Figure A.56: Formation energy as a function of Li content for select compositions in the Li-Si-Tl chemical system. Lines represent cross-sectional planes of the amorphous hull. Calculated amorphous phases, coincident with the cross-sections, are marked with diamonds.

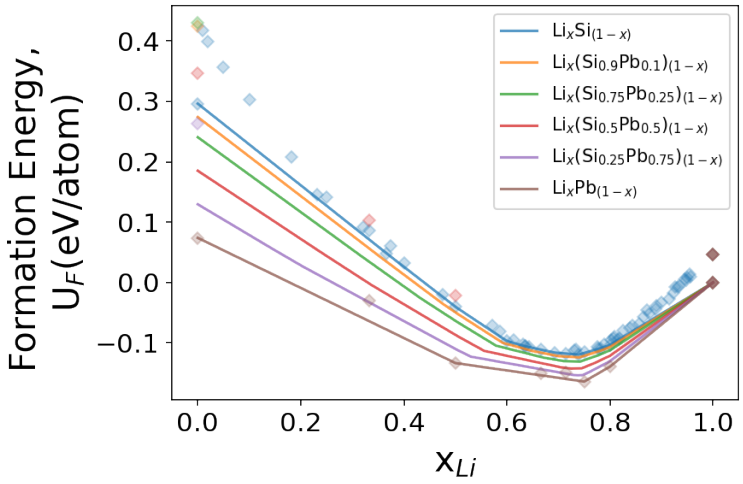

Figure A.57: Formation energy as a function of Li content for select compositions in the Li-Pb-Si chemical system. Lines represent cross-sectional planes of the amorphous hull. Calculated amorphous phases, coincident with the cross-sections, are marked with diamonds.

A.2 Equilibrium Lithiation potentials for Si-X alloys

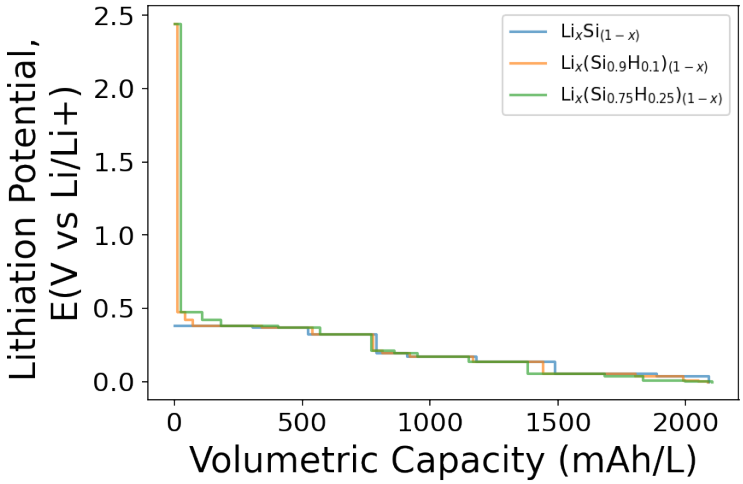

Figure A.59: Lithiation voltages for select compositions in the H-Li-Si chemical system.

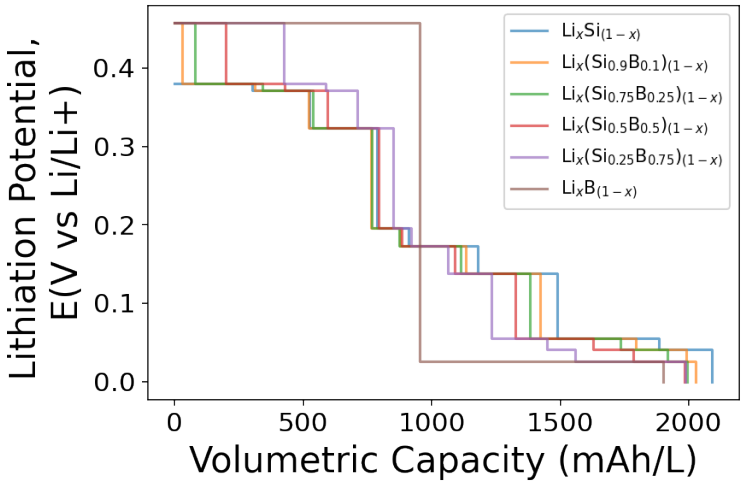

Figure A.60: Lithiation voltages for select compositions in the B-Li-Si chemical system.

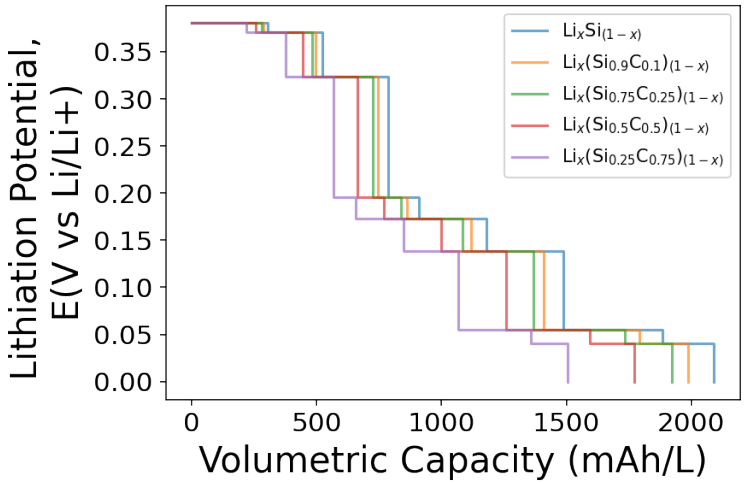

Figure A.61: Lithiation voltages for select compositions in the C-Li-Si chemical system.

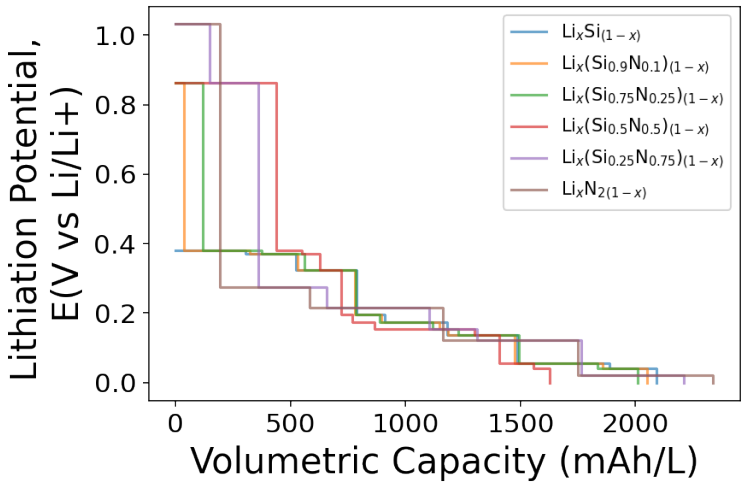

Figure A.62: Lithiation voltages for select compositions in the Li-N-Si chemical system.

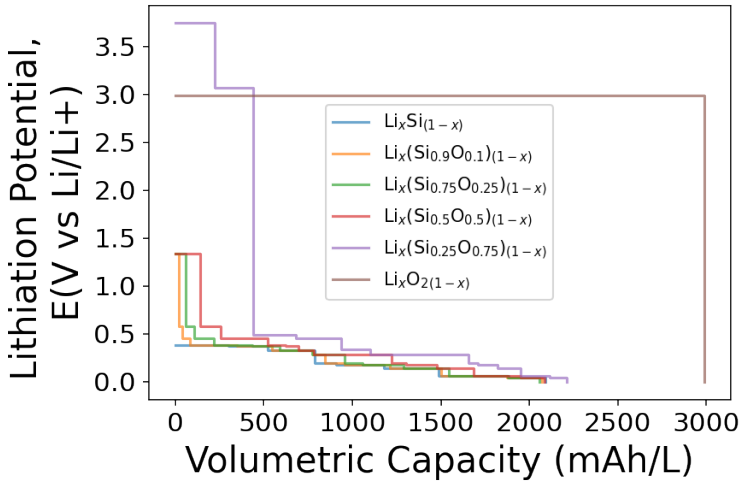

Figure A.63: Lithiation voltages for select compositions in the Li-O-Si chemical system.

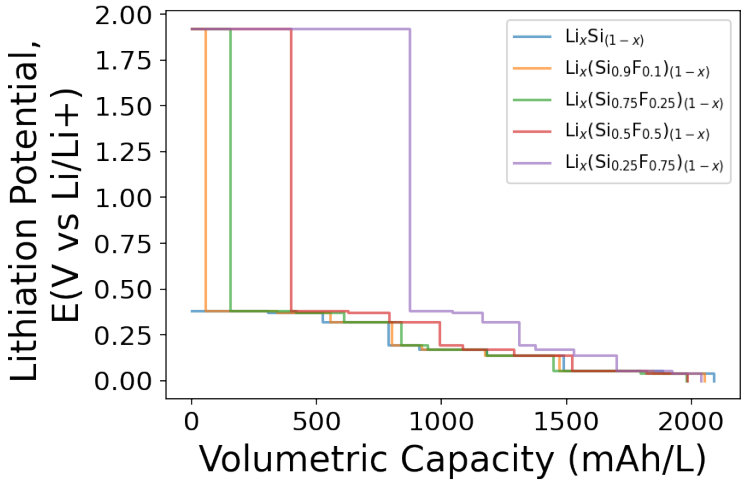

Figure A.64: Lithiation voltages for select compositions in the F-Li-Si chemical system.

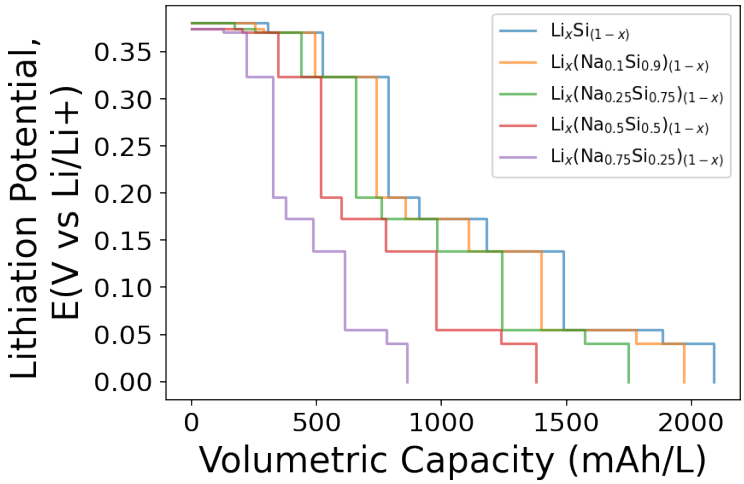

Figure A.65: Lithiation voltages for select compositions in the Li-Na-Si chemical system.

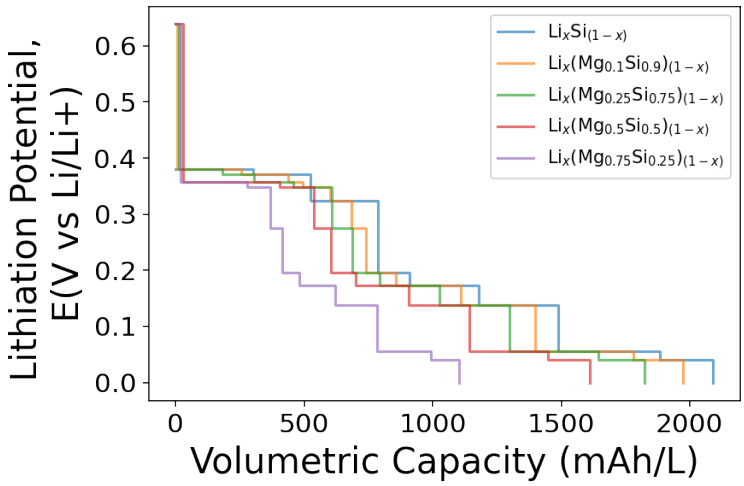

Figure A.66: Lithiation voltages for select compositions in the Li-Mg-Si chemical system.

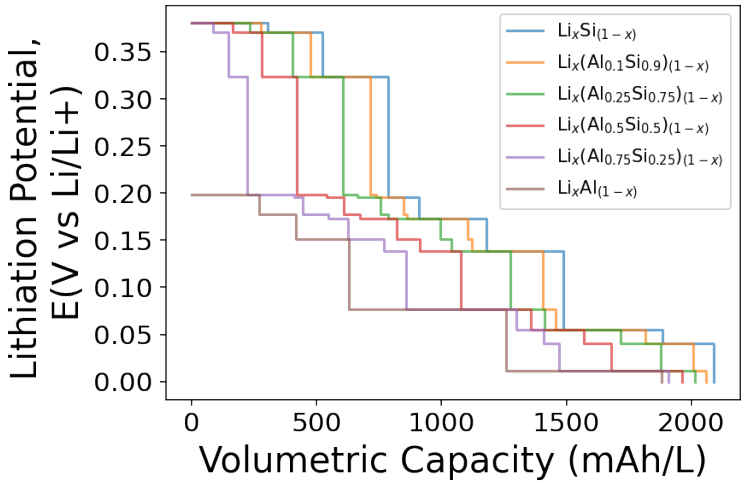

Figure A.67: Lithiation voltages for select compositions in the Al-Li-Si chemical system.

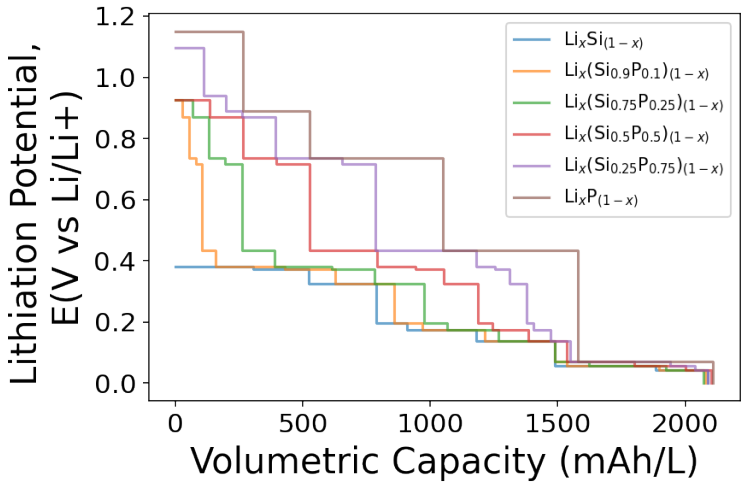

Figure A.68: Lithiation voltages for select compositions in the Li-P-Si chemical system.

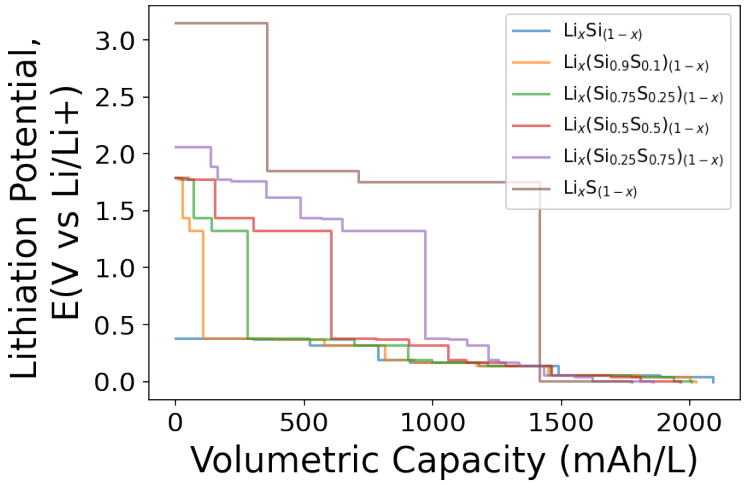

Figure A.69: Lithiation voltages for select compositions in the Li-S-Si chemical system.

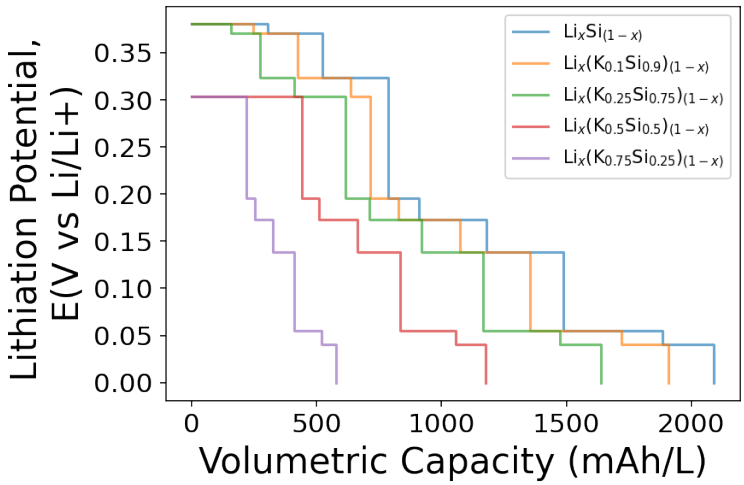

Figure A.70: Lithiation voltages for select compositions in the K-Li-Si chemical system.

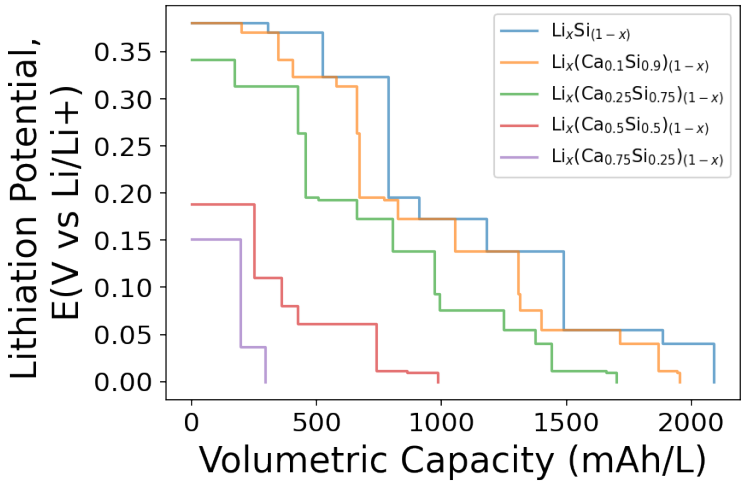

Figure A.71: Lithiation voltages for select compositions in the Ca-Li-Si chemical system.

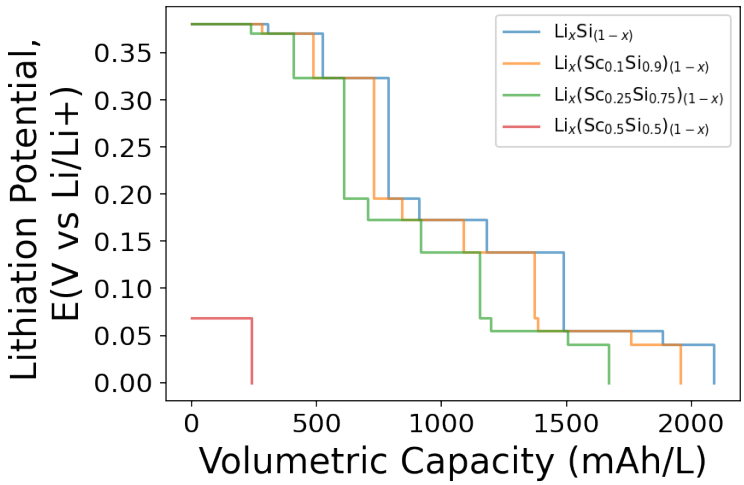

Figure A.72: Lithiation voltages for select compositions in the Li-Sc-Si chemical system.

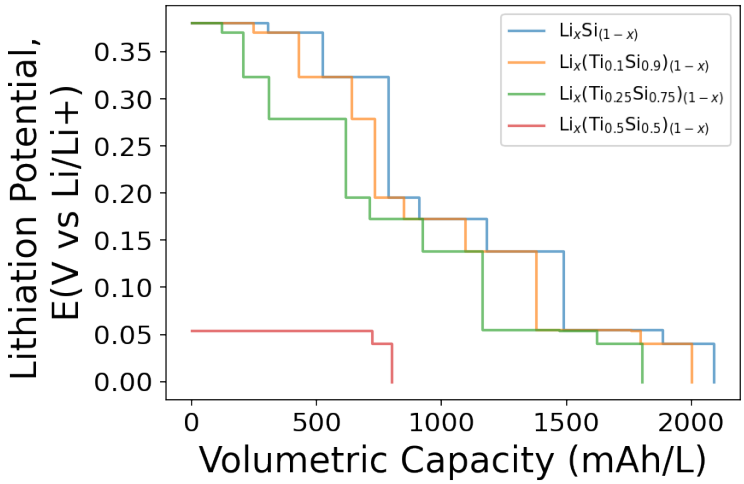

Figure A.73: Lithiation voltages for select compositions in the Li-Si-Ti chemical system.

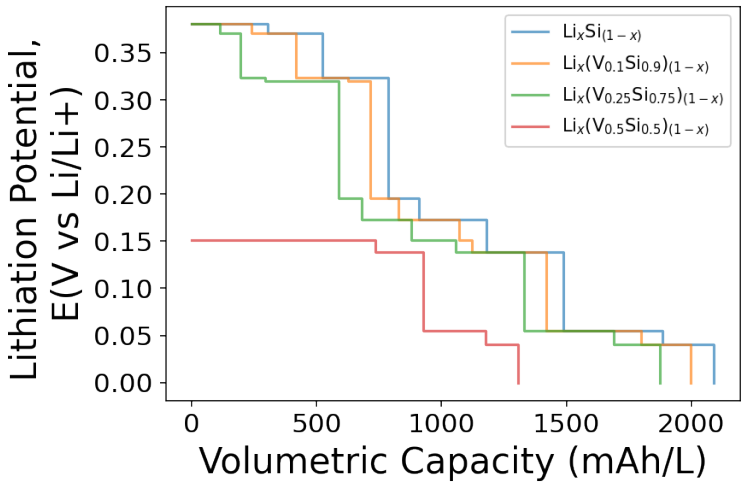

Figure A.74: Lithiation voltages for select compositions in the Li-Si-V chemical system.

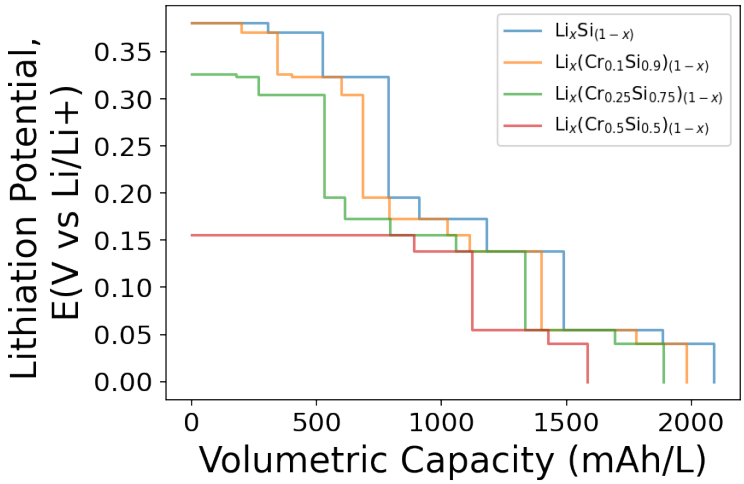

Figure A.75: Lithiation voltages for select compositions in the Cr-Li-Si chemical system.

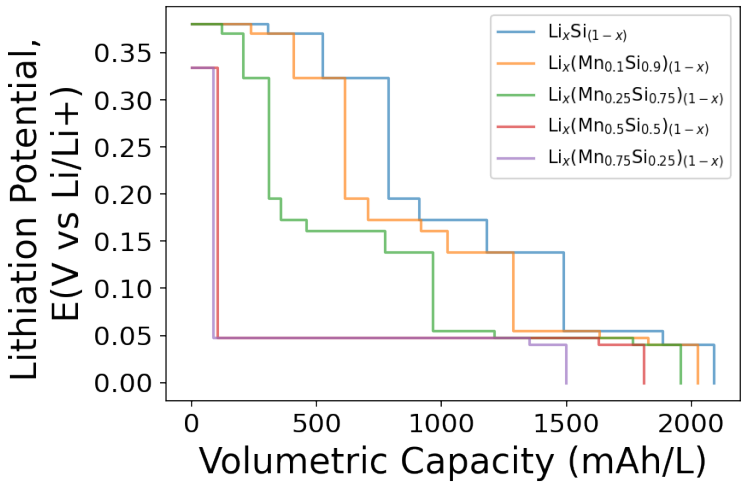

Figure A.76: Lithiation voltages for select compositions in the Li-Mn-Si chemical system.

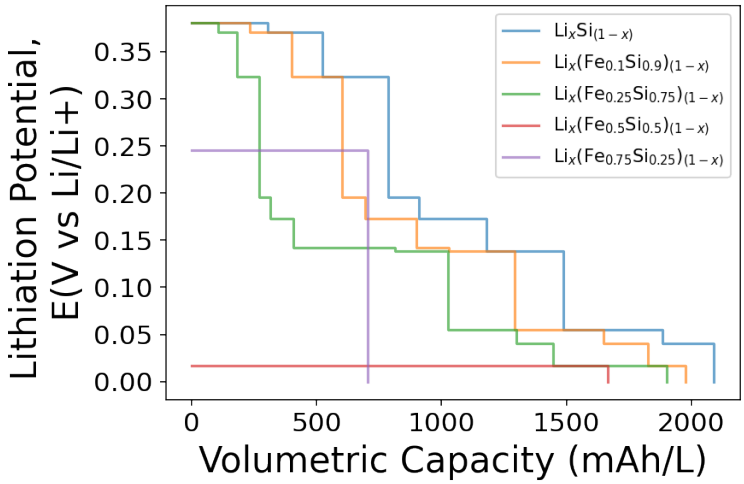

Figure A.77: Lithiation voltages for select compositions in the Fe-Li-Si chemical system.

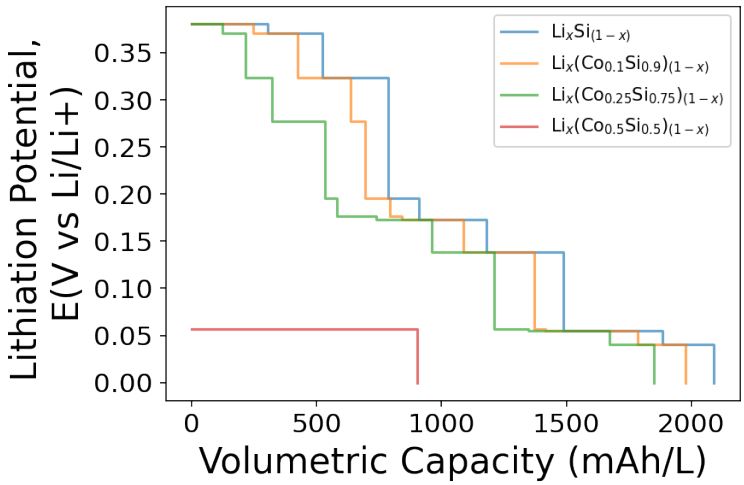

Figure A.78: Lithiation voltages for select compositions in the Co-Li-Si chemical system.

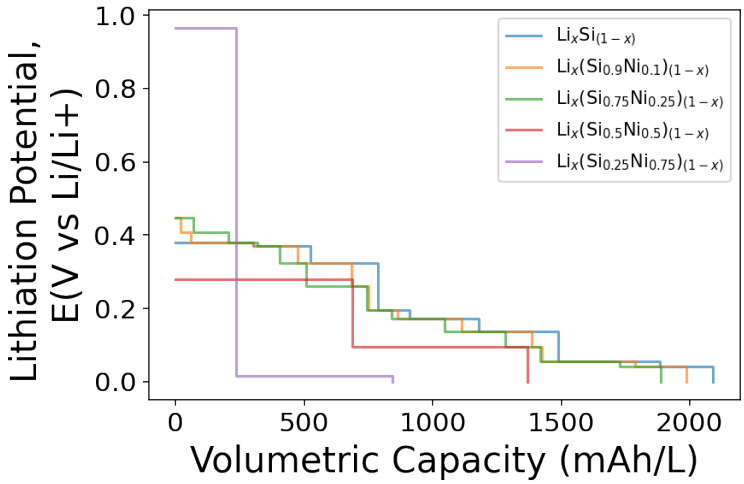

Figure A.79: Lithiation voltages for select compositions in the Li-Ni-Si chemical system.

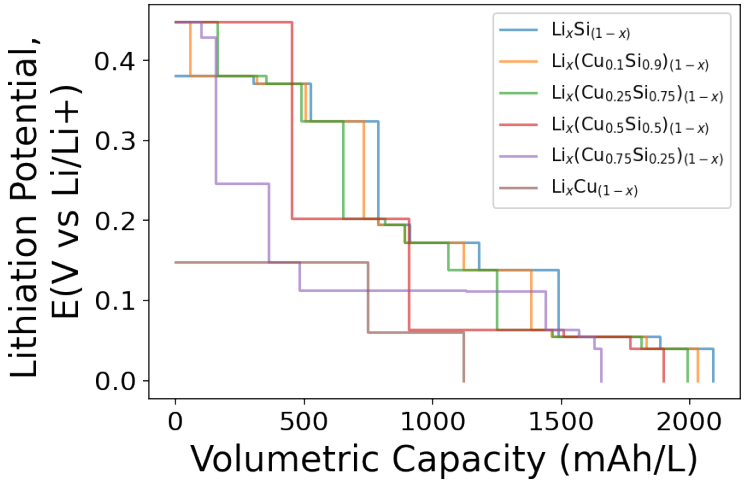

Figure A.80: Lithiation voltages for select compositions in the Cu-Li-Si chemical system.

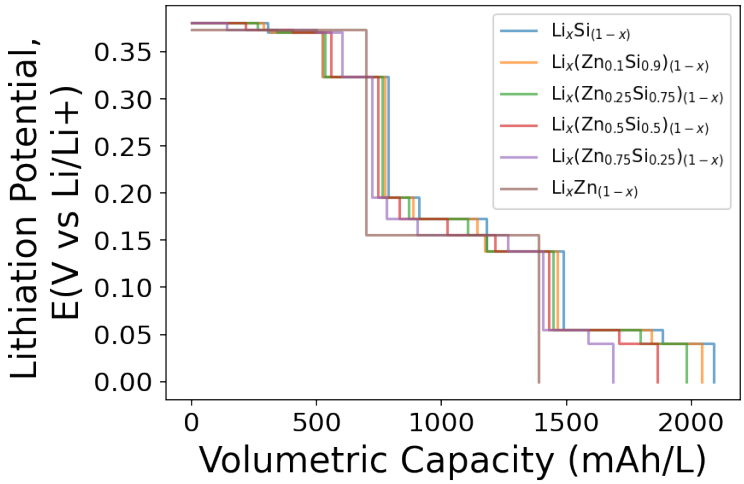

Figure A.81: Lithiation voltages for select compositions in the Li-Si-Zn chemical system.

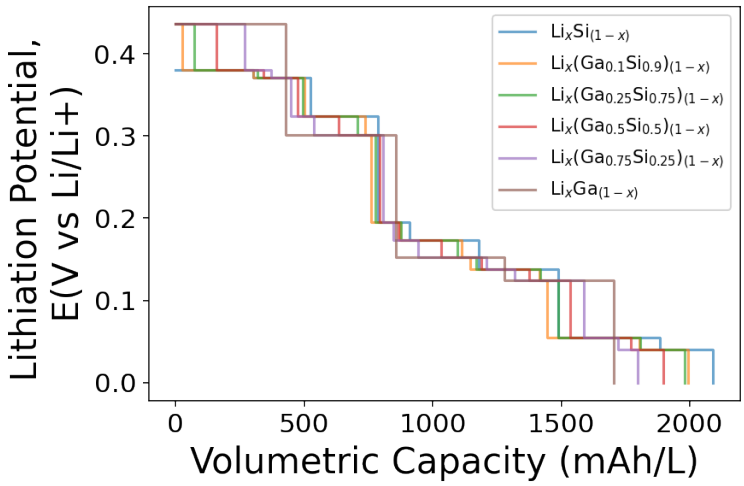

Figure A.82: Lithiation voltages for select compositions in the Ga-Li-Si chemical system.

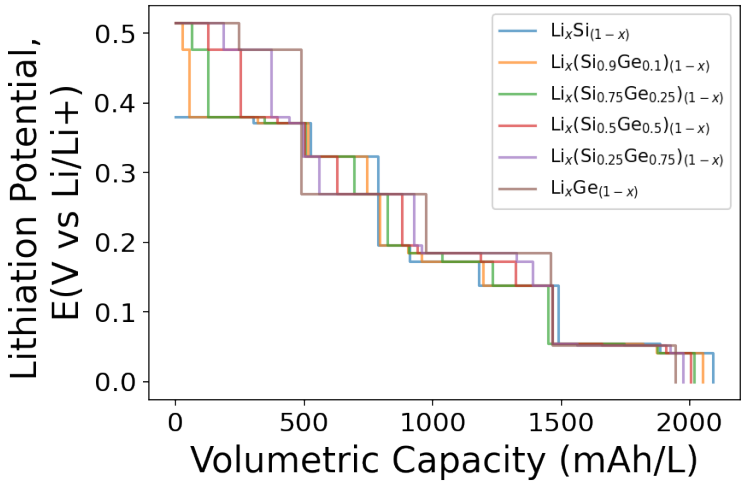

Figure A.83: Lithiation voltages for select compositions in the Ge-Li-Si chemical system.

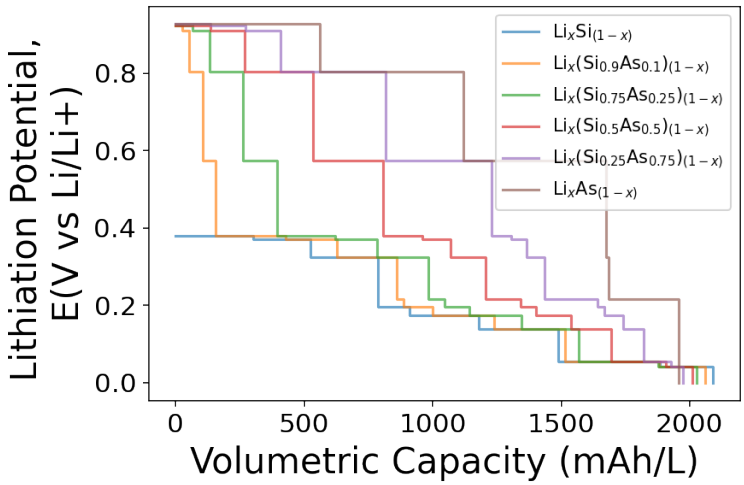

Figure A.84: Lithiation voltages for select compositions in the As-Li-Si chemical system.

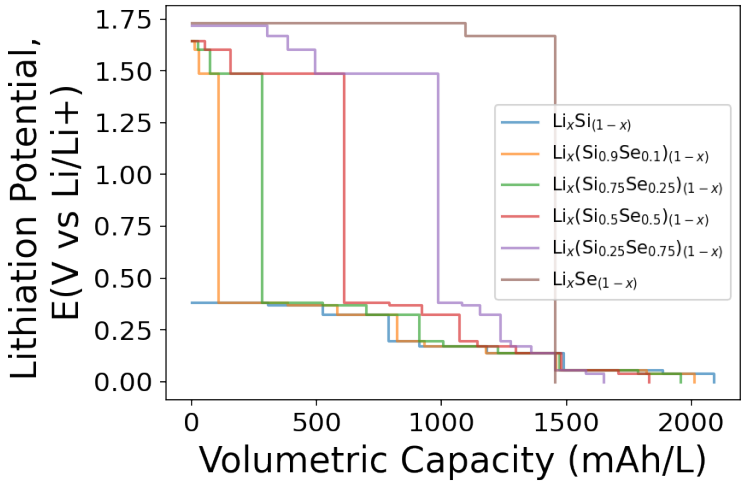

Figure A.85: Lithiation voltages for select compositions in the Li-Se-Si chemical system.

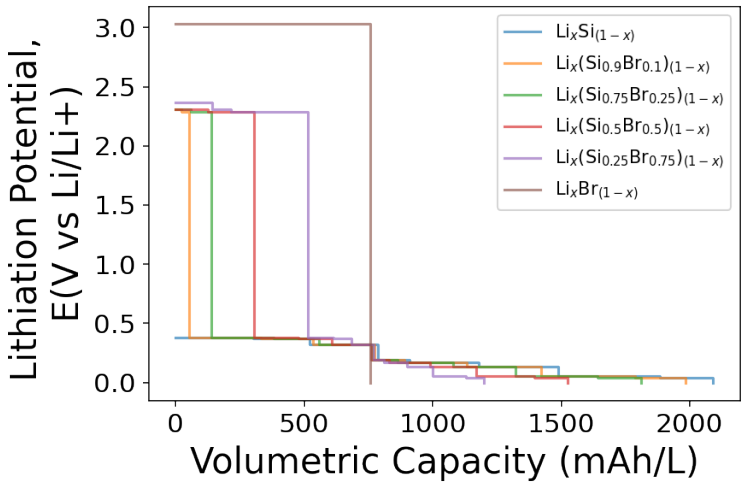

Figure A.86: Lithiation voltages for select compositions in the Br-Li-Si chemical system.

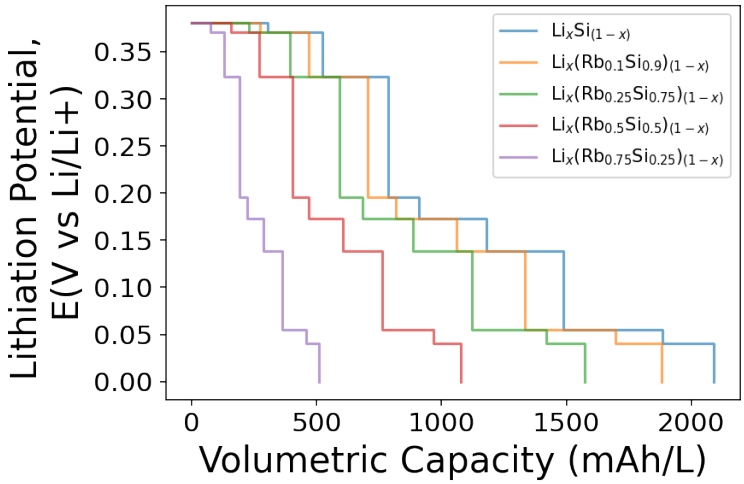

Figure A.87: Lithiation voltages for select compositions in the Li-Rb-Si chemical system.

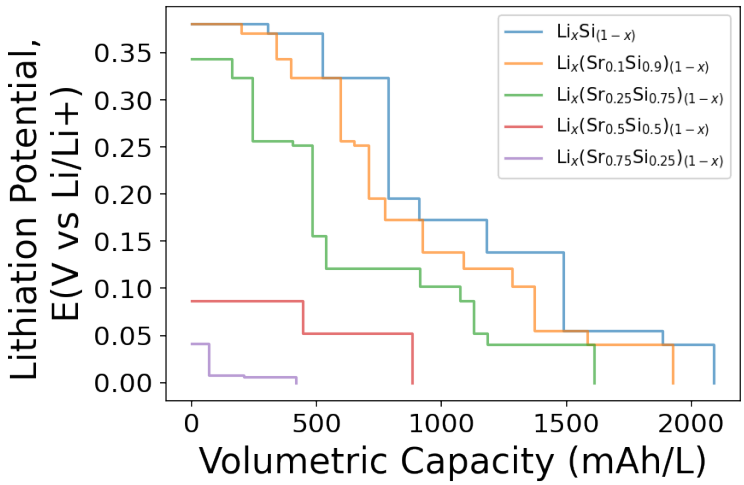

Figure A.88: Lithiation voltages for select compositions in the Li-Si-Sr chemical system.

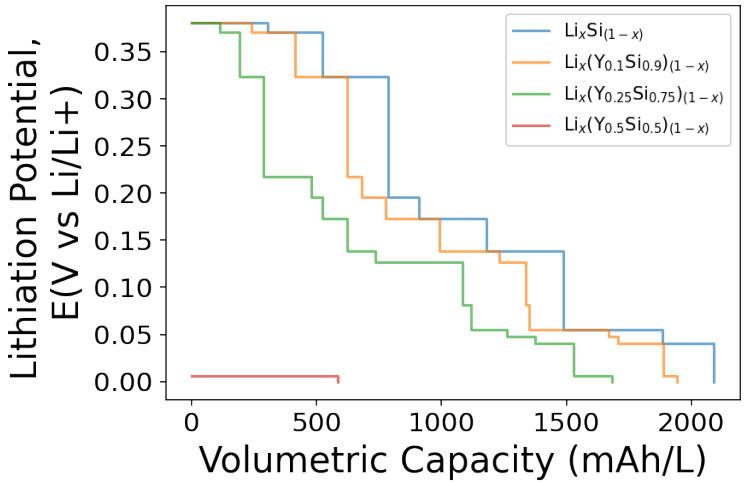

Figure A.89: Lithiation voltages for select compositions in the Li-Si-Y chemical system.

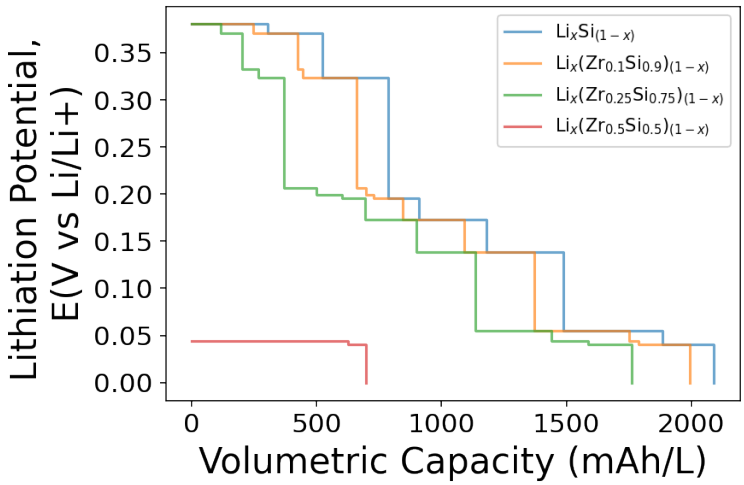

Figure A.90: Lithiation voltages for select compositions in the Li-Si-Zr chemical system.

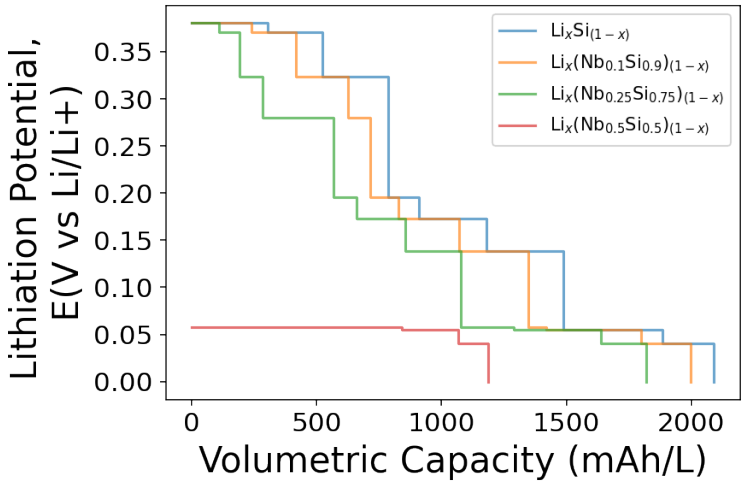

Figure A.91: Lithiation voltages for select compositions in the Li-Nb-Si chemical system.

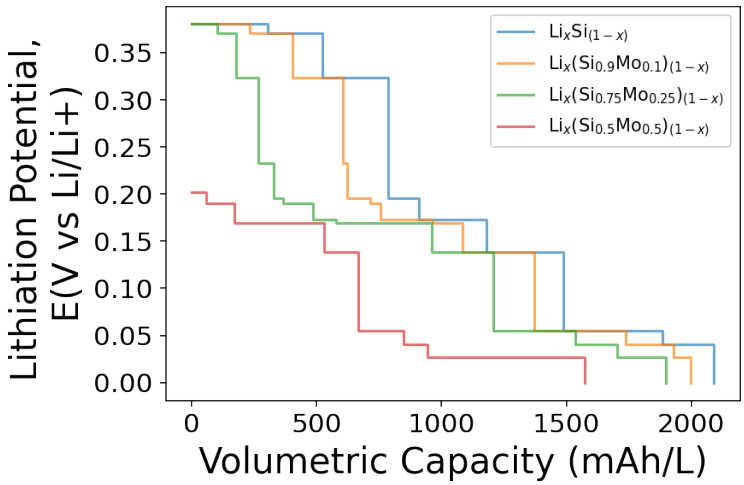

Figure A.92: Lithiation voltages for select compositions in the Li-Mo-Si chemical system.

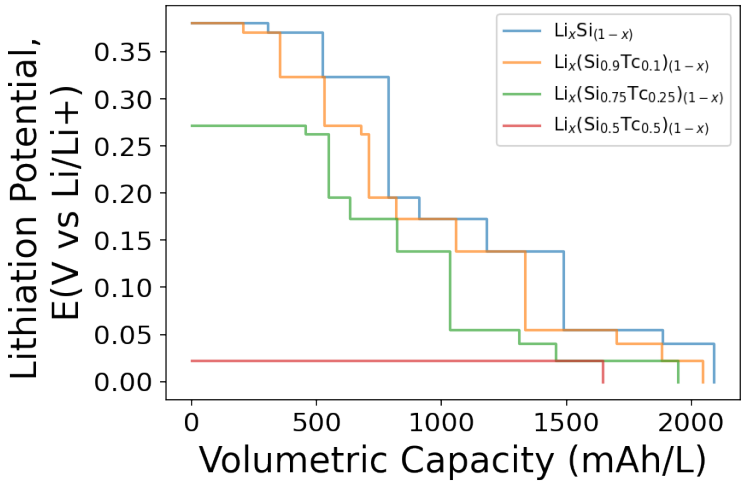

Figure A.93: Lithiation voltages for select compositions in the Li-Si-Tc chemical system.

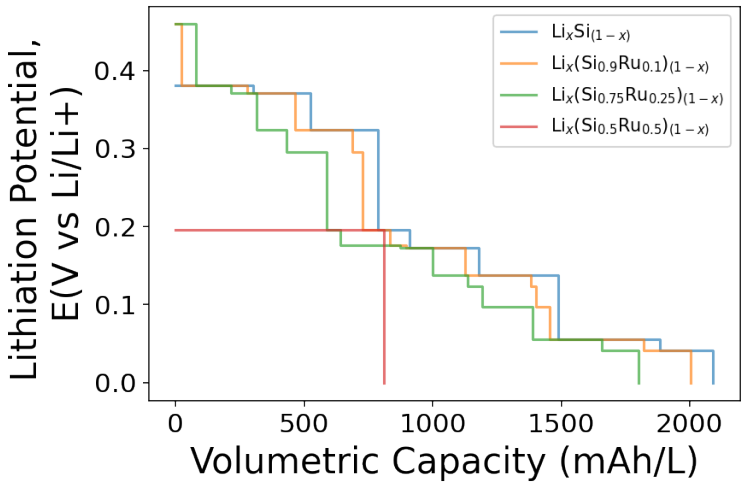

Figure A.94: Lithiation voltages for select compositions in the Li-Ru-Si chemical system.

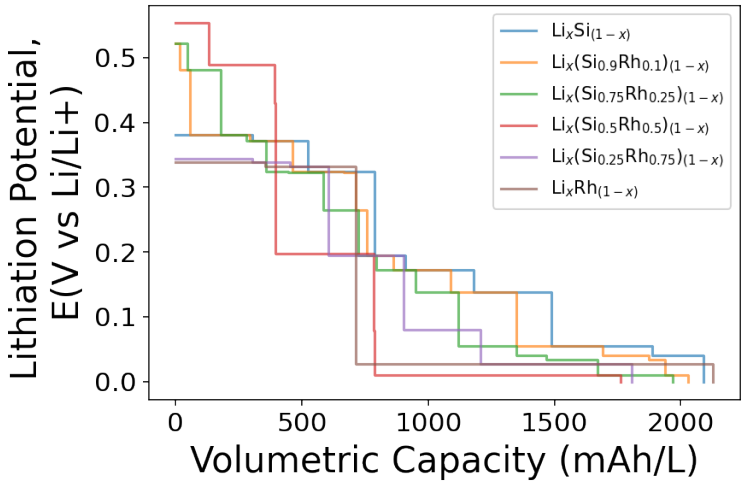

Figure A.95: Lithiation voltages for select compositions in the Li-Rh-Si chemical system.

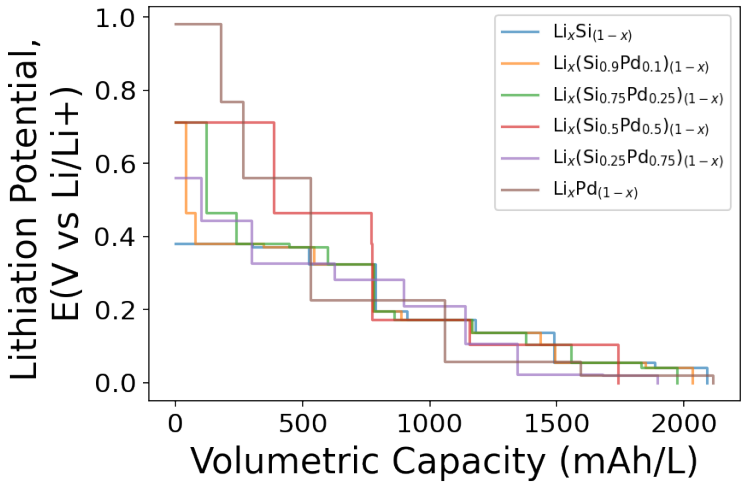

Figure A.96: Lithiation voltages for select compositions in the Li-Pd-Si chemical system.

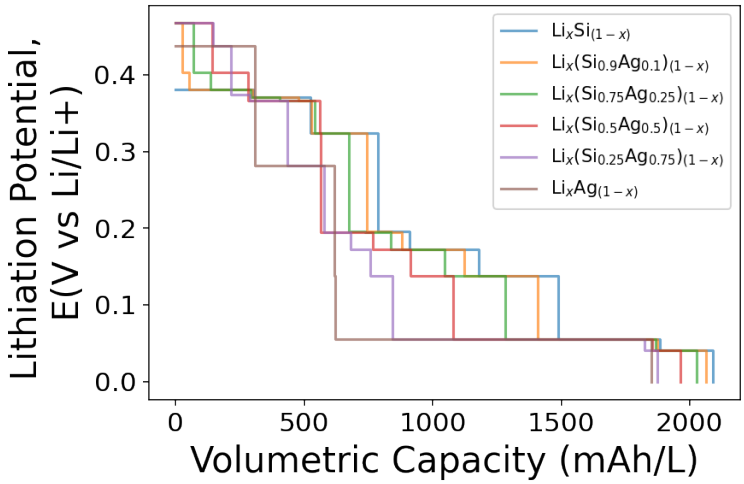

Figure A.97: Lithiation voltages for select compositions in the Ag-Li-Si chemical system.

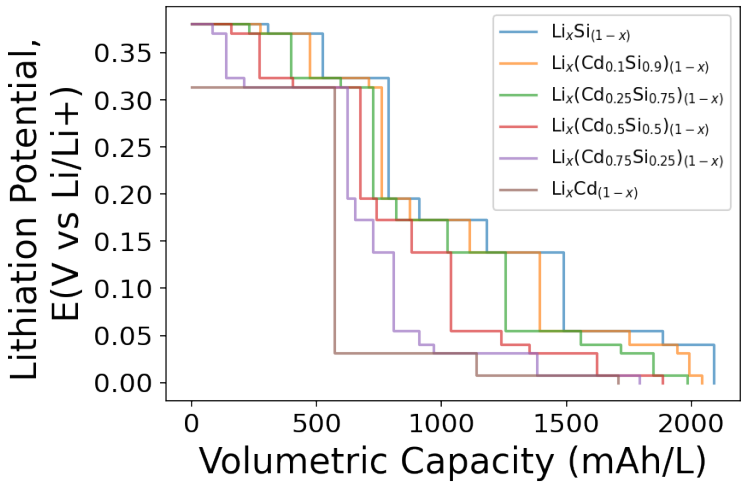

Figure A.98: Lithiation voltages for select compositions in the Cd-Li-Si chemical system.

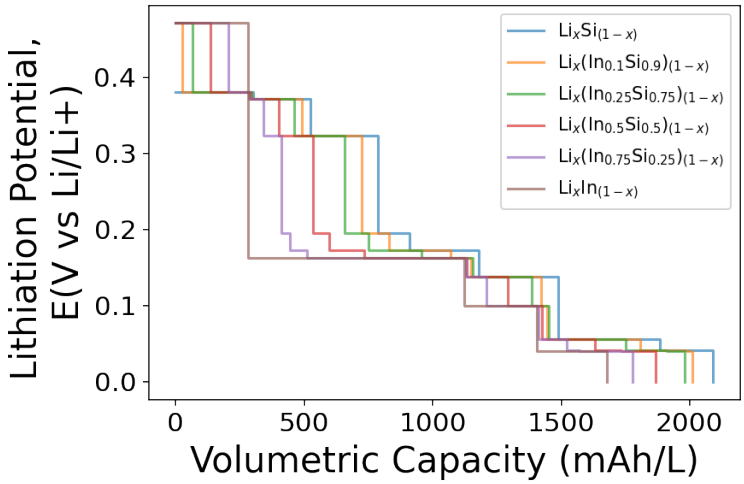

Figure A.99: Lithiation voltages for select compositions in the In-Li-Si chemical system.

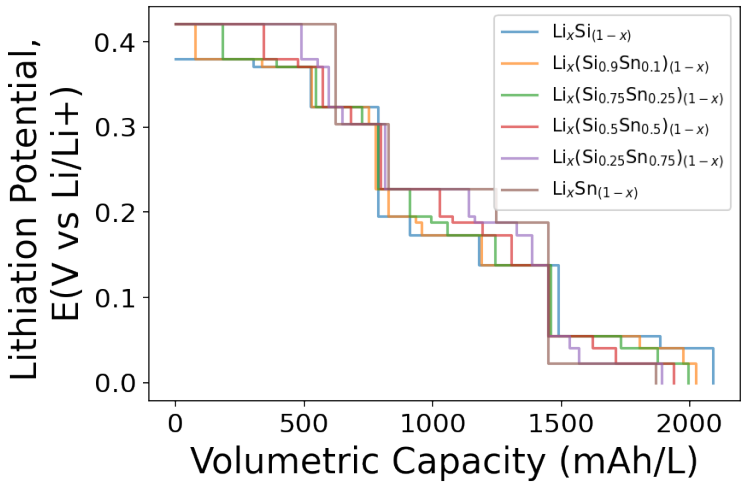

Figure A.100: Lithiation voltages for select compositions in the Li-Si-Sn chemical system.

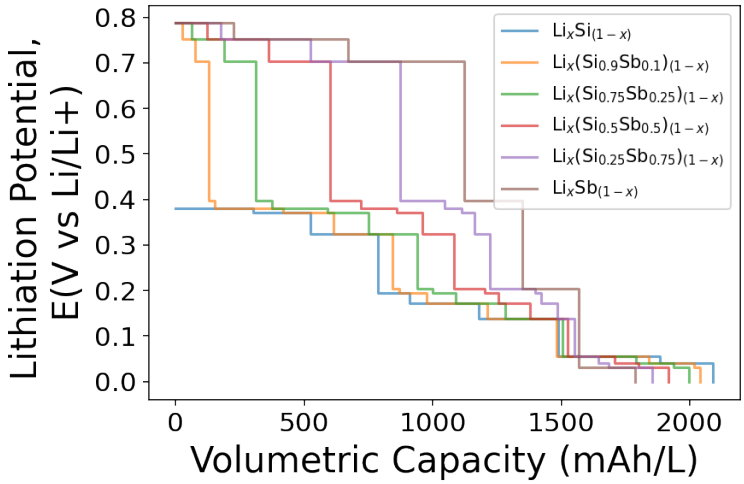

Figure A.101: Lithiation voltages for select compositions in the Li-Sb-Si chemical system.

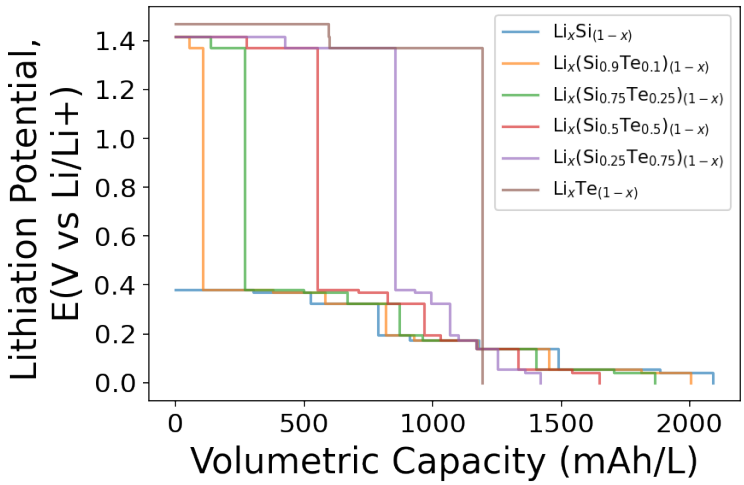

Figure A.102: Lithiation voltages for select compositions in the Li-Si-Te chemical system.

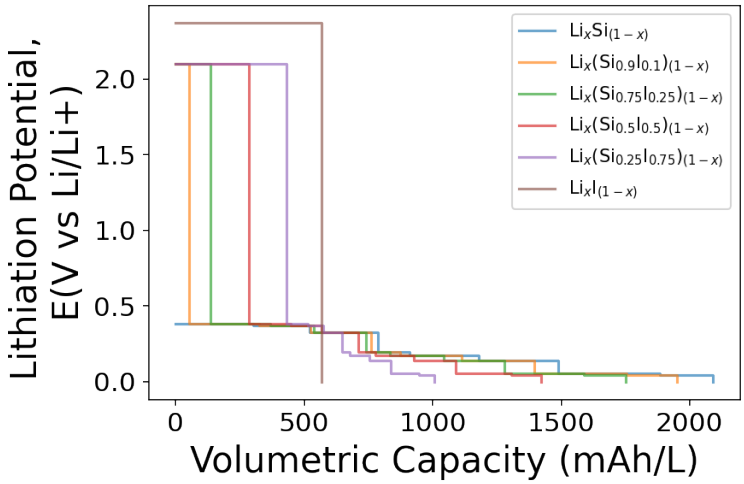

Figure A.103: Lithiation voltages for select compositions in the I-Li-Si chemical system.

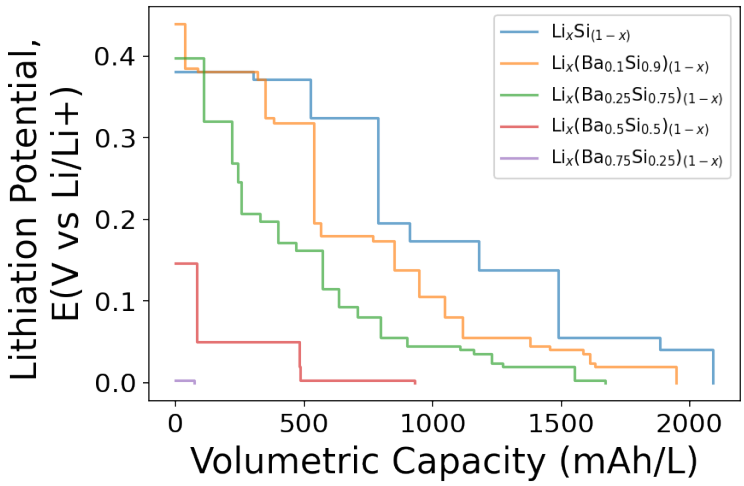

Figure A.104: Lithiation voltages for select compositions in the Ba-Li-Si chemical system.

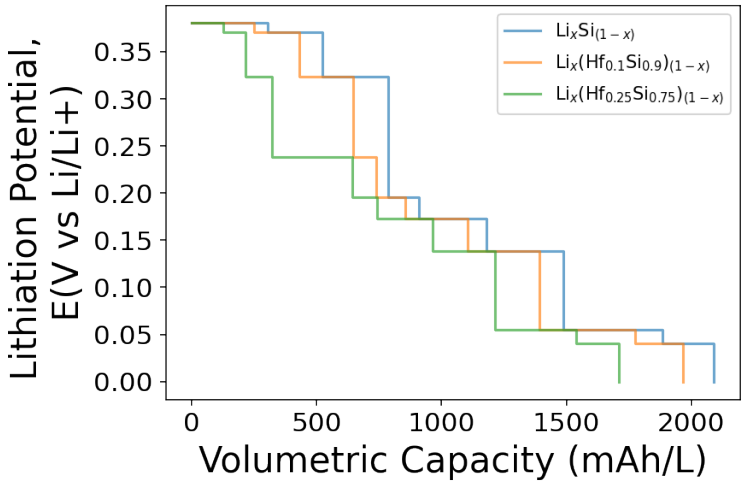

Figure A.105: Lithiation voltages for select compositions in the Hf-Li-Si chemical system.

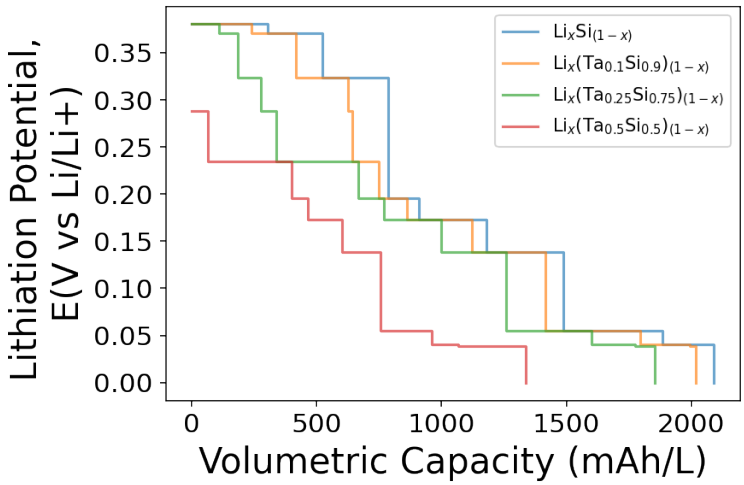

Figure A.106: Lithiation voltages for select compositions in the Li-Si-Ta chemical system.

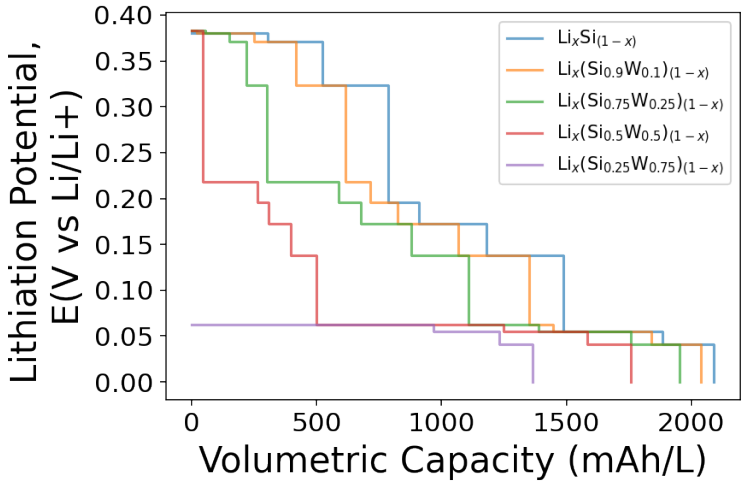

Figure A.107: Lithiation voltages for select compositions in the Li-Si-W chemical system.

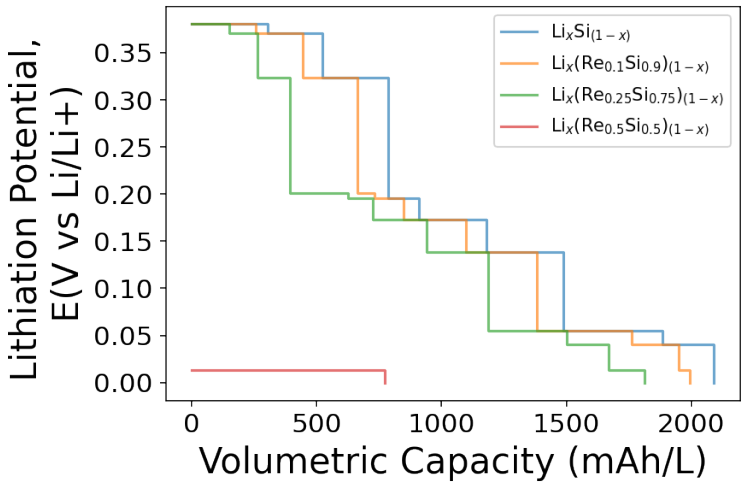

Figure A.108: Lithiation voltages for select compositions in the Li-Re-Si chemical system.

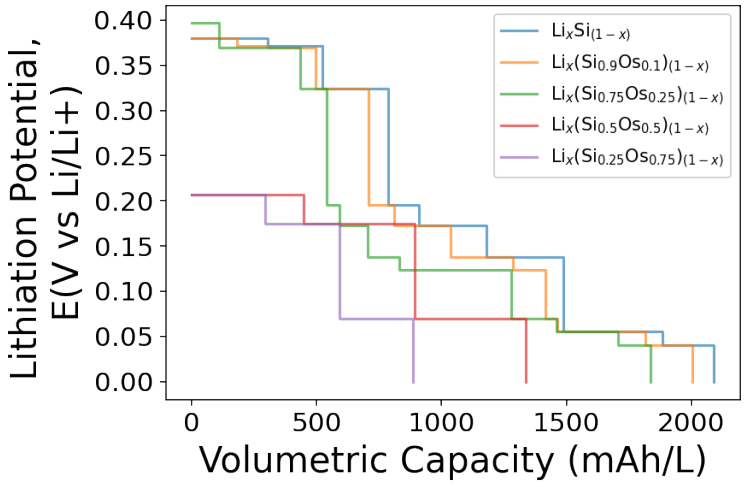

Figure A.109: Lithiation voltages for select compositions in the Li-Os-Si chemical system.

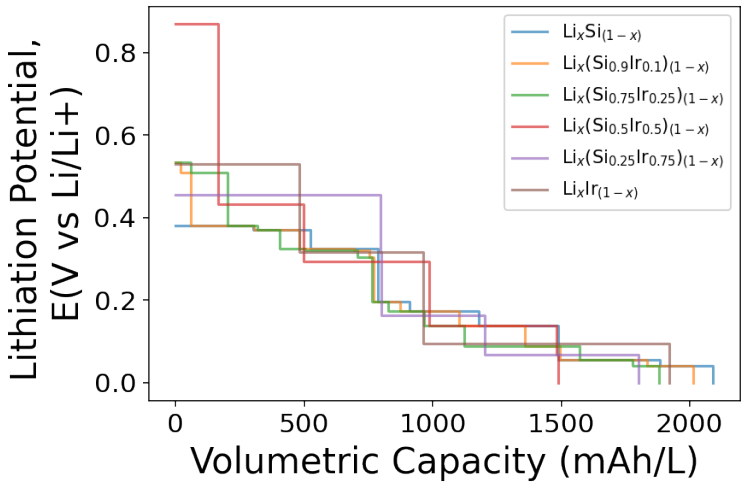

Figure A.110: Lithiation voltages for select compositions in the Ir-Li-Si chemical system.

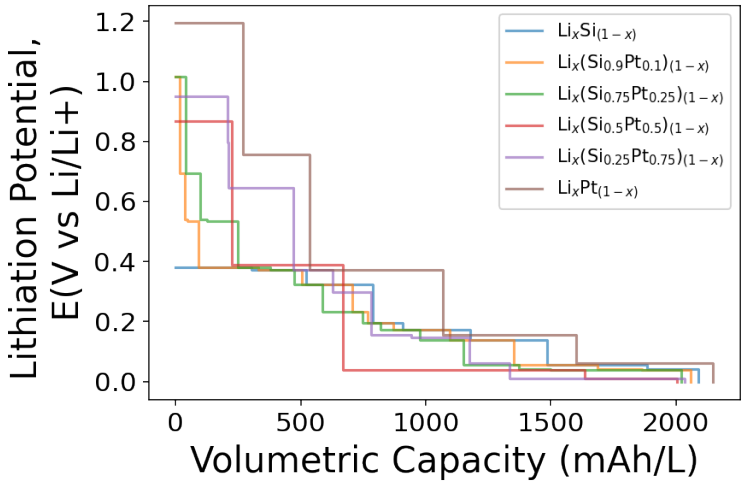

Figure A.111: Lithiation voltages for select compositions in the Li-Pt-Si chemical system.

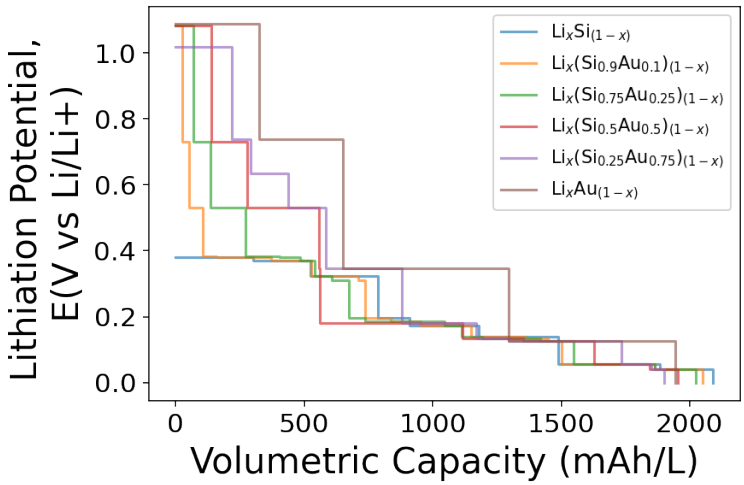

Figure A.112: Lithiation voltages for select compositions in the Au-Li-Si chemical system.

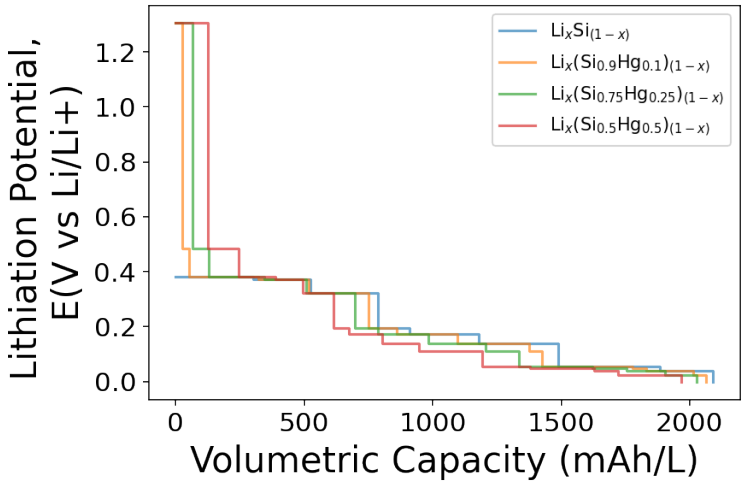

Figure A.113: Lithiation voltages for select compositions in the Hg-Li-Si chemical system.

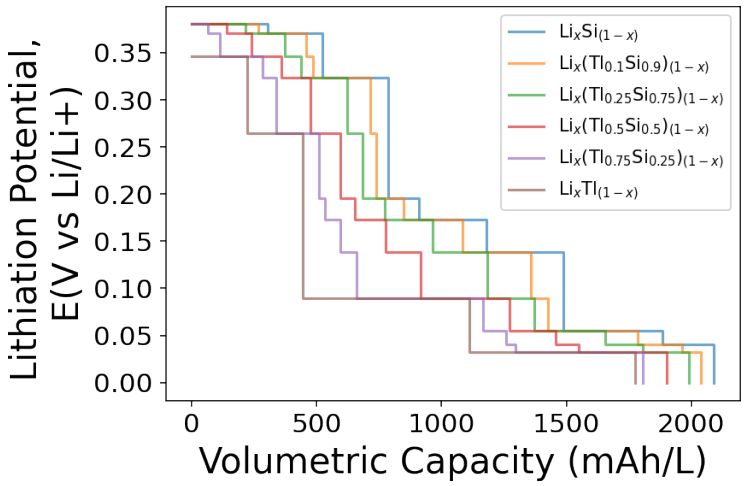

Figure A.114: Lithiation voltages for select compositions in the Li-Si-Tl chemical system.

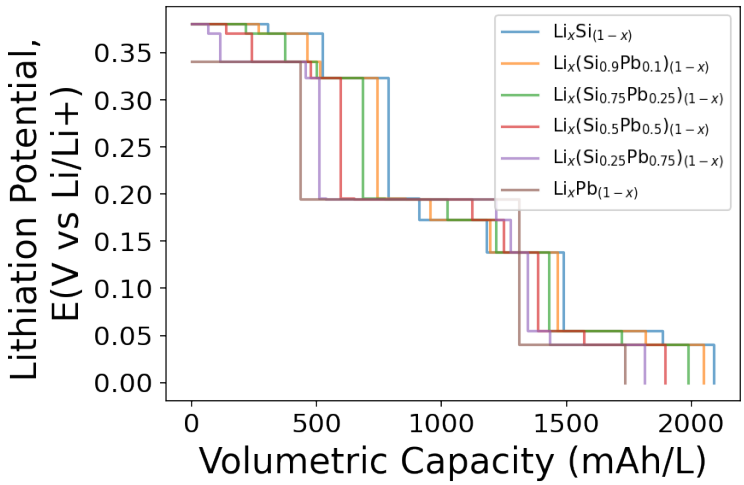

Figure A.115: Lithiation voltages for select compositions in the Li-Pb-Si chemical system.